Advances in Colloid and Interface Science 327 (2024) 103141

Contents lists available at ScienceDirect

Advances in Colloid and Interface Science

journal homepage: www.elsevier.com/locate/cis

Advances in sample environments for neutron scattering for colloid and interface science

Anton P. Le Brun, Elliot Paul Gilbert *

Australian Centre for Neutron Scattering, Australian Nuclear Science and Technology Organisation (ANSTO), New Illawarra Road, Lucas Heights, NSW 2234, Australia

ARTICLE INFO

Keywords:
Pressure
Shear
Electric field
Magnetic field
IR/visible/UV light
Machine learning

ABSTRACT

This review describes recent advances in sample environments across the full complement of applicable neutron scattering techniques to colloid and interface science. Temperature, pressure, flow, tensile testing, ultrasound, chemical reactions, IR/visible/UV light, confinement, humidity and electric and magnetic field application, as well as tandem X-ray methods, are all addressed. Consideration for material choices in sample environments and data acquisition methods are also covered as well as discussion of current and potential future use of machine learning and artificial intelligence.

1. Introduction

Sample environments are an essential and integral inclusion to all neutron scattering experiments. While it is possible that measurements at ambient temperature and pressure, and under the influence of the Earth's magnetic field are sufficient for a scientific study, this is rarely the case. Consequently, additional equipment to apply specific conditions and to induce the sample into a phase or state of particular interest is desirable. A non-exhaustive list includes subjecting the sample to high or low temperatures, high pressure or under vacuum, varying magnetic field, controlled shear stress or strain, exposure to vapour, chemical manipulation or a simultaneous combination of several such conditions. Note that while some of the above options have the primary objective of keeping a certain parameter fixed (e.g., pressure), others may be used to deliberately manipulate the structure or dynamics of the sample during measurement (e.g., following a temperature quench or observing the relaxation of a complex fluid following the cessation of shear).

'Standard environments' could include a humidity generator, a temperature-ramping cell, tumbler cell (to prevent sedimentation), stop-flow [1] or continuous flow cell. However, despite their critical role, conducting a literature search in Scopus using the search term "neutron" AND "sample AND environment*" AND "scattering OR radiograph* OR tomograph* OR reflect*" and limiting the search to articles that only had "sample environment" as a keyword yielded only 113 articles from the time period 2005 to October 2023. Analysing the search result in VOS viewer [2] using a co-occurrence analysis shows how the articles are related to one another according to keyword terms. In Figure 1 each ball represents a keyword term, and the size of the ball is the weight of that term. As can been seen the term "sample environment" is the largest item as every article in the analysis used this as a keyword. The lines represent the link between each term and the colour represents a cluster of items (e.g., red is one cluster), and a cluster is the strength of the relatedness of the terms. In Fig. 1 there are nine clusters with the largest cluster being the red cluster with 29 terms and the smallest cluster only having one term ("pulsed magnet"). The most distinct and second largest cluster is the green cluster which has terms mainly relating to cryogenics and low temperature effects. Terms that could be conceived as being particularly related to colloid and interface science such as "soft matter", "rheology", "lipid bilayer", etc., are generally spread out and not concentrated in a particular cluster. What we interpret from this is that colloid and interface science makes the most demand for novel or bespoke sample environments whereas other areas of science that utilise neutron scattering tend to (but not exclusively) use more 'standard' or commercially available equipment.

Neutron scattering centres will readily advertise their range of sample environments [3,4] that can be selected when a proposal is prepared. Many will be common across facilities e.g., cryostats, superconducting magnets, etc. while others will be unique. A number of reviews have described sample environments for neutron scattering. Lindner et al. [1] discuss sample environments for small-angle neutron scattering (SANS) and neutron reflectometry (NR). The reader is directed to the excellent 2021 review of sample environments

* Corresponding author.
E-mail address: elliot.gilbert@ansto.gov.au (E.P. Gilbert).

https://doi.org/10.1016/j.cis.2024.103141
Received 8 December 2023; Received in revised form 27 March 2024; Accepted 27 March 2024
Available online 4 April 2024

specifically for SANS with a focus on time-resolved neutron scattering experiments [5]. More recently Martel and Gebel reviewed this area more broadly for structural biology [6]. Recent reviews of developments in NR have also discussed aspects of sample environments that can be used for surface and interface analysis [7,8]. It is also relevant to consult several previous works dedicated to X-ray facilities [9–11] despite some of the described devices not being currently available for neutrons, since an appreciation of what is possible can both inform the technical aspects required to develop neutron-suitable equipment and highlight potential opportunities. An example is differential scanning calorimetry – a technique widely used simultaneously at X-ray facilities – which, only relatively recently has been implemented for SANS [12]. It is indisputable that the development of sample environments for X-ray scattering is more advanced than for neutron scattering. Reasons for this relate to both beam intensity, and thus the ability to achieve much greater time resolution, as well as (and indeed related) the opportunity to use implicitly smaller beams. However, the advantages of contrast, beam penetration as well the avoidance of beam-mediated sample damage position neutrons as a probe important in their own right. These and other advantages of neutron scattering are briefly outlined below.

Sample environments which are non-standard, that may be bespoke or not generally commercially available or simply have been used in a non-standard way, and that find application to colloid and interface research, represent the focus of this article. As a consequence, extreme environments including high magnetic fields and very low and very high temperature devices are not considered here. A recurring theme concerns the ability to collect neutron scattering data while, at the same time, measuring with a complementary technique. This is a particular advantage for in situ or *in operando* studies of complex nanoscale systems which irreversibly change their structure with time, e.g., upon a reaction, crystallisation, aggregation, gelation, particle formation, growth, or aging process. The potential gain in information, compared to conducting two independent measurements (i.e., one for each technique) should be balanced with the effort required to implement such a 'simultaneous' system. As a rule of thumb, for studies in which structural changes occur over a period of, say, greater than two minutes, independent measurements generally have the possibility to be correlated without a significant error in time [12]. The review therefore also extends itself to the concept of tandem techniques as opposed to individual sample environments per se where combined methods are used to reveal additional information on a sample e.g., combined SANS and SAXS. Where appropriate, the focus is also on the last few years since the publication of the most recent reviews in this field.

2. Neutron scattering and its application for colloids and interfaces

A neutron is a sub-atomic particle, exhibiting wave-like properties, present in the nuclei of all atoms except the principal isotope of hydrogen, protium. When produced in sufficient quantities at either

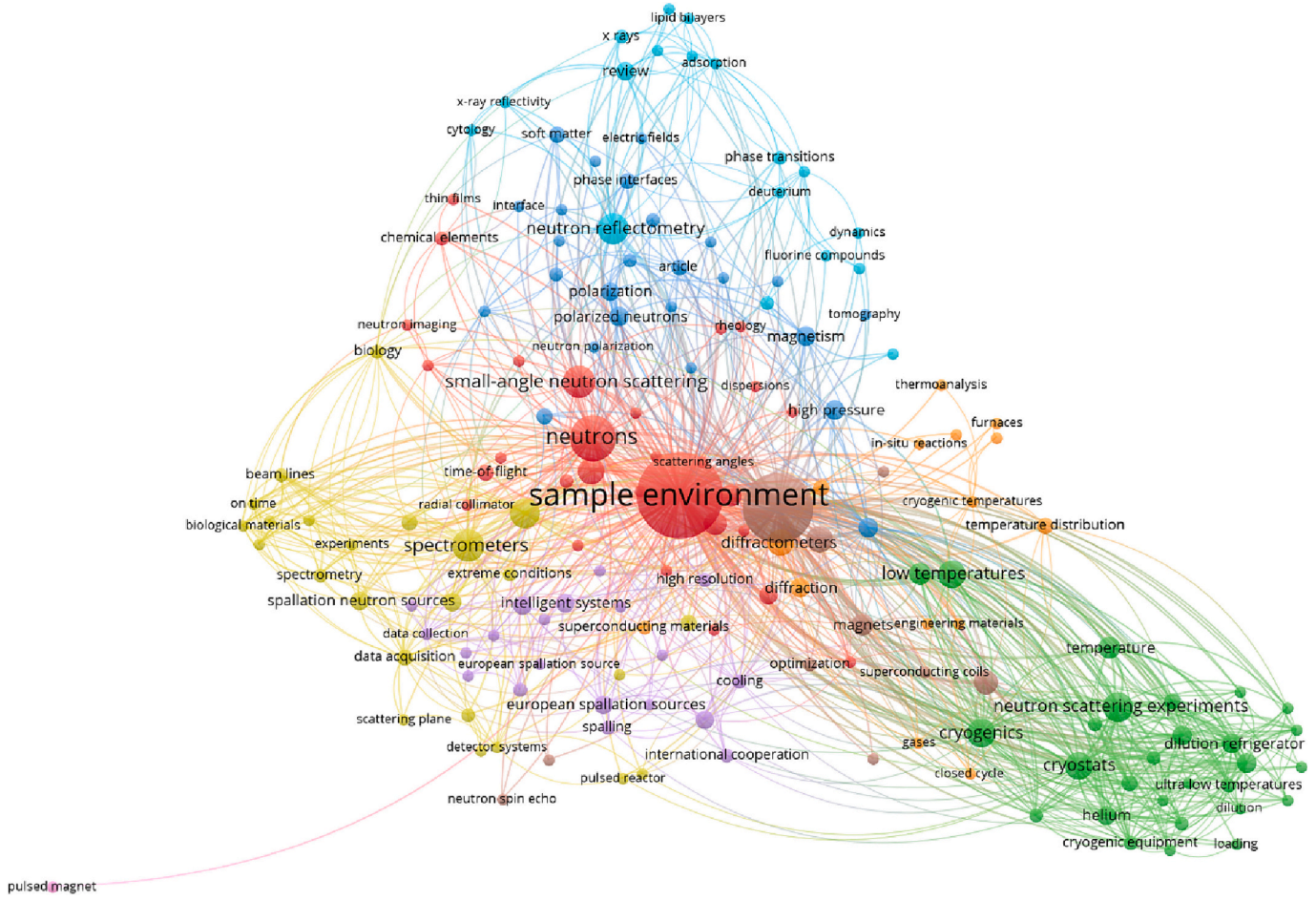

Fig. 1. A network diagram of keywords created in VOS viewer (version 1.6.19) [2] from a Scopus literature search showing the relationships between the keywords. The search term used in the Scopus search was "neutron" AND "sample AND environment*" AND "scattering OR radiograph* OR tomograph* OR reflect*" and was limited to documents which only had "sample environment" as a keyword and found 113 publications from 2005 to October 2023. The VOS viewer network was created using a co-occurrence analysis using all keywords and a full counting method. To be included in the network, keywords had to have an occurrence of two or more.

reactors or accelerator sources, intense beams of neutrons can be generated that, following their interaction with a material of interest, are able to provide information on either the structure and/or dynamics within the material; this is achieved by measuring the change in the direction of the neutron, sometimes combined with an assessment of the associated energy changes, to describe the interaction process. Such a process is referred to as neutron scattering.

In the context of colloids and interfaces, of all neutron scattering methods, it is undoubtedly the case that small-angle neutron scattering (SANS) and neutron reflectometry (NR) are by far the most utilised as they reveal structure on a length scale from one to several hundred nanometres. In the case of SANS, this size range can be extended further with very small-angle neutron scattering (VSANS) methods as well as ultra-small-angle neutron scattering (USANS); the former employs a range of optical approaches (e.g. multi-beam converging apertures, material or magnetic lenses, or focusing mirrors) to access lower angles while maintaining pinhole geometry while the latter uses multiple-bounce reflection from monochromator and analyser crystals resulting in slit smeared data [13]. Other neutron methods that can be applied to colloids and interfaces includes spin echo SANS (SESANS) [14] which yields data on a similar size range to USANS but employs a polarised (i.e., spin selected) neutron beam. Here, the Larmor precession of the neutron spin in a magnetic field is used to label the direction of the neutron path and by using opposing magnetic fields before and after the sample a spin-echo is obtained for unscattered neutrons, however, any small angle scattering will depolarise the neutron beam yielding structural information. However, since the neutron spin must be controlled throughout the instrument, this has implications in terms of the suitability of samples and sample environments. For example, while measurements of magnetic samples are possible, they are nonetheless challenging although this can be addressed if all necessary polarisation manipulation can be achieved upstream of the sample, as is the case for spin-echo modulated SANS (SEMSANS) [15]. For NR the length scales covered are similar to SANS, however the sample of interest is confined to a surface or interface and the structure obtained is a one-dimensional depth profile which describes the thickness, composition and roughness of the layer(s) of interest. A wide range of interfaces can be studied including gas-solid, solid-liquid, gas-liquid, solid-solid (buried interfaces), and the more technically challenging, liquid-liquid. In experiments the specular reflection is measured where the angle of incidence is equal to angle of reflection which yields the structures perpendicular to the plane of the surface [16]. In some cases, off-specular reflection may be measured where the angles of incidence and reflection are not equal, and the final information includes in-plane structural correlations [17]. Grazing incidence SANS (GI-SANS) also covers the same length scales as traditional transmission-based SANS but within a surface scattering geometry to study in-plane structures such as the arrangement of particles at a surface [18]. Additional techniques, including neutron radiography/tomography, as applied to colloids and interfaces will also be described further in this section as well as inelastic and quasielastic neutron scattering (QENS) [19].

Unlike more conventional probes of structure, namely X-rays, electrons and photons, the neutron interacts with the atomic nucleus. This is noteworthy for several reasons. Firstly, neutron scattering is isotopically sensitive meaning that the scattering intensity can be manipulated by varying the isotopic composition of a material e.g., by replacing hydrogen (composed almost exclusively by protium) with deuterium. Indeed, this property is one of the main motivations for using neutrons for studying colloids and interfaces as particular molecules within mixtures can be made effectively transparent, thus making no contribution to the overall scattering, through 'contrast matching' via solvent contrast variation (e.g., H_2O / D_2O exchange) or selective deuteration to manipulate the neutron scattering length density (SLD) [20]. In addition, the exchange of hydrogen for deuterium also vastly reduces the incoherent background, which is additionally assists neutron crystallography, quasielastic neutron scattering (QENS) and inelastic neutron scattering more generally, to reduce the scattering contribution of components that are not of interest. Secondly, since the nuclear structure, i.e., the sum of protons and neutrons within the atomic nucleus, varies across the periodic table in a non-linear fashion, adjacent elements can have markedly different interactions with the neutron, characterised by the atomic scattering length; this enables, for example, the contribution of elements of similar atomic number to the structural arrangement within a material to be directly discerned. This property is crucial to the success of neutron powder diffraction albeit not widely used in the study of colloids. Thirdly, the atomic nucleus is approximately four orders of magnitude smaller in size than the atom, the latter comprising its nucleus and its orbiting electrons; consequently, as far as the neutron is concerned (which is ten times smaller than a typical nucleus), materials comprise atoms separated by large distances. Indeed, an analogy often used in teaching is to consider that if the neutron were the size of a pea, the atom would be the size of a tennis ball while the atoms in a typical material would be separated by a distance of 1 km. Consequently, neutrons are a highly penetrating form of radiation and, as a result, are not only an excellent probe deep inside materials but also through sample environments which is the focus of the current review. The caveat here is that any material through which the neutrons pass should be made as transparent as possible; this may involve replacing materials composed of plastic - an intense source of scattering due to their typically high hydrogen content - with 'neutron-friendly' materials such as aluminium, titanium, silicon or sapphire.

The associated neutron scattering process can be elastic or inelastic. In an elastic neutron scattering event, while there is no change in the energy of the neutron as a result of its interaction with a sample, there may be a change in its wavevector, $\vec{k}$. $\vec{k}$ indicates the direction of propagation of the neutron while its magnitude $\left(=\frac{2\pi}{\lambda}\right)$ determines its energy, E, through the relation $E=\frac{h^2k^2}{(2\pi)^2 2m}$ where h is Planck's constant and m is the neutron mass. The conservation of energy in elastic scattering implies that any change in $\vec{k}$ is limited to a change in the wavevector direction not its magnitude. In this case, the scattering intensity is expressed in terms of the wavevector transfer, $\vec{q}$ (also commonly written as $\vec{Q}$), $=\vec{k}_f-\vec{k}_i$ where $\vec{k}_i$ and $\vec{k}_f$ are the wavevectors of the incident and scattered neutrons, respectively. Consequently, the magnitude of the scattering vector, q, can be expressed via the equation $\frac{4\pi}{\lambda}sin\vartheta$ (where ϑ is half the scattering angle and λ is the neutron wavelength). q is defined in units of inverse length or reciprocal space. It can be readily shown, by substitution of this equation into Bragg's Law, that q is related to real-space structures with dimension, d, via $q=\frac{2\pi}{d}$. The resultant elastic neutron scattering yields structural information that may cover a size range from the sub-nanometre (i.e., atomic) to micron length (macromolecular) scale.

In contrast to elastic scattering, the neutron may also lose or gain energy as a result of its interaction with the sample; the associated energy difference yields information on internal dynamics or correlations within the material under study. Neutron techniques overall can cover over nine orders of magnitude in terms of energy transfer with slower motions requiring instrumentation with better energy resolution. Such measurements are referred to as either quasielastic or inelastic, with the two differing in terms of the amount of energy exchanged between the neutron and the material. While elastic scattering can be described solely by q, inelastic scattering is denoted by the additional symbols of E (for energy), ω (angular frequency) or t (time).

Within these elastic or inelastic processes, neutrons can be scattered coherently or incoherently. Coherent scattering provides information on the relative positions of nuclei and the motions of particles via elastic and quasielastic/inelastic scattering processes respectively. Incoherent scattering is spatially isotropic and, when energy-resolved, provides information on single particle dynamics. The incoherent scattering cross-section - where the cross-section is a measure of the probability of a scattering event occurring - for many isotopes present in soft

condensed matter systems is either zero or close to zero. Protium, however, has one of the largest incoherent cross-sections of any isotope in the periodic table; as a result, the neutron incoherent scattering signal is extremely sensitive to any motion involving hydrogen.

For the purposes of studying colloids and interfaces, it is typically only for QENS, where small changes in energy occur centred at zero energy transfer, which is relevant here; the technique provides the time scale of relaxation as well as the geometrical constraints involving translational and rotational motion e.g., diffusion and molecular reorientation over fractions of a picosecond to hundreds of nanoseconds and from the sub-nanometre to tens of nanometre. Spin echo spectroscopy is the highest energy resolution technique and can extend the time domain further into the microsecond to explore much slower dynamics. For completeness, it should be noted that there is a neutron vibrational spectroscopy technique that is complementary to infra-red and Raman spectroscopy but with the benefits of having no selection rules and, in common with other neutron methods, high penetration through matter and high sensitivity to hydrogen. However, with the increasing complexity of vibrational spectra with molecular size and disorder, this inelastic scattering technique finds greater potential for smaller molecules or molecules with greater order e.g., polymers in the solid state.

Neutron scattering traditionally also includes the technique of neutron radiography whereby neutrons are measured following transmission through a sample; the associated images obtained rely on the scattering of neutrons out of the incident beam thus reducing their transmission through the material investigated. For example, the distribution of moisture within a porous material can be easily measured since the incoherent scattering from hydrogen in water serves to attenuate the neutron beam. Typical spatial resolutions are of the order of 10 μm. When measurements can be conducted at multiple angles, the images can be reconstructed in three-dimensions with neutron tomography.

While neutrons clearly have a range of unique attributes, that is not to say that neutrons are superior to other probes; indeed, based on both the intensity of neutron beams (there are more photons from a light bulb than neutrons from a reactor!), and with the difficulty in accessing such facilities, the opposite is perhaps far closer to the truth. However, their properties make neutrons exceptionally useful to obtain detailed information that is unavailable from other methods for the study of colloids and interfaces.

3. Considerations for sample environment in neutron scattering

3.1. Materials

The selection of suitable materials for neutron applications is naturally quite distinct to that for X-ray applications due to the difference in scattering properties of the two probes; it relies on a range of factors including the need for high neutron transmission, low background, and minimal potential for neutron activation. Of importance is also the ability to machine the material (usually as thin as possible to reduce the mass of extraneous materials in the beam) while also providing structural integrity (e.g., withstanding pressure, corrosion) and minimising parasitic scattering, particularly for SANS (e.g., from inclusions, precipitates, etc.). Silicon, sapphire, and quartz are commonly used materials, particularly for windows, while tougher components are manufactured from aluminium and titanium. Many windows in sample environments to allow entry of the incident beam and exit of the scattered beam will use aluminium. This is due to aluminium's high transparency to neutrons and low incoherent scattering cross section. While aluminium is also a suitable material for machining and windows can be made relatively thin, chemical compatibility needs to be checked particularly with chlorides. While vanadium tends to be the material of choice for powder diffraction due to its low coherent cross-section, its high incoherent cross-section makes its unsuitable for inelastic studies where aluminium is preferred. Despite the widespread use of sapphire and quartz in neutron instrumentation, either for vacuum windows or sample cell design, there are factors that need to be considered in the context of crystallinity. For example, Harris et al., [21] and Chung et al., [22] report on inelastic scattering modes from silica that can contaminate the signal in SANS experiments. With metals such as vanadium and titanium, hydrogen embrittlement need to be considered if using a hydrogen (or deuterium) gas, particularly at elevated temperatures and/or pressures [23,24]. Research continues however to identify new materials.

The appropriate material selection may differ from one neutron application to another; for example, Kibble et al. [25] recently presented studies of low-background materials for high pressure cells for inelastic neutron scattering. The compound $Zr_{59.3}Cu_{28.8}Al_{10.4}Nb_{1.5}$ has recently been studied and may find potential for use as a material for sample environments for neutron scattering [26,27]. A more technically challenging alternative is to completely remove the need for a sample container as is the case for levitating samples [28], often combined with laser heating. The advantage of this method is that the sample is suspended without need for a sample holder simplifying any background subtraction and allows for the integration of additional techniques. An excellent recent review by Benmore and Weber [28] discusses how these sample levitation developments have been used at several international x-ray and neutron sources. Inevitably such levitation-based options are not readily applicable to colloid and interfacial materials. However, Krauss et al. [29] developed a simple yet effective system for containerless SANS measurements (Fig. 2); it is based on the flow of the liquid sample through a Teflon-based trapezoid-shaped inlet piece that spreads the liquid between two wires to generate a free-flowing film. Instrumental background is reduced by 37% compared to standard quartz cells while humidity control is achieved by placing the system into a glove bag purged by a constant flow of He gas with openings for the collimation and detector ends of the sample area.

Solid-liquid cells used for NR measurements typically comprise the substrate wafer, such as silicon, quartz, sapphire, etc., a backing material which is separated from the substrate with a gasket, with the whole assembly being brought together by sandwiching the substrate and backing between aluminium plates. The aluminium plates can also have channels connected to a circulating water bath for temperature control [30,31]. For NR experiments to be successful, the substrate wafers must have a low roughness ideally 3 Å or less. The choice of backing can vary with poly(tetrafluoroethylene) (PTFE) being popular due to its relative ease for machining and wide chemical resistance; poly(etheretherketone) (PEEK) is also a popular choice for similar reasons.

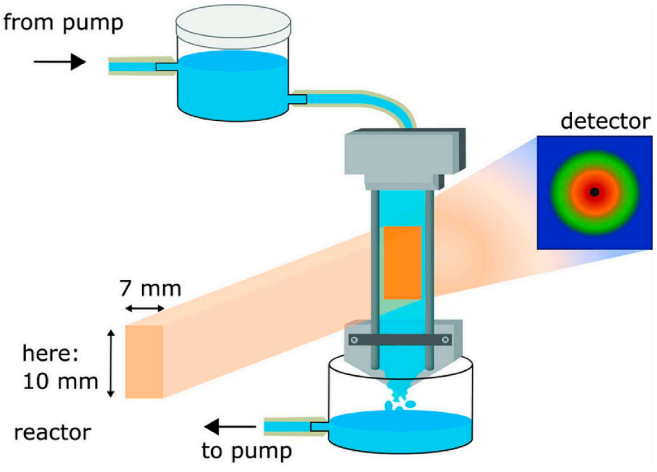

Fig. 2. Schematic of the free-film setup. The neutron beam on the free film is indicated by an orange square. Reproduced from [29] with permission from the International Union of Crystallography under creative commons CC BY 4.0 DEED.

However, with both PTFE and PEEK the drawback is that they can contribute to background scattering from the cell and therefore a deeper liquid subphase is required or shielding masks such as cadmium may be needed [1]. This can be overcome by using silicon as a backing material and using thin gaskets. Silicon single crystals are a suitable backing material because of silicon's low incoherent scattering cross section and high neutron transmission. However, the drawbacks are that it is brittle, easily damaged as well as difficult to machine. Through thin solvent reservoirs and silicon backing wafers Hoogerheide et al. [32] developed a new approach for background subtraction for monochromatic reflectometers. This approach was further used on the new CANDOR white beam reflectometer where a background of $<10^{-8}$ in reflectivity was achieved through using a silicon backing wafer at a solvent reservoir <50 μm thick and energy-analysing the reflected beam [33].

PTFE is also a useful material for making free-liquid troughs for studying layers absorbed at the air-liquid interface. Liquid troughs can be encased within aluminium housing with sapphire windows to prevent evaporation. Heating pads can also be used to regulate temperature in which case the housing can be doubly insulated to prevent condensation [34]. If PTFE is not a compatible material for free-liquid surfaces, alternative materials for the troughs such as stainless steel or polyoxymethylene can be used [1].

Quartz is commonly used to make windows for various sample environments due to its low incoherent scattering cross section and high neutron transmission. As a backing material for solid-liquid cells, it can reduce background for the study of polymer films at the solid-liquid interface using GI-SANS [35]. It can also be used as a material for creating liquid-liquid cells where a PTFE trough can be placed inside a quartz cell with the aqueous phase used to fill the PTFE trough while the organic phase fills the remaining quartz cell [36]. An alternative design is where the liquid-liquid cell has two compartments with the lower compartment being a trough to contain the aqueous phase and the upper compartment, containing the organic phase, having quartz windows to allow for the neutron beam passage through the cell [37].

In terms of technological developments, advanced manufacturing techniques have been increasingly used to create more complex and intricately designed sample environments or for more rapid fabrication of consumable items. One example of this is the increased use of 3D printing. To date 3D printing has been utilised to produce parts for solid-liquid cells for NR [31], and collimators, apertures and shielding components using borated filaments [38–40], while the 3D printing of titanium has been used to fabricate an impeller for a Rapid ViscoAnalyser [41] which is discussed below. Single crystal mountings that are bespoke to crystal dimensions have been printed from the alloy $AlSi_{10}Mg$ [42]. This was achieved by 3D scanning the crystal first and then using computer aided design to generate the model to be printed. Indeed, whole sample environments can be created from 3D printing as has been demonstrated through the fabrication and successful use of a humidity chamber for GI-SANS [43].

3.2. Data acquisition

It is desirable to be able to measure the response of a system to a changing external parameter, e.g., temperature following a quench or jump, as a function of time to yield kinetic information. Irrespective of the technique, the greatest time resolution of the signal obtained from a sample undergoing a rapid change is highly dependent on the shortest timeframe that may provide a statistically viable data point. The brute force approach is to use the maximum flux available – the so-called single-shot kinetics experiment – but this immediately places synchrotron studies at a significant advantage to those with neutrons. Despite neutron scattering, compared to its X-ray counterpart, being a more flux limited technique, kinetic information down to 1 s time resolution is not uncommon [44]. To obtain greater time resolution, and assuming scattering intensity is not a limitation, event mode acquisition can be employed where a single acquisition is taken over the entire changing event. As each neutron that is detected has its position and time on the detector recorded, the data can then be processed post-data collection at desired time intervals corresponding to the external variable that is being tested [45–47]. Event mode acquisition has been used for studying rheological processes to sub-millisecond time resolution [48], thermal annealing of organic photovoltaic devices using a ramp rate of 2 °C min^{-1} [49], and time-resolved deposition of copper or silver from deep eutectic solvents onto gold surfaces [50].

The flux issue can be circumvented to some extent if the system responds completely reversibly and reproducibly to a stimulus, without degrading (or, potentially, in the case of irreversible processes such as a reaction, enough sample material is available to allow the experiment to be repeated). In this case, one can repeat the experiment many times to accumulate sufficient statistics within each time bin. Using a stroboscopic approach, where the measurement can proceed over many cycles of the kinetic process and the time dependent information recovered post-measurement, time bins of the equivalent stage can then be added to provide sufficient counting statistics for the data to be analysed. With this approach, time resolution down to 50–100 milliseconds is relatively straightforward when incorporated with event mode acquisition.

There has been detailed discussion on the best approach to reduce and normalise data [51,52]. Stroboscopic measurements were first reported for applying an alternating current field to liquid crystals [53]. Stroboscopic measurements have been applied to in situ rheology and SANS experiments to study the crystallisation behaviour of Pluronic F127 under shear [54] and structural deformation of polymer-like micelles [55]. It also has been used for investigating the structural arrangement of Pluronic F127 mixed with magnetic nanoparticles under oscillatory shear using polarised GI-SANS [56]. For the latter, neutron frames from the instrument were aligned with the output voltage of the rheometer (the output voltage is proportional to the shear rate); it was found that when the shear rate was at a maximum both the specular and off-specular scattering intensity was at its lowest and a time resolution of 0.1 s could be achieved. More examples where this approach has been used are discussed in subsequent sections.

The intrinsic wavelength spread imposes the limits on time-resolved measurements of a few milliseconds for monochromatic SANS instruments since the range of times-of-arrival of neutrons at the detector may be comparable to the time domain of interest. Similar, but smaller, time-resolution uncertainties may apply in the case of spallation sources where this results from finite neutron moderation times [57]. To yield enhanced time resolution, so-called TISANE methods are available for SANS. In this case, a fast chopper near the beginning of the collimator of the SANS instrument is employed, along with a detector with suitable fine time resolution and sample environment in which the scattering properties of the sample are time-modulated. Parameters for these modulations may be magnetic or electric fields, alternating currents, or ultrasonic pulses. Such an approach is technically challenging but together, it is possible to achieve time resolutions down well into the sub-millisecond [58]. With the development of the European Spallation Source, the ability to perform more sophisticated time-resolved measurements using data aggregation and streaming architecture will make the above experiments, hopefully, more routine [59].

3.3. Machine learning and artificial intelligence

Artificial intelligence has attracted enormous media attention recently with the public release of ChatGPT in November 2022 with a range of competitor products being available shortly thereafter. It involves teaching a machine, via the manual selection and extraction of features from raw data, to perform a specific task and provide accurate results by identifying patterns. Machine learning is a subset of artificial intelligence that automatically enables a machine or system to learn and improve from experience. A workshop focussed on the topic of machine learning for X-ray and neutron scattering was held in the United States in 2023 with a further workshop scheduled to take place in 2024 in

Germany [60,61]. Through the common machine learning technique of training of a neural network, a large amount of repetitive work and potentially experience-related knowledge can both be transferred from the experimenter to a computer as well as provide the opportunity of real-time data analysis and more efficient beamline operation.

Doucet et al. [62] discuss efforts that have been made to use machine learning across multiple scattering methods at Oak Ridge National Laboratory (ORNL). Chen et al. [63] also discuss machine learning and artificial intelligence across multiple neutron and X-ray techniques including inelastic scattering and radiography. SANS and NR experiments have been identified as the neutron techniques that are most likely to benefit from machine learning since the final data generated are a series of one-dimensional curves; the computational costs are therefore not as great as for inelastic techniques where data are more complex due to the additional dimension of energy space [64]. Hao et al. [65] have reported on the application of machine learning for neutron diffraction to recognise Bragg peaks and corresponding regions of interest; this information is then used to automatically screen and align a measured crystal, and subsequently plan and optimise the data collection with user-provided information and uncertainty quantification values of the detected peaks. Do et al. [66] and Archibald et al. [67] also demonstrate how machine learning algorithms can be used to suggest appropriate scattering models that can describe an experimentally measured one-dimensional SANS profile. Chang et al. [68] used a deep-learning based super-resolution algorithm using neural network models to demonstrate that time-resolved SANS experiments with a finer time resolution can be achieved by boradening the effective detector resolution. For a given collection time, there is a trade-off between counting statistics per detector pixel and detector resolution.

Machine learning and artificial neutral networks have been used for automation of NR data analysis and optimisation of experimental conditions [69]. Neural networks has been used to optimise data analysis for one-layer [70], two-layer [71], and multi-layer systems [72,73]; in each, the data analysis process was sped-up and optimized. In addition, it has been used to fit data from complex systems that use multiple isotopic contrasts such as lipid bilayers [74]. The use of machine learning to optimise experimental conditions and processes is of increasing interest and how sample environments factor into this will be an important consideration. Information theory has been used for NR to optimise the experimental conditions such as counting time required, maximum momentum transfer needed as well as choosing the optimum scattering length densities for isotopic contrasts of the surrounding solution [75].

Large-scale simulations for training can also be used to explore phase diagrams of materials and identify underlying physical mechanisms. They also provide a powerful basis on which to steer experiments. Probably the best recent example of this is the work of Beaucage and Martin [76] in which they describe the design of the "Autonomous Formulation Laboratory" for the automated synthesis and measurement of complex liquid mixtures (Fig. 3). The platform prepares samples from stock solutions from which their structure can be characterised using any number of techniques centred around, but not limited to, neutron and X-ray scattering. In the context of formulation science, the ability to intelligently explore compositional parameter space provides the ability to greatly reduce the cost of creating structure−composition maps (phase diagrams). The approach has the potential to dramatically accelerate the phase-mapping process in multi-component i.e., industrially-relevant systems and enable the rational design of soft condensed matter systems. Indeed, as the authors note: "Dense grid sampling for such systems scales exponentially with the number of components, meaning that for a binary system that could be characterized with only 5 measurements, a ternary would require 25, a quaternary 125, and a 10-component system nearly 10 million measurements to obtain the same grid spacing."

4. Sample environments in detail

The below sections are detailed descriptions of advances in sample environments that have been used in neutron scattering for colloid and interface science. Some of the sections discuss several different devices; Tables 1 to 4 summarise a selection of those devices to provide a quick reference guide outlining key parameters, properties, and relevant primary literature.

4.1. Temperature

In terms of sample environment, temperature control and variation are the most common; Table 1 summarises a selection of sample environments used for temperature control. Although devices are available that cover the very low (e.g., 50 mK with dilution refrigerators) to several thousand Kelvin (vacuum furnaces) such extremes are typically unsuitable for soft matter applications. Beyond the relatively straightforward thermostatically controlled automatic sample changers connected to water or glycol baths, there are few examples of novel sample environments dedicated to temperature. An in situ differential scanning calorimeter based on a commercial unit has been developed by researchers at the Australian Nuclear Science and Technology Organisation (ANSTO) in combination with modified pans suitable for SANS transmission geometry (Fig. 4). The range is approximately −50 °C to 450 °C, the latter determined by the material limitations. A trigger at the start of a DSC run synchronises the event mode neutron collection with the DSC data enabling post-experimental time binning to match that of the DSC thermal transitions. It was successfully demonstrated on measurements of blends of hydrogenated and deuterated paraffins that had previously undergone local phase separation to form a modulated

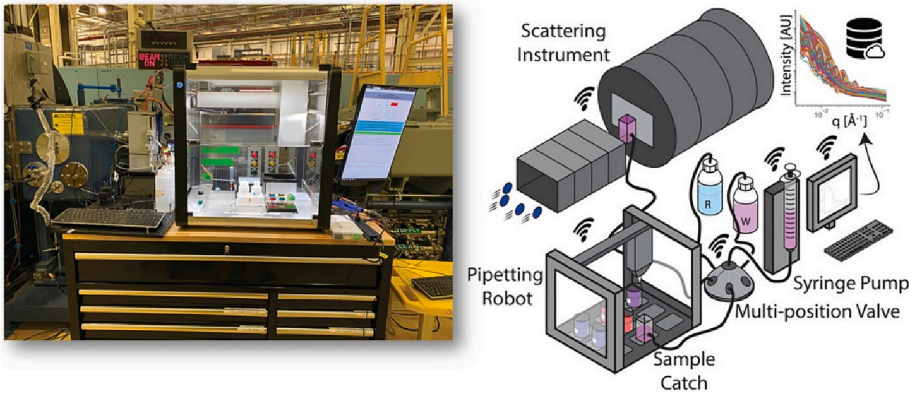

Fig. 3. Photograph and schematic of 'Autonomous Formulation Laboratory' for the automated synthesis and measurement of complex liquid mixtures. Reprinted with permission from The Autonomous Formulation Laboratory: An Open Liquid Handling Platform for Formulation Discovery Using X-ray and Neutron Scattering. Reprinted with permission from [76] Chem. Mater. 35, 846–852 Copyright 2023, American Chemical Society.

Table 1
A summary of selected devices for controlling temperature for neutron scattering experiments in soft matter applications.

Device	Temperature Range	Scattering Techniques	Notes	References
DSC-SANS	220–720 K	SANS	Simultaneous DSC and SANS	[12]
DSC-QENS	10–300 K	QENS	Simultaneous DSC and QENS	[77]
T-jump cell	293–550 K	SANS	Large temperature jumps of approximately 100 K	[79]
RHQC	150–600 K	SANS	Rapid temperature jumps above and below ambient	[78]

Table 2
A summary of selected pressure devices used for neutron scattering experiments.

Device	Maximum pressure	Scattering Techniques	Notes	References
High pressure cell for biomacromolecules	500 MPa	SANS	Operational temperature of 255 to 353 K	[83]
High pressure cell	600 MPa	SANS	Uses metallic windows	[86]
Versatile pressure and temperature-controlled cell	1 MPa	SANS and NR	Temperatures up to 623 K	[87]
Stroboscopic high-pressure cell	30 MPa	SANS	283 to 323 K	[91]
Flow-through compression cell	60 MPa	SANS and USANS	Automated control and data output of stress and pore pressure with time	[93]
Hydraulic cell	40 MPa	Neutron tomography	Custom cell used for tomography measurements	[94]
Environmental pressure cell	100 MPa	SANS and USANS	Liquid nitrogen cooling	[96]
High-pressure cell	12.5 MPa	NR	Temperature up to 358 K	[101]
High-pressure cell	140 MPa	NR	Uses a temperature controller	[100]
High-pressure cell	100 MPa	NR	Test fluid separated from hydraulic fluid	[102]
High-pressure cell	250 MPa	NR	Temperature control by a circulating water bath	[105]
High-pressure cell	200 MPa	NR	Temperatures up to 473 K	[106]
High-pressure cell	50 MPa	NR	Low sample volume	[107]

Table 3
A summary of selected shear cells and tribology devices for colloid and interface experiments suitable for neutron scattering and associated techniques.

Device	Type / geometry	Scattering Techniques	Notes	References
Flow cell	Couette	SANS	Special cell to access 1–2 geometry	[116]
Rheometer	Plate-plate	SANS	Use for steady and oscillatory shear.	[117]
shear-SAS cell	Taylor-Couette, cone-plate, plate-plate	SANS, SESANS, SAXS	A device for using multiple shear geometries and can be used for neutron and X-ray studies	[118]
Rapid ViscoAnalyser	Couette-like	SANS	Ability to ramp shear and temperature; uses an impeller	[41]
Recirculation flow cell	Poiseuille flow	SANS	Poiseuille flow cell for studying polymer melts	[119]
Microfluidic cells	Microfluidics	SANS	Small volume measurements under flow	[122–124,156]
Poiseuille shear flow cell	Poiseuille flow	NR and GI-SANS	Solid-liquid cells for Poiseuille flow	[132–134]
Rheometer for NR experiments	Cone-plate	NR and GI-SANS	Commercial rheometer used for NR experiments	[135]
Shear cell for NR studies	Cone-plate	NR	Shear cell can be used in combination with ATR-FTIR spectroscopy	[140]
Tribometer	N/A	NR and XRR	Use of a roller to measure shear in surfactant solutions in contact with surfaces	[142]

superstructure [12] but has been used for other materials including surfactants in deep eutectic solvents. More recently, Fornalski et al. [77] developed a cryogenic system which will allow the simultaneous measurement of calorimetric transitions and QENS measurements over a temperature range from 10 to 300 K. This presents design challenges beyond those for SANS including sample geometry since QENS detectors typically cover ~20–160° and thus favour a cylindrical, annular sample geometry. The sample cell therefore has an annular gap of 0.5 mm which also aims to minimise multiple scattering events. The current design is thus unsuitable for hydrogenated materials which commonly require a sample thickness of 0.1 mm but is ideally suited to deuterated materials or for hydrogenated surfactant micelles or model lipid membranes in D_2O.

Rapid heating or quenching into unstable or metastable states from which relaxation can be observed is another area of scientific interest. The RHQC – the abbreviation denoting Rapid Heat Quench Cell – has been developed for SANS that comprises two temperature reservoirs that can be controlled between 150 and 600 K [78]. A quartz SANS cuvette, of typical 1–2 mm path length, can be driven from one side to the other to generate a rapid increase or decrease in temperature whose rate is essentially determined by the thermal conductivity of the cell and associated sample. A similar hydrogenated-deuterated paraffin blend to that used for the DSC was used as a test sample but the best heating and cooling rates were achieved with an ideal indium sample. Earlier examples of rapid quenching to monitor crystallisation or separation in polymer systems are described in [79–81].

It is worthy of mention that, on occasion, the process of heating may, in itself, generate potential issues that have to be considered. A case in point in the study of drying in cement-based materials during simultaneous neutron and X-ray tomography. Here, the moisture extraction may generate airborne dust that could become radioactive when exposed to a neutron beam. Sleiman et al. [82] developed a novel heating cell with the principal functionality of heating the cement and concrete samples on their top surface, from which moisture is extracted. The materials and design were chosen to be as transparent as possible to both neutrons and X-rays but while also fulfilling safety requirements by being equipped with an exhaust tube connected to a vacuum system.

Table 4
A summary of devices used for experiments with ultraviolet, visible and infrared light in conjunction with neutron scattering experiments.

Device	Wavelength / Energy	Scattering Techniques	Notes	References
DLS	633, 642, 658 nm	SANS	DLS scattering angles ranging from 71° to 120°	[163,165–167]
DLS	633 nm	SANS	DLS scattering angle of 138° and used in combination with a pressure cell up to 500 MPa	[162]
DLS	532, 633 nm	Neutron spin-echo spectroscopy	DLS scattering angles of 75°, 100°, 115°	[168]
UV–visible spectroscopy	365 nm, 436 nm	SANS	In situ simultaneous UV–vis spectroscopy and SANS	[169]
UV–visible spectroscopy	200 to 850 nm	SANS	In situ simultaneous UV–vis spectroscopy and SANS	[170]
UV–visible light irradiation	LED source: 367, 408, 441, 521 nm Hg lamp: 248, 313, 365, 405, 436 nm Xe lamp 380, 440, 550, 650 nm	NR	Light irradiation of samples for NR studies	[172]
FTIR	4000 to 400 cm^{-1}	SANS	Simultaneous FTIR spectroscopy and SANS	[167,185]
ATR-FTIR	4000 to 400 cm^{-1}	NR	Attenuated total reflectance geometry for simultaneous NR measurements at solid-liquid and air-solid interfaces. Bands below approximately 1500 cm^{-1} will be affected by silicon transmission.	[186]
IRRAS	4000 to 900 cm^{-1}	NR	Infrared reflection absorption spectroscopy at air-liquid interfaces.	[192]
Ellipsometry	400 to 1000 nm	NR	Angle of incidence fixed at 70° for ellipsometry. Cell can be used in combination with FTIR spectroscopy and NR.	[195]

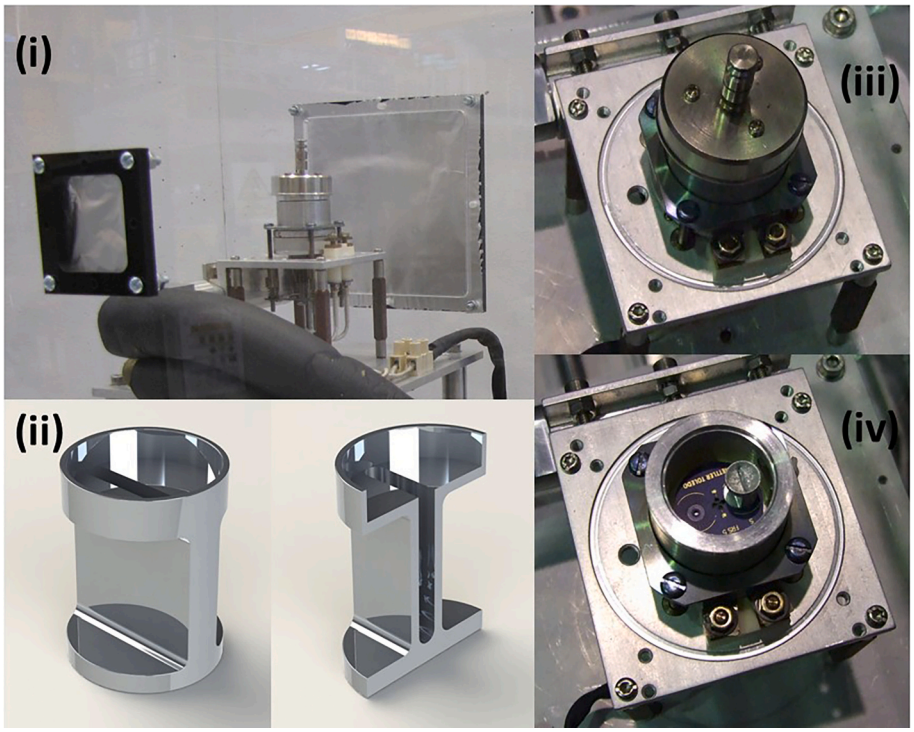

Fig. 4. Modified commercial DSC for use with SANS [12]. (i) The furnace assembly is placed inside a Perspex box that may be continuously flushed with a low flow of dry nitrogen gas to enable studies below the dew point. To allow the incident and scattered neutron beams into and out of the perspex box, simple aluminium foil windows are used. (ii) Crucibles to enable transmission geometry for SANS. (iii) DSC furnace with lid to maintain thermal stability; (iv) Furnace lid removed showing crucible located on 'sample' measuring position.

4.2. Pressure

The manipulation of pressure is enormously important to the behaviour of colloidal and interfacially-relevant materials. Table 2 summarises a selection of the pressure equipment discussed in this section. Pressure cells can be categorised based on their mechanism for pressure transfer, range, sample volume required and associated temperature. Teixeira et al. [83] describe pressure cells in the context of biological macromolecules that are designed to work up to 500 MPa, equivalent to 5 kbar, a pressure insufficient to break covalent bonds. A cell designed to simultaneously operate at temperatures between 255 K and 353 K for SANS has been used to study the high pressure, low temperature-induced unfolding and aggregation of two monoclonal antibodies where the extent to which the native secondary structure was preserved after incubation was independent of the extent of tertiary unfolding and reversibility [84]. Several combinations of pressure and

temperature were used to discern the respective contributions of the isolated antibody fragments to unfolding and aggregation that showed significantly different partial unfolding profiles and reversibility. Gomes et al. [85] used the same approach to study two globular proteins (α-chymotrypsinogen and ovalbumin) and a model monoclonal antibody (anti-streptavidin). Annighöfer et al. [86] describe a high pressure cell comprising windows of a $TiAl_6V_4$ ELI ("Extra-Low-Interstitial" version for lower impurities) metallic alloy to investigate the structure of molecular solutions up to 600 MPa – a somewhat higher pressure than is suitable for single crystals of sapphire - and demonstrated its use for SANS from myoglobin. More recently, Bannenberg et al. [87] designed a cell suitable for both SANS and neutron reflectometry that can be pressurized up to a more modest 1 MPa (10 bar), but temperature controlled up to 350 °C which also is compatible with simultaneous optical transmission and resistivity measurements. Supercritical CO_2 is a promising green solvent in organic synthesis, dry cleaning and nanomaterial processing due to a range of factors including low cost, non-flammability, environmentally benign characteristics and natural abundance [88]. However, the low solubility in CO_2, particularly of polar compounds has limited its use. Consequently, extensive studies have been conducted on water-in-supercritical CO_2-microemulsions exploring a range of surfactant systems over a number of years, most notably by Eastoe and Sagisaka [89,90]. Many of these investigations have used a cell which pressurises using CO_2 with the ability to operate up to 60 MPa or, with stirring, up to 40 MPa while temperature control is enabled between 10 and 25 °C with electrical heaters allowing the cell to reach 150 °C. A rather elegant combination of high-pressure studies and time resolution is monitoring the kinetics of induced structural changes in critical or near critical CO_2-microemulsions. Here, Müller et al. [91] used a high pressure SANS cell combined with a stroboscopic technique which provides a time resolution of 50 milliseconds to apply up to 10 Hz pressure jumps with adjustable amplitude (up to 35 MPa) and duration. They report two different mechanisms of structural reorganization of the initial spherical microemulsion particles under compression and expansion; compression-induced formation of the elongated structures is connected to a slow growth of cylinders, while the much faster expansion-induced break-down of the elongated structures into spherical CO_2-swollen micelles is proposed to be facilitated by undulations of the amphiphilic film.

Pressure jump SANS with millisecond time resolution has been used to study the rapid volume phase transition kinetics of *N*-*n*-propylacrylamide microgels [92] to resolve their collapse and swelling kinetics. Such materials are relevant to the production of nano-actuators, sensors or drug carriers. To obtain fine time resolution, pressure jump cycles were repeated 5400 times on a device designed by the Institute of Physical Chemistry at the University of Cologne. The cell is capable of achieving pressures up to 30 MPa and by connecting the casing of the pressure cell to a thermostat, temperatures between 5 and 70 °C can be achieved with an accuracy of $\Delta T = \pm 0.1$ °C. Wrede et al. [92] show that the pressure-induced swelling of the poly(NNPAM) microgels can be deduced from the shift of the oscillations to smaller q-values and a shift of the Guinier region while a lower scattering intensity at higher pressures arises from a decrease in contrast. Particle collapse/deswelling is much slower (by a factor of at least 10) than the swelling process; this behaviour is most-likely related to an inhomogeneous collapse of the microgels due to the non-equal distribution of the cross-linker content throughout the whole particle.

Pressure is also enormously important in the study of gas and liquid transport in porous media including hydrocarbon recovery. Hjelm et al. [93] report on the design of a compression cell, which provides compressive stress and hydrostatic pressures with effective stress up to 60 MPa, enabling the effects of stress vectors parallel to the neutron beam to be explored. The cell is demonstrated for a 300 μm thick sample of shale mounted on 24.5 mm diameter quartz discs surrounded by mixtures of hydrogenated and deuterated water. A somewhat less elaborate approach at much lower pressures has been employed by Etxegarai et al. [94] but interestingly combined with neutron tomography to study fluid flow in porous rocks. Blach et al. [95–97] have also employed pressure cells over a number of years to study the porosity of geological materials often combined with pressurized deuterated methane to manipulate contrast within open pores. In this context, one must also mention the extensive contributions of Melnichenko in the study of such materials, as well as polymers and supercritical CO_2 microemulsions [98]; Melnichenko addresses many such applications of high pressure, as well as a summary of pressure cells, in his 2015 book [99].

Pressure can be applied to surfaces and interfaces in a variety of ways; the design of pressure vessels has evolved over time starting with the cells of Koga et al. [100] and Gupta et al. [101] which consisted of a steel body with sapphire windows for neutron beam transmission. The cells were used to study the absorption of supercritical fluids into polymer films and the pressure was applied using pure carbon dioxide gas and a hand-operated syringe pump to achieve pressures up to 12.5 MPa and 140 MPa (for Gupta and Koga respectively). Designs of pressure cells have encompassed various approaches to exert pressure on a surface uniformly. This includes work by Kreuzer et al. [102] which used liquid to apply pressures up to 100 MPa at the solid-liquid interface, which is a convenient pressure for studying many biochemical processes [103,104]. In this design the fluid applying the pressure is separated from the fluid that is in contact with the surface; the same approach has also been used by Jeworrek et al. [105] for applying higher pressures of up to 250 MPa. Associated temperatures are typically controlled using circulating water baths limiting the temperature range at which the cell can operate. Wang et al. [106] designed and implemented a pressure cell that can reach pressures of 200 MPa and temperatures of 200 °C so that the cell is more suited to studying non-biological materials particularly geological systems. Carmichael et al. [107] have designed a cell for pressures up to 50 MPa for studying supercritical fluids in contact with surfaces; in this design the beam passes through the crystal of interest without the need for additional windows and has a low fluid volume of 0.1 mL which improves background and reduces beam attenuation.

Examples of successful pressure application to interfaces includes the work by Micciulla et al. [108] where the phase change in collapsible polymers brushes was observed as pressure was applied. Using the cell described by Jeworrek et al. [105] two different polymer brushes were studied under a range of temperatures and pressures to find the effect of pressure on the collapse point from a swollen hydrated phase to a collapsed dehydrated state. Using thermo-responsive poly(N-isopropylacrylamide) (PNIPAM) brushes, it was found that applied pressure had little effect on the structure below the collapse temperature as the brushes always remained extended and hydrated up to 160 MPa. Above the collapse temperature, pressure also had little effect with the brushes always remaining in a dehydrated collapsed state. However, at temperatures close to the collapse temperature, PNIPAM brushes were observed to swell and become more hydrated at low pressures but started to collapse and hydrate at high pressures. Through careful analysis it was found that the behaviour of the brushes under different pressures and temperatures behave in the same way as in solution.

Adsorption of proteins into polymer brushes through the application of pressure has also been investigated using NR [109]. For the adsorption of α-chymotrypsin onto polyacrylic acid (PAA) brushes, up to 100 MPa, enzymatic activity increases have been evaluated using total internal reflection fluorescence spectroscopy. The structure of the adsorbed protein to the PAA brushes was investigated using NR and it was found that the adsorbed mass per unit area decreased with increasing pressure and that the mass loss was not reversible once the pressure was reduced. The changes in activity and adsorbed mass are due to a negative volume change of adsorption up to 100 MPa which is where distortions in the active site change the behaviour of the enzyme.

For films at the air-liquid interface, surface pressures can be applied laterally to a film. This is usually done using a Langmuir trough. There have recently been extensive reviews on combining NR and Langmuir

monolayers [110] so this will only be covered briefly here. A Langmuir trough consists of a PTFE trough in which water or aqueous solutions can be filled and with a set of moveable barriers that can compress (or expand) a deposited monolayer. The change in surface pressure is measured with a Wilhelmy plate made typically of platinum or filter paper connected to a microbalance sensor. The change in surface pressure is usually measured as a function of the change in molecular area as the barriers move to change the area that the monolayer occupies. NR and GI-SANS can be conducted on Langmuir monolayers at different surface pressures to obtain the thickness and composition of the monolayer. Recent examples from biological systems include determining the location of proteins within model membranes such as the chloride intracellular ion channel protein (CLIC1) bound to phospholipid monolayers with different sterol compositions [111] and the binding of antimicrobial peptides to model bacterial membranes [112]. Some non-biological examples include the formation of polymer networks at air-water interfaces through UV irradiation [113] and studying the pH effects of *co*-polymers at the air-water interface [114].

4.3. Flow, shear, and tribology

It is important to draw the distinction between studies which aim to investigate structural changes occurring as a result of flow and those that may, in addition, enable potential insight into stresses that occur as a result that govern the bulk rheological properties. For more on this, the reader is directed to the excellent review on Flow-SANS and Rheo-SANS applied to soft matter by Eberle et al. [115].

The majority of soft matter studies concerned with flow-mediated SANS have involved Couette geometry. In this approach, measuring the axis torque allows quantitative measurements of shear stress simultaneously with macroscopic strain gradients imposed by the frequency of rotation while the sub-microscopic deformation is measured in the SANS. In Couette geometry, one can describe three planes of interest, namely 1–3, 2–3 and 1–2 and where the 1-, 2- and 3-directions are co-ordinate indices representing the flow velocity (v), velocity gradient (Δv), and vorticity (ω) directions, respectively (Fig. 5i). A standard Couette cell has a vertical geometry in which two configurations are possible. In the first, the incident beam is normal to the 1–3 plane and aligned along the direction of the velocity gradient; this is referred to as radial geometry. In the second, the beam is normal to the 2–3 plane and along the flow direction; this is referred to as tangential geometry. These cells can impose a constant shear flow from which the associated changes in SANS can be studied. Less common but still widely available is a cell from which a stress can be simultaneously measured; the latter can then be related to the bulk rheology to perform so-called rheo-SANS. These devices are generally only available for low viscosity fluids in the temperature range from around −20 °C to 200 °C.

The 1–2 plane is not accessible in vertically oriented Couette geometry and more specialised flow cells have been developed [116] to create a horizontal geometry that gives access to the 1–2 plane only. This technologically most relevant geometry also allows for unique spatial resolution along the velocity gradient where the structure and composition can vary significantly. A 1–2 cell with 5 mm path length was used in combination with beam sizes of 0.5 mm width by 3 mm height to study the formation of multilamellar vesicles from the lamellar phase of the nonionic surfactant system C12E5/D_2O under shear flow. Plate-plate rheometers have also been developed for use on SANS instruments to access the 1–2 plane under steady and oscillatory shear and is particularly useful for studying high viscosity polymer blends [117].

Velichko et al. [118] have designed a shear cell suitable for both SANS, spin echo SANS (by minimising any stray magnetic fields from the motor drive) and SAXS. The device is mainly intended for experiments in 1–2 plane geometry but can also be modified into cone–plate and plate–plate rheological geometries, giving access to the 1–3 scattering plane. The device can be operated from 5 to 100 °C and has been used to study a range of food materials under shear including cellulose suspensions, fat crystal networks and milk proteins although SANS has only been used to study the latter.

A highly applied but somewhat related sample environment that seeks to follow structural changes under flow is a Rapid ViscoAnalyser that has been modified for SANS [41]. The device is a viscometer with the ability to ramp temperature and apply variable shear with a

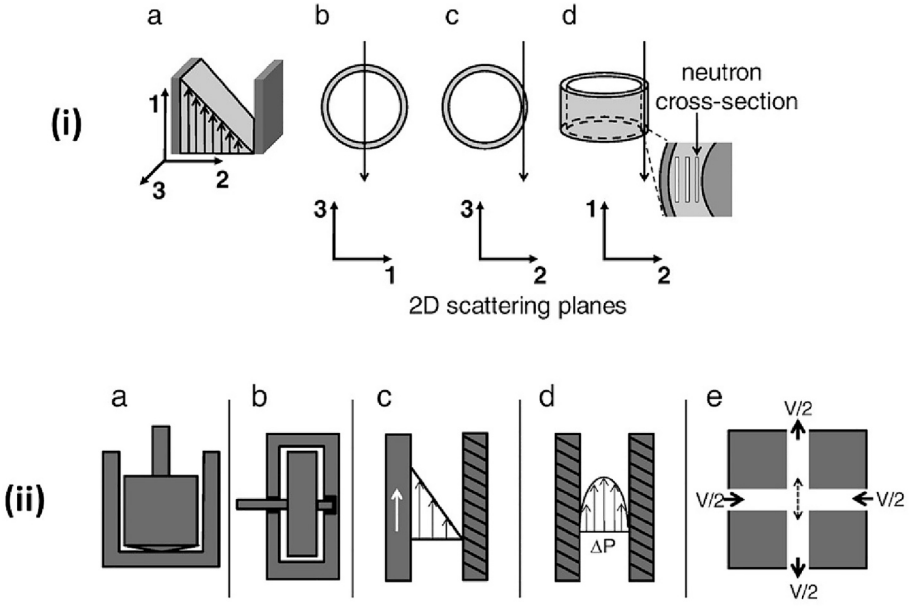

Fig. 5. (i) The common Couette flow cell geometries with accessible scattering planes. (a) Rectilinear coordinate frame where the 1-, 2-, and 3-directions are defined as the velocity (v), velocity gradient (Δv), and vorticity (ω) directions, respectively. (b), (c), and (d) are the radial, tangential, and 1–2 plane flow cell geometries that allow for scattering along the 1–3, 2–3, and 1–2 planes, respectively. In the latter, an incident beam cross-section smaller than the fluid gap allows for spatial resolution along the gap. (ii) Cross-section of the common flow-SANS sample environments, (a) Couette cell, (b) 1–2 plane shear cell, (c) sliding plate, (d) Poiseuille flow and capillary pressure driven flow, and (e) opposing jet flow cell where V is the volumetric flow rate. Reprinted from [115] Current Opinion in Colloid & Interface Science Vol. 17, Eberle and Porcar, Flow-SANS and Rheo-SANS applied to soft matter, 33, Copyright (2012), with permission from Elsevier.

capability optimized for testing the viscous properties of starch, grain, dairy products and other foods. The original design controls the rotation of a pitched paddle impeller which ensures that slurries and viscous materials are suspended during a controlled heating and cooling process. To enable its use for SANS, several modifications were required. Firstly, the pitched paddle impeller was modified both to minimise scattering from the paddle itself and to ensure minimal multiple scattering. To do this, the original plastic paddle, which would be a source of significant neutron scattering due to the large hydrogen content of the material, was replaced by one constructed from aluminium (and, subsequently from 3D printed titanium). Furthermore, a hollow, cylindrical band was incorporated into the centre of the paddle to ensure a scattering path length of 1 mm on either side between the outer surface of the paddle and the inner surface of the surrounding aluminium can. This dramatically modified the flow characteristics towards a more Couette-like geometry. Finally, a hole was drilled through the heating block to enable passage of the neutron beam around which borated aluminium shielding was installed to minimise activation along with an upstream cadmium aperture. The device has been successfully used to correlate the structural changes with viscometric behaviour during the cooking and subsequently cooling of a variety of different starches.

In contrast to the above 'drag' flow fields, Pouiseulle flow (Fig. 5 ii) is pressure driven; the associated flow between two parallel plates results in a hyperbolic velocity profile with a maximum in the shear rate at the boundaries and equal to zero at the centre line. To perform measurements on high viscosity fluids at extreme temperatures, a less recent example is a Poiseuille flow cell for SANS developed for investigations of polymer melts at pressures up to 10 MPa, temperatures up to 230 °C, and a melt viscosity up to 65 kPa.s [119]. Other specialised flow cells exist such as capillary flow, which is similar to Pouiseulle, and jet flow where two opposing fluid streams converge and then exit at directions normal to the inlet. This is discussed in more detail in Eberle and Porcar [115]. Bharati et al. [120] discuss recent developments in Poiseuille flow and extensional flow small-angle scattering.

Based on an original microfluidic design, Corona et al. [121] developed a cross-slot flow cell (Fig. 5 ii); by changing the flow directions of four inlets or outlets, it is possible to generate near-2D steady state flows with a range of variable flow types within a single device: including shear flow, extensional flow and rotational flow. In combination with SANS, they investigated the flow-induced changes in a variety of systems including Newtonian fluids (both glycerol and D_2O), an inelastic shear thinning fluid (cellulose nanocrystal dispersions), a yield stress fluid (Carbopol 934), an elastic (Boger) fluid (polyethylene glycol) and a viscoelastic fluid (sodium nitrate and hexadecyltrimetylammonium bromide solution).

Microfluidic devices also play an important role as sample environments. They can be employed to study the response of materials to flow, i.e., the molecular or mesoscopic bases for complex fluid rheology and processing, but also to both speed up traditional SANS experiments (e.g., phase-space exploration) and explore the mechanisms and kinetics of phase and conformation transition kinetics [122]. An example of the latter by Adamo et al. [123] will be discussed below in the context of chemical reactions.

Lopez et al. [124] performed experiments on two model complex fluids, cetyl trimethylammonium chloride/pentanol/D2O and sodium lauryl sulphate/octanol/brine lamellar systems to study the molecular re-orientation and alignment underpinning the flow response under contraction-expansion geometries. The latter system was compared under continuous and oscillatory microfluidic contraction–expansion flows; the authors investigated the influence of varying flow velocity, oscillation amplitude, frequency, and number of oscillatory cycles on the lamellar-to-multilamellar vesicle (MLV) transition [125]. A SANS beam footprint of 175 μm × 420 μm probes a scattering volume of 22 nL. They subsequently explored the influence of material selection on microfluidic device fabrication on a range of performance factors for SANS including neutron absorption, scattering background and activation, spatial resolution, chemical compatibility, pressure resistance, cost, durability and manufacturability [122]; they also describe the range of flow systems available in combination with SANS. More recently Fischer et al., [126] have used microfluidics in combination with SANS to study the shear-induced sponge-to-lamellar phase transition in bicontinuous microemulsions. It was demonstrated that, as the velocity gradient increases, the number of inter-lamellar connections disappears resulting in the structure tending to form lamellar phases.

Weston et al. [127] have developed a slit rheometer for neutron scattering (described as μRheoSANS) comprising a linear flow cell of 100 μm path length in which the pressure drop between the entrance and exit, across the cell channel was monitored using microfluidic pressure sensors. The device, which is capable of achieving higher shear rates than conventional RheoSANS, was used to measure the structure of a semi-dilute surfactant solution of worm-like micelles during flow. A data analysis technique was required to isolate the scattering from the high-shear region of the flow channel but good agreement was found between μRheoSANS and conventional RheoSANS. The authors state that further development could occur to increase the maximum pressure the channel can contain from ≈ 3.5 bar to 350 bar, the maximum shear rate the channel can probe from $\approx 1.5 \times 10^5\ s^{-1}$ to approximately $1.5 \times 10^6\ s^{-1}$ and the ability to control sample temperature in a range from 0 to 150 °C. Many of these same authors report on the development of SANS coupled to a capillary rheometer (Capillary RheoSANS') [128] to study the chaining of silica nanoparticles, the alignment of wormlike micelles and the aggregation of monoclonal antibodies. The device enables wall shear rates up to $10^6\ s^{-1}$ to be generated with measured pressure drops of up to 500 bar. In the cylindrical capillary geometry, the resulting scattering is a combined projection varying between the 1–3 and 1–2 planes. By combining capillary and rotational RheoSANS techniques, the relationship between nanostructure and rheology of complex fluids can be measured over eight orders of magnitude in shear rate from 10^{-2} to $10^6\ s^{-1}$.

Compared to rheometers for rheometric studies, microfluidic devices are a relatively inexpensive platform, requiring much smaller sample volumes and are perhaps somewhat easier to integrate. Although their application to complex fluid rheology and processing is still in its infancy, their use as sample environments is likely to grow as facilities with access to greater beam intensities, and thus the ability to use smaller beams or measure more rapidly, become available [122].

In all of these systems, it is intriguing to consider their combination with applied electric or magnetic fields to conduct studies relevant to rheo-electro or rheo-magneto applications. Indeed, Richards and Riley [129] review the field of dielectric rheoSANS which combines conventional rheoSANS with dielectric (or impedance) spectroscopy. To perform dielectric rheoSANS, measurements are made between the rotating cup and the stationary bob of a Couette cell using an impedance spectrometer that enables electrical measurements over a wide frequency range; the electrical contact under continuous rotation is maintained via a slip ring attached to the cup. Further details can be found in [130,131]. In the same way that a time-oscillatory shear deformation is imposed and the oscillatory stress response is measured to reveal storage and loss moduli, in impedance spectroscopy, when the sample is exposed to a time-oscillatory electrical excitation (i.e., voltage or current), the resulting oscillatory electrical response can be decomposed to obtain the complex impedance from which the real and imaginary parts of the permittivity are obtained. The system has been used to study a variety of soft matter systems including the electrically conducting polymer poly(3-hexylthiophene) (P3HT) in deuterated p-xylene. The authors detail the range of systems that would benefit from these tandem methods including conductive composites, polymer solutions and melts (exploiting molecular dipole moments) as well as microemulsions where electrical properties are often an indicator of microemulsion type (O/W or W/O) and connectivity (percolation and phase-inversion).

For NR shear across an interface can be achieved in several different

ways. Early studies implemented shear by using lateral flow across a silicon wafer under liquid in a Poiseuille flow cell [132–134]. Another method typically used has employed cone and plate geometry where the surface of interest forms the plate, and a stirrer is cone shaped, which has the advantage for allowing the incident and reflected beams through the sample environment. Whilst shear cells of this geometry can be made in-house, earlier work also involved setting up commercially available rheometers on beamlines as has been done by Wolff et al. [135] to investigate the packing arrangements of Pluronic F127 under shear on hydrophilic silica and hydrophobized silicon surfaces.

Shear can be conducted in oscillatory mode or under a steady mode. Both methods were used separately to investigate the formation of lamellar structures of AOT deposited onto a sapphire substate [136]. Using a cone and plate geometry it was found that the AOT structure at low concentrations was unaffected by the application of shear; however, at high concentrations the lamellar form of bilayer stacks that are formed by the AOT are lost over time under a steady shear. Under oscillatory shear some bilayers are lost from the surface, but an equilibrium structure is reached depending on the shear applied. Other materials that can also be investigated are shear-responsive polymers. Korolkovas et al. [137] used simultaneous rheology and NR to monitor the shear response of two entangled polymers of different chain lengths and grafting density. It is shown that the brushes collapse reversibly under shear, and using computer simulations, that solution dynamics play an important role in creating shear responsive polymer brushes.

Many of the valuable properties of biomaterials involve their use under shear [138]. Hamley et al. [139] applied rheology and GI-SANS to investigate the formation of protein nanotubes on a silicon surface using a cone and plate geometry. The protein nanotubes form an ordered structure on the surface under shear and the alignment of the tubules is similar to those found in solution using a Couette cell. Shear in combination with NR has also been used to investigate properties of mimics to synovial fluid that is found between mammalian bone joints. Stacked phospholipid bilayers are created on a silicon surface and the fluid gaps between each bilayer filled with poly(allylamine hydrochloride) (PAH) which mimics the hyaluronic acid found in synovial fluid. It was found the system with PAH present in the spacing between phospholipid bilayers increased the mechanical stability of the bilayer stacks by a factor of four with respect to the shear applied compared to bilayers with no PAH present [140].

Food materials are usually prepared under shear conditions and the interface with which the material is in contact can affect its structural arrangement. Using a cone and plate geometry, the crystalline structure of cocoa butter on a silicon surface under shear flow has been investigated using NR [141]. It was found at 40 °C under a shear rate of 500 s^{-1} the commercially desirable type *V* structure of the cocoa butter forms (a tri-layer structure of the triacylglycerides) whereas with no shear the type III structure is formed (a bilayer structure). Upon cooling to 25 °C under shear it was found that the type V structure continues to grow rapidly whereas the type III structure continued to grow under shear more slowly. This work showed that the formation of type V cocoa butter structures occurs more rapidly under shear at interfaces than in bulk.

Armstrong et al. [142] have recently created a novel design for measuring shear on surfactant layers deposited on iron-coated silicon wafers (Fig. 6). The tribometer comprises a PEEK roller between the substrate of interest and a liquid trough containing a solution of surfactant (Fig. 2). Laser displacement sensors are used to ensure that an even gap is maintained between the roller and the substrate. As the roller spins the substrate becomes coated with the surfactant solution and is then deposited onto the iron surface and maintains a shear force. For reflectometry the incident neutron beam is directed through the substrate. The apparatus was also demonstrated for use for X-ray reflectometry, in which case, the incident beam is directed along the liquid filled gap between the roller and the substrate. Two different subphases were tested. The first was deuterated dodecane oil using two different shear rates;the second was GMO in dodecane solution which is often used as an additive for engine oils. It was found that at the low shear rates an additional layer was needed to be included in the model and that the higher shear rate the GMO could be described using a single layer.

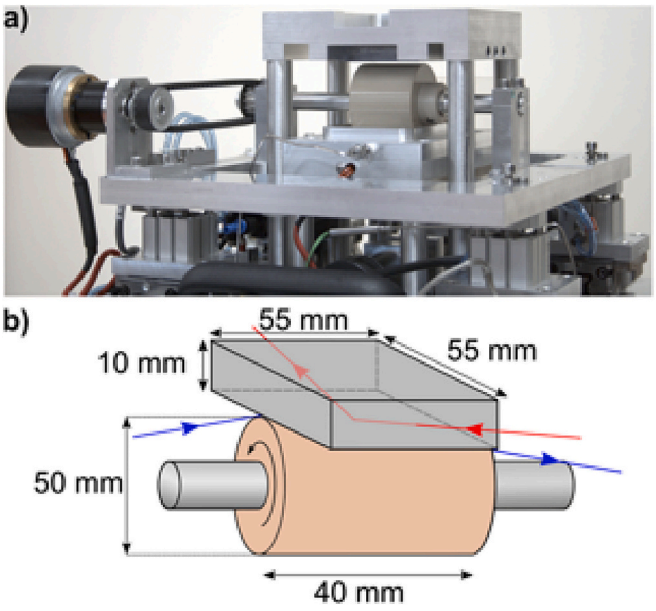

Fig. 6. Photograph (a) and schematic (b) of the tribometer by Armstrong et al. [142]. Figure adapted from the original in [142] under Creative Commons Attribution 4.0 International License (http://creativecommons.org/licenses/by/4.0/).

Shear can also be applied to thin films at the air-liquid interface; a recent innovation by Tein and co-workers [143] have created a PTFE trough with four arms connected through a band, known as the quadrotrough, so that pure shear and dilatational strains can be determined. This trough has an advantage over conventional Langmuir troughs as shear and dilatational strain cannot be easily separated [144]. The quadrotrough has been adapted so that Brewster angle microscopy or NR can be simultaneously measured with shear and dilation/compression. The shear direction is determined by the direction of the pairs of barrier arms and whether the Wilhelmy plate is perpendicular or parallel to the extensional axes. The use of the trough was demonstrated by using deuterated stearic acid monolayers on a subphase of pure water or a dilute solution of aluminium nitrate. Stearic acid on a pure water subphase showed negligible shear elasticity whilst on the dilute aluminium nitrate subphase shear elasticity could be observed. The ability to use the quadrotrough on a NR beamline was demonstrated; measurements showed that there were no significant changes in the structure of the deuterated stearic acid monolayer under shear strain.

With the majority of approaches listed above, the combination of data collection in event mode would enable information to be gained during transient structural reorientation of complex fluids e.g., stress relaxation following steady shear or via time resolved small- and large-amplitude oscillatory rheology. Table 3 summarises many of the devices and their key characteristics from this section.

4.4. Tensile testing

Uniaxial mechanical deformation studies are widespread in the polymer sciences. To obtain quantitative information during combined neutron studies, one needs to ensure that sample is uniform over its entire volume and not merely at the beam position. In addition, one must also consider whether it is appropriate to subject the material to discontinuous variations in deformation i.e., to deform the material up to a certain value, collect the data and then proceed to deform. This

approach is really only suitable for materials where relaxation times are long compared to the data collection time. In other cases, different approaches are required, and this is even more the case when the deformation force is completely removed, and the material is allowed to relax. Ideally, a continuous deformation approach with simultaneous data collection in streaming mode should be pursued. This is described in more detail in [5]. Other factors to consider are controlled temperature and humidity, the latter is discussed below. A final factor for consideration is whether the sample position is constant during stretching. López-Barrón et al. [145] have investigated a series of hydrogenated and deuterated polystyrene blends during uniaxial extensional flow using a strain-controlled Sentmanat extensional rheometer (SER) to track the stress response (Fig. 7). SANS measurements were performed in a time-resolved mode during the startup and cessation of deformation steps of 5 s duration with measurements repeated five times to obtain sufficient statistics; the data were subsequently divided into a number of logarithmic time bins. They show that strain hardening is directly related to chain stretching and obtain an empirical linear relation between the alignment factor and strain hardening ratio. Similarly, Lam et al. [146] have investigated the scaling behaviour of the anisotropic relaxation following uniaxial stretching of blends of hydrogenated and deuterated polystyrene of three different molecular weights; they found that conformational relaxation at relatively high q and short time can be described by a simple scaling law with the relaxation rate proportional to q that is indicative of a weak influence of entanglement. In other work, López-Barrón et al. [147] studied blends of hydrogenated and deuterated linear low-density polyethylene using a Linkam TST350 tensile stage equipped with a 200 N load cell. Three regimes of alignment were identified: (i) initial strains in the elastic regime show significant chain stretching, followed by (ii) a slower but continuous increase in the total orientation during plastic deformation, and (iii) a final stage where further chain stretching stops at the onset of strain hardening. Differences in alignment between the low and high molecular weight fractions in the polymer are observed along with amorphous chain recoil and loss of orientation upon long time relaxation.

The SMART process, where SMART refers to shear motion-assisted robust transfer, involves the creation and subsequent transfer of free standing films to a tensile stage with the intent to assess the mechanics of free-standing thin polymer films (< 100 nm in thickness) that are either stiff or viscoelastic [148]. Films that were stretched to different thickness were floated onto a water surface for NR measurements to assess water uptake and hydration. A future possibility for tensile testing of thin films for NR studies is film stretching in situ on the neutron beam.

4.5. Ultrasound, chemical reactions and stop flow

Ultrasound refers to sound with frequencies >20 kHz. Beyond medical research and diagnostics, it can be used for cleaning, mixing, and accelerating chemical processes. The mechanical stresses used in sonication are the result of the formation and violent collapse of vapour cavities in a process known as cavitation. Cavitation is often associated with high localized pressures, stresses, and temperatures in the vicinity of collapsing bubbles. These cavitation bubbles can cause local agitation, affecting a variety of processes including the acceleration of reactions (sono-chemistry) via localized heating and free radical formation, as well as the promotion of the formation of crystalline nuclei that can accelerate crystallisation (sono-crystallisation); in addition, it can be used to generate a time-dependent mechanical perturbation. Li et al. [149] developed an in situ ultrasound device for small angle scattering studies which was validated for SANS as well as USAXS (Fig. 8). In the latter design, two transmitting spherical-focus transducers generate ultrasounds operating at 1.24 MHz while a receiving PVDF transducer connected to an oscilloscope through a preamplifier is incorporated to identify any cavitation events or scattered acoustic signals. The transducers were activated in an alternating configuration to avoid sonophoresis from a single transducer (i.e., sample depletion in the scattering volume due to an acoustic radiation force) or sample enrichment at acoustic standing wave antinodes (i.e., during simultaneous transducer activation). Sonophoresis can result in the modification of the scattering intensity that could be incorrectly interpreted as a change in the structure. Potential options exist to trigger the SANS detector in pulsed mode for time-of-flight experiments without any changes to the electronics, or vary acoustic conditions (e.g., pulse repetition frequency, pulse duration, acoustic pressure, and frequency) while simultaneously monitoring structural changes in the sample via scattering. While they employed the device to study a range of materials

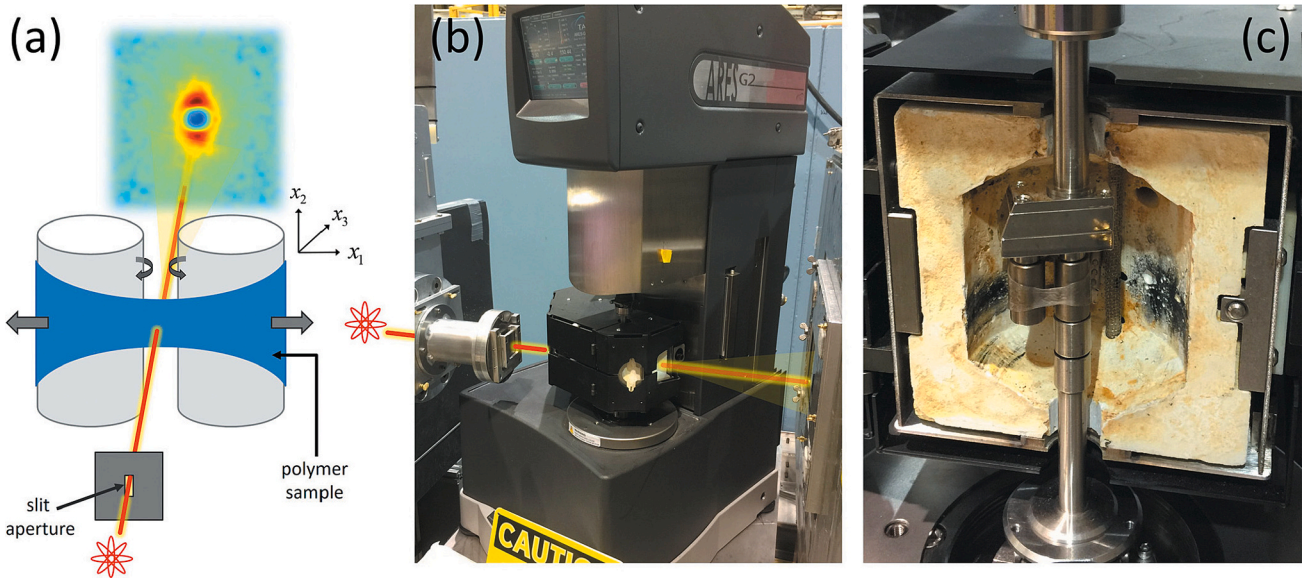

Fig. 7. (a) Schematic diagram of the extensional rheo-SANS configuration. (b) Photograph of rheometer with modified oven mounted on the SANS instrument. The direction of the neutron beam is illustrated with the red-yellow lines. (c) SER with a sample after stretching. Reprinted from [145] Chain stretching and recoiling during startup and cessation of extensional flow of bidisperse polystyrene blends, Carlos R. López-Barrón; Yiming Zeng; Jeffrey J. Richards, J. Rheol. 61, 697. Copyright (2017). The Society of Rheology. (For interpretation of the references to colour in this figure legend, the reader is referred to the web version of this article.)

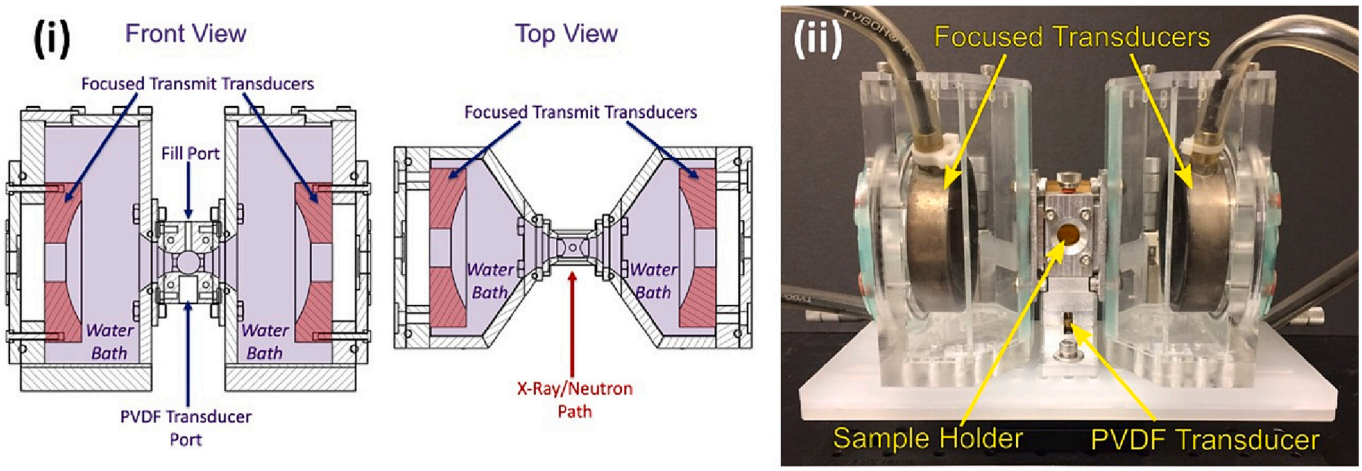

Fig. 8. Focused ultrasound sample environment: (i) front and top down slice views and (ii) photograph of device. The sample is held in an aluminium sample holder in the centre of the apparatus. 100 mm thin Kapton windows cover the front and back face of the sample holder through which the beam passes. Similarly, Kapton film windows are used on the left and right face of the sample holder for acoustic transmission. Beneath the sample holder is a custom built unfocused polyvinylidene (PVDF) transducer that is acoustically coupled to the aluminium body of the sample holder with ultrasound gel. Left and right of the sample holder are two chambers acoustically coupled to the primary sample holder with gel. Each chamber holds a focused transducer submerged in degassed water to insonate the sample. Adapted from [149].

including the emulsification of perfluorooctane in water via gold nanoparticle Pickering formation, the resuspension of dry silica particles in water and the sono-crystallisation of fullerenes, all data presented are from SAXS studies. Gupta et al. [150] designed an ultrasound cell for SANS that can fit inside standard sample environments thus maintaining access to a wide range of well-established controls such as temperature, humidity or magnetic fields. They explored its use to measure the time constant associated with SDS micellar self-assembly followed by ultrasound-induced disintegration at a fixed temperature. While outside the scope of this review, a resonant ultrasound spectroscopy device for in-situ neutron scattering measurements has been developed by ORNL [151]. When the drive frequency matches the frequency of a mechanical full-body resonance in a mm-cm sized sample, the result is large-amplitude surface vibrations and a strong peak in the ultrasound spectrum. The information provided can thereby non-destructively probe the elastic properties of mm-cm sized solids such as metals, ceramics and semiconductors and has been tested on the neutron diffractometer, NOMAD.

A system designed to enable the measurement of SANS during a chemical process has been developed by Hayward et al. [152]. The chemical reactor has a flow-through observation cell that enables the effects of changes in chemical composition, e.g., due to ongoing chemical reactions, to be measured continuously. Beyond the reaction vessel, the system includes a pH electrode, a peristaltic pump and two syringe pumps. Experiments were conducted on oligo-oxyethylene lauryl ether carboxylic acid which undergoes a dramatic structural transition between large vesicles and small micelles over a narrow pH range. The combination of high compositional precision and time-resolution allows for the exploration of non-equilibrium states that would not be measurable in a classical 'static' approach. It also facilitates systematic investigations to be conducted of unstable regions in phase diagrams such as the structural evolution in aqueous surfactant systems as a result of changes in pH and salt concentration. A vortex fluidic device comprises a rapidly rotating tube open to generate dynamic thin films at high rotational speed; the sub-millilitre volumes of liquid undergo high shear forces enabling modification of chemical reactions and processing, depending on the speed and orientation of the tube. Its operation has been studied with neutron radiography [153,154], while its functionality has been demonstrated with SANS on the production of Tween 20-based encapsulation of fish oil [155].

More recently, Adamo et al. [123] developed a microfluidics system as a rapid and precise liquid 'formulator' (Fig. 9). The system comprises a boron free microfluidic chip connected to three input lines (i1, i2 and carrier) in the form of a double T-junction. This is followed by a mixing channel and a 3 m long channel with hydrophilic channel walls. The carrier input provides a continuous, immiscible phase to segment the flow transport and the plugs along the serpentine channel. Inputs i1 and i2 are miscible and their ratio was changed to formulate the sample. Each input was connected to a syringe and an independent syringe pump driven by a custom-made script to precisely control the flowrates. The authors maintained a constant overall flowrate of i1 + i2 while the

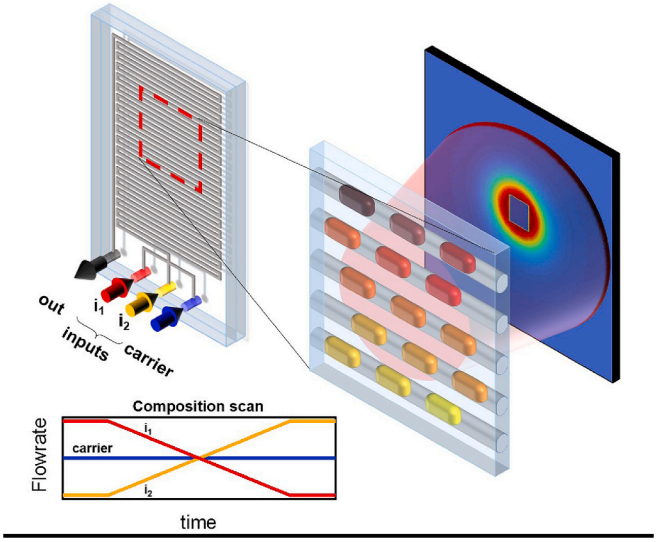

Fig. 9. Schematic of the droplet microfluidic setup for SANS: a microdevice is employed to formulate a large series of samples by varying the relative flowrates of inputs i1 and i2, while maintaining the flowrate of an immiscible (carrier) fluid constant, and segmenting the sample in discrete plugs, at a fixed total flowrate. For weakly scattering systems, the neutron beam illuminates a prescribed number of channels, indicated by the dashed red line, resulting in SANS data averaging over the sample volume and requiring optimisation of system parameters for precise phase mapping. Adapted from [123] with permission from the Royal Society of Chemistry. (For interpretation of the references to colour in this figure legend, the reader is referred to the web version of this article.)

relative flow rates were changed with time, as the flow rate of the carrier phase was kept constant to ensure consistent plug production. The illuminated sample area for SANS measurements was 66 mm^2 (100 mm^2 square beam covering 16 full channels and 2 partial channel widths) equivalent to a sample volume of 16.7 μL. The system was evaluated for both continuous and droplet flows on colloidal silica nanoparticles and in a range of droplet carrier phases. This approach enables rapid and precise contrast matching measurements as well as systematic dilution or composition scans, circumventing the traditional, sequential and time-consuming preparation of discrete samples, loading of cells and use of sample changers. Furthermore, microfluidic SANS also allows adaptive scanning of parameter space and possible feedback and optimization loops. The connection to machine learning is discussed in more detail below. The approach is an extension of work previously reported by these authors to demonstrate the ease of contrast variation and matching for H_2O/D_2O mixtures, 12 nm diameter SiO_2 particles and the sodium dodecyl sulphate solutions while continuously scanning the composition space during SANS data acquisition [156]; however, the approach is of limited use to viscous systems and certainly weakly scattering systems where typical acquisition times may require sample volumes of >20 mL. However, for typical samples, this microflow-SANS approach can result in improvements in the quantity of reagent required, the total experimental time as well as a significant improvement in the resolution of the contrast match point.

A further flow system is stop- or stopped-flow whereby multiple liquids, typically 2 or 3, may be mixed and the resultant changes measured following the generation of a trigger signal from which neutron data can be synchronised. After mixing a lamellar phase of the non-ionic surfactant, TX-100, and water, with toluene, SANS showed the formation of an initial oil-swollen lamellar phase which was found to subsequently evolve into a dense water-in-oil (w/o) microemulsion, during which time the two phases coexisted [157]. A more recent example, also with SANS, concerns the precipitation polymerisation of Poly(N-isopropylacrylamide) microgels [158]. A visual demonstration of how such a device works can be found in [159].

NMR has been combined with total neutron scattering studies on the Near- and InterMediate-Range Order Diffractometer (NIMROD) at the ISIS Pulsed Neutron and Muon Source (Rutherford Appleton Laboratory, United Kingdom) using the coupled total neutron scattering – NMR "NeuNMR" arrangement. The system has been used to investigate the catalytic heterogeneous reduction of benzene-d_6 with deuterium gas in 3 wt% Pt/MCM-41 [160] as well as the arrangement of molecules within molecular mixtures of cyclohexane and benzene in both the bulk liquid phase and when confined in MCM-41 mesopores [161].

4.6. Ultraviolet, visible, and infrared light (scattering, spectroscopy, and irradiation)

Dynamic light scattering (DLS) measures the fluctuations of scattered light intensity as a function of time from which an autocorrelation of the intensity from different time slices is performed. The initial slope of the autocorrelation function yields the diffusion coefficient and, via the Stokes–Einstein equation, the hydrodynamic radius. The latter value can be related to the radius of gyration obtained from SANS since these two radii are related to each other depending on the shape of particles. In addition, by combining SANS with DLS the stability of a sample can be tracked during extended neutron measurements and any aggregation can be identified. The technique provides size information from the sub-nm to approximately 10 μm. The ability to easily switch wavelength using modern solid-state lasers provide further opportunities for readily manipulating the accessible size range probed. A potential use of combined DLS and SANS includes the analysing of autocorrelation functions from DLS to reveal the translational diffusion coefficient whilst simultaneously accessing structural information from SANS. In-situ DLS has been implemented at a number of SANS instruments internationally including: SANS-I instrument at the SINQ spallation source (Paul-Scherrer Institute, PSI, Villigen, Switzerland) [162], D11 instrument at the Institut Laue-Langevin (ILL, Grenoble, France) [163,164], and LOQ and ZOOM instruments at ISIS [165]. However, the experimental configurations are not routine to install and implement and in most cases the equipment is assembled in a bespoke fashion for the particular experiment with DLS equipment supplied by the visiting scientists.

Schmid et al. [166] describe the development of combined SANS with DLS for FRM2 in Germany. The sample environment is equipped with two parallel setups for measuring dynamic light scattering at two different scattering angles of approximately 120 and 71°. Due to refraction at the cuvette–air and cuvette–solvent interfaces, the precise scattering angle is calculated using the refractive index of the solvent according to Snell's law for each temperature. It is noted that the light scattering plane is inclined by 20° relative to the SANS plane, to prevent problems arising from reflections from the cuvettes. Test DLS measurements were performed on polystyrene standard spheres with a radius of 25 nm and 200 nm and more advanced measurements on NIPMAM microgels during temperature-mediated swelling, although no combined SANS/DLS data were reported. A similar approach is described by Balacescu et al. [167]. DLS has also been implemented on the neutron spin echo spectrometer J-NSE Phoenix at FRM2 to enable both NSE data validation and to identify when a sample should be replaced when its aggregation state influences the spin echo measurement results [168]. Six different values of momentum transfer can be accessed by switching between two different laser colours enabling the equipment to also be used for static light scattering (Fig. 10). Test experiments were performed with silica nanoparticles with diameters ranging from 20 nm up to 300 nm. In addition, the aggregation state of apomyoglobin in heavy water, was monitored over hours and shown to have no influence on the spin echo measurements; the platform lends itself to the future implementation of other probes e.g., UV–visible spectroscopy.

A UV–Vis absorption system has been deployed on the TAIKAN SANS instrument at the Materials and Life Science Experimental Facility (MLF) at J-PARC in Japan; it comprises a mercury lamp, a lens system, an Al-coated quartz mirror, an in-house-built photodetector and a cuvette holder. Simultaneous measurement of SANS and UV–Vis absorption was conducted to follow the irradiation-induced structural changes of light-sensitive surfactant micelles formed by 4-butylazobenzene-40-(oxyethyl)trimethylammonium bromide in an aqueous solution [169] (Fig. 11). The latter molecule transforms from the *trans* to *cis* isomer under UV light irradiation; subsequent visible-light irradiation or thermal relaxation results in the recovery of the trans isomer. SANS data were continuously collected in event mode while the sample was irradiated first with UV light and then by visible light; the disintegration and subsequent reassembly of the spherical micelles was followed. Similarly, Kelly et al. [170] studied the self-assembly behaviour of azobenzene photo-surfactants. It was observed that tetraethylene glycol mono-(40,4-octyloxy,octyl-azobenzene) could switch between wormlike micelles (*trans* native state) and fractal aggregates (under UV light). Changes in the self-assembled structure arose concurrently with changes in the absorption spectrum; wormlike micelles could be recovered within 60 s of blue light illumination. In both these systems, the effect of irradiation mediates photo-isomerisation between *cis*- and *trans*- forms thus affecting molecular packing density for micelle formation.

UV and visible light irradiation is also possible for photosensitive samples that have been deposited onto surfaces. A sample environment has been created on the SHARAKU reflectometer at MLF where, using a series of different lamps or LED sources, thin film samples at the air-solid interface can be irradiated [171,172]. This apparatus has been used to investigate the photo-diffusion of silver through amorphous germanium sulphide films. Upon exposure to a light source silver ions diffuse through the germanium sulphide layer with the greatest diffusion observed at near UV wavelengths (367 nm) and with the silver layer completely diffused into the germanium sulphide [173]. Kinetic measurements can also be performed upon exposure to a UV or visible light

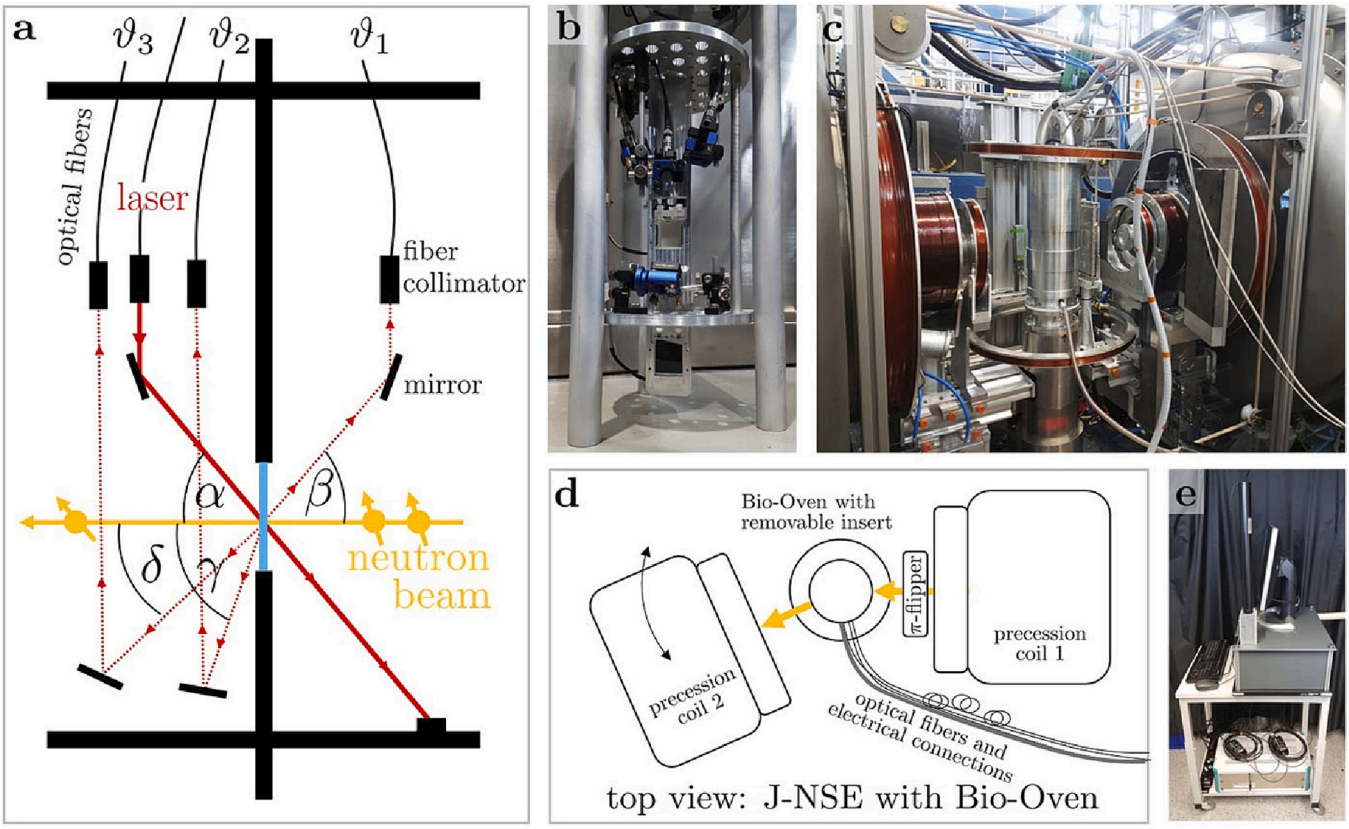

Fig. 10. The in situ DLS sample environment at the neutron spin echo spectrometer J-NSE Phoenix at FRM2. (a) Schematic cross section of the in situ DLS measurements with three scattering angles. The laser beam (red solid line) leaves the lens of the fibre collimator (black rectangle) and is guided by a mirror to the sample. The scattered light (red dashed lines) is redirected by mirrors and collected by collimators on the top. The neutron flight path is indicated with yellow arrows. (b) Photograph of the inset put onto an external holder. (c) Photograph of the J-NSE instrument with the mounted Bio-Oven, which is a light proof casing containing the inset shown in (a) and (b). (d) Schematic top view of the J-NSE instrument. (e) Photograph of the mobile cart carrying all components used for DLS measurements including an optical bench with laser and optics, detectors, correlator cards, laser safety interlock, and a PC. Figure reproduced from [168] under Creative Commons CC BY license. (For interpretation of the references to colour in this figure legend, the reader is referred to the web version of this article.)

source to investigate the exact nature of diffusive or reaction processes [174]; his can be done whilst the sample is under illumination or followed post-illumination.

A platform that encompasses even more complementary methods, namely UV–visible, fluorescence, and in-line density measurements is described by Dicko et al. [175]. The unit comprises a combined sample holder/fibre optic manifold in which flow-through cells can be mounted (Fig. 12). The design incorporates easy fibre optic alignment and multiple configurations, temperature control capability and an enclosure for efficient light exclusion. UV–visible and fluorescence measurements are mutually exclusive due to the background light that arises; however, both radiation sources have either a built-in shutter or filter wheel for their control. A proof-of-concept study was performed on solution mixtures of the fluorinated and hydrogenated surfactants, PFNA and Brij35 containing pyrene; pyrene has an excitation at 337 nm and fluorescence emission of approximately 450 nm typical of self-association. UV–visible transmission spectra indicated an increase in turbidity with increasing amounts of PFNA in the mixtures.

In situ photoluminescence and simultaneous NR have also been implemented for studying the structure of layered organic systems. Using a custom-built chamber, the photoluminescence equipment consists of a UV-LED source and a detector that is a fibre optic USB-powered spectrometer [176]. Photoluminescence measured simultaneously with NR has been used to study the morphology of dendrimer films upon the absorption of explosive analogues [176,177]. As the analogue binds to the dendrimer, the photoluminescence is quenched, and the NR measurements show that the analogues diffuse through the entirety of the dendrimer film. Simultaneous photoluminescence and NR have also been used to study organic light-emitting diodes (OLEDs) with a tri-layer structure consisting of a hole transport layer, an emissive layer, and an electron transport layer. If layers of the OLED are deuterated through chemical synthesis then each layer can be characterised using NR [178]. To investigate the inter-diffusion between the layers upon thermal annealing, a custom, aluminium block, sample chamber was used within whichcartridge heaters were installed [179]. As the OLED layers are thermally annealed, the annealing process can be monitored by photoluminescence and the inter-diffusion between different layers monitored using NR [180–182].

Although unrelated to soft condensed matter, it is noteworthy that light illumination of a photochromic material has been recently combined with inelastic neutron spectroscopy [183]. Illumination of the sample in situ is achieved inside a CCR using a transparent sample holder and an LED light source. The photochromic material, when exposed to ultra violet or blue-light excitation, results in the initial pale yellow open form of *cis*-1,2-dicyano-1,2-bis(2,4,5-trimethyl-3-thienyl) ethene (CMTE) to a deep red closed isomer due to its undergoing a reversible photocyclization reaction.

Fourier transform infrared spectroscopy (FTIR) enables the determination of chemical and physical structure via interpretation of the spectrum of characteristic bands; the latter are produced by the excitation vibrations of molecular bonds following absorption of infrared photons in the material. The ability to combine IR methods with neutron scattering provides the opportunity to correlate structural or dynamic changes with, for example, local molecular level structure changes. A

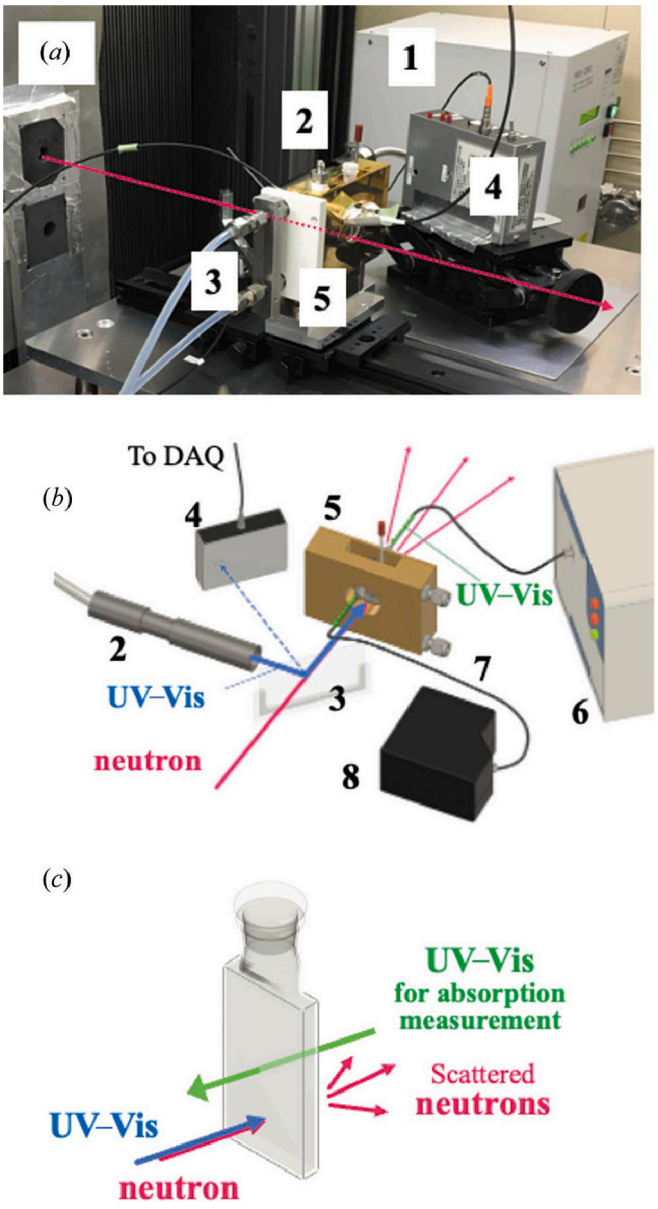

Fig. 11. (a) Photograph and (b) schematic drawing of the in situ UV–Vis irradiation system installed on the small- and wide-angle neutron scattering instrument TAIKAN at MLF, J-PARC. (1) A mercury lamp (REX-250, Asahi Spectra Co., Ltd., Japan), (2) a lens system, (3) an Al-coated quartz mirror (thickness of 2 mm), (4) a photodetector, (5) a cuvette holder, (6) a UV–Vis fibre light source for absorption measurement, (7) an optical fibre, (8) a UV–Vis absorption spectrometer. (c) Schematic drawing of simultaneous SANS and UV–Vis absorption spectroscopy. (DAQ = data acquisition.). Reproduced from [169] with permission from the International Union of Crystallography under creative commons CC BY 4.0 DEED.

system for the simultaneous measurement of SANS and transmission FTIR has been developed by Kaneko et al. [184]. Its application was demonstrated in temperature-dependent studies of a cocrystal of fully deuterated syndiotactic polystyrene with triethylene glycol dimethyl ether (TEGDME). The SANS data exhibit changes in lamellar intensity with temperature, first increasing, then decreasing, before subsequently increasing; however, the FTIR signal continuously decreases with temperature. These observations are correlated with displacement of the TEGDME guest molecule (which has a negative scattering length density) from the crystalline to amorphous regions in the lattice before its subsequent evaporation while the polystyrene undergoes a higher temperature phase transition to a more densely packed state. A similar approach has been reported with some of the same authors on the crystallisation of hydrogenated polyethylene glycol dimethyl ether in deuterated tetrahydrofuran solution [167]. Here, the initial SANS characteristic of semi-flexible coils in solution transforms at low q and subsequently exhibits lamellar peaks during the latter stages of crystallisation. The SANS is correlated with FTIR bands associated with the helical conformation of the polymer. In the same work, deuterated syndiotactic polystyrene films containing protonated toluene were also investigated. More recently, this work has been extended to both SANS and wide-angle neutron scattering through the use of polarised FTIR which additionally provides information on molecular orientation [185].

To be able to combine IR spectroscopy with reflectometry the IR measurements must be collected in an attenuated total reflectance (ATR) mode. Combining ATR-FTIR spectroscopy with reflectometry was conducted on the BioRef instrument for several years [186,187]; the instrument, formerly located at the BER II at the Helmholtz-Zentrum Berlin, is now at ANSTO and is known as Spatz with the ATR-FTIR option still available to users [188]. To be able to combine NR and ATR-FTIR, specially cut silicon wafers are needed where the edges are cut at a 45° angle so that the IR beam can be directed to the surface of interest below the critical angle to allow total internal reflection. Depending on the size of the silicon wafer used there can be 3, 5, etc., bounces at the interface before the beam exits the crystal towards the detector. The ATR-FTIR spectra can be collected at solid-liquid interfaces as well as air-solid interfaces.

Simultaneous NR and ATR-FTIR have been used to investigate the absorption of saponin biosurfactants to bilayers of DPPC on silicon wafers where NR showed that the saponin binds to the DPPC bilayer and penetrates into the bilayer and that the binding is reversable; ATR-FTIR highlighted the lack of change in the local vibrational modes in the CH_2 groups in the lipid alkyl chains associated predominantly with the polar headgroups [189]. More recently Garvey et al. [190] have investigated phase separation in ternary mixtures of phospholipids using a variety of techniques including simultaneous NR and ATR-FTIR. Creating a ternary system of DPPC/POPC/DOPC, the phase changes in the lipid mixtures were confirmed by both techniques. The work of Schwörer et al. [140,191] discussed above not only combined shear and NR but also included simultaneous ATR-FTIR measurements using a bespoke shear cell design [140] (Fig. 13). By combining NR and ATR-FTIR, the authors were able to correlate the symmetric and asymmetric CH_2 stretching in the IR spectrum to changes in the phase state of the lipid bilayers arising from variations in shear in the presence of the synovial fluid mimic PAH. As the shear is increased and the phospholipid bilayer fragments, ATR-FTIR demonstrated that the bilayers shifted from a gel to a fluid state. It was also found that increasing the PAH concentration causes the spacing between bilayers to swell however the ATR-FTIR confirmed that the bilayers do not completely detach from one another, and the phase state of the bilayers remains unchanged [191].

Groups have also conducted simultaneous infrared spectroscopic techniques with NR at the air-liquid interface. Skoda et al. [192] used a configuration on the INTER beamline at ISIS where Infrared Reflectance Absorption Spectroscopy (IRRAS) is utilised with a water-filled PTFE trough. The IRRAS-NR sample environment was used to investigate the effect of ozone gas (the equipment also contained a gas delivery system and chamber) on monolayers of pure fatty acids and mixed fatty acids at the air-water interface; NR provided structural information about the monolayer thickness and surface excess while the IRRAS provided information about the local environment of the monolayer acids. Mixing deuterated and hydrogenous fatty acids is not only advantageous for the NR but also for infrared spectroscopy techniques due to the difference in wavenumber from the signal of $-CH_2$ and $-CD_2$. By using mixtures of deuterated and hydrogenous fatty acids the authors were able to show the oxidation of different acids when exposed to ozone. The combined NR and IRRAS technique has been further used to investigate the

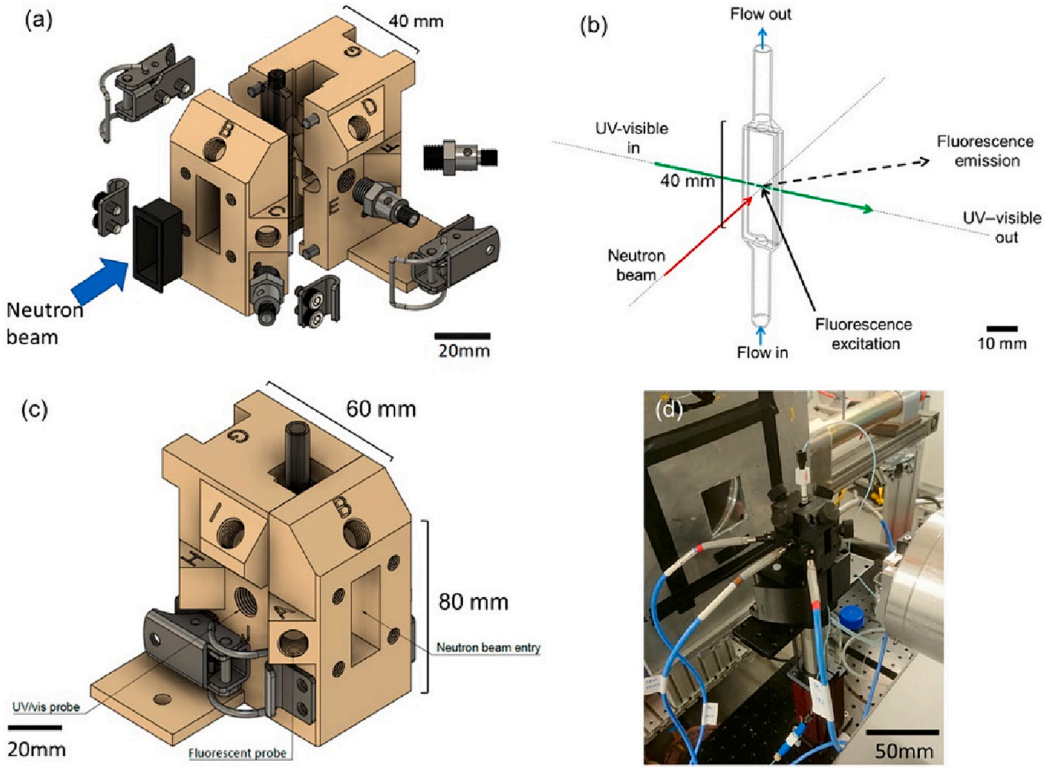

Fig. 12. (a) Exploded view of the 3D-printed sample holder. Note the 3D-printed boron/polymer aperture on the entrance port. The optical ports are labelled from A to J. Next to port C, E, and F are the Ocean Optics lenses. Top, side, and front views are available in the supplementary material. (b) Flow cell with the optical paths, sample flow, and neutron beam directions. (c) 90° rotated view of (a) without the Ocean Optics lenses and the boron/polymer aperture. (d) Photograph of the 3D printed cell setup on the SANS beamline Larmor (ISIS, UK). Reprinted from NUrF—Optimization of in situ UV–vis and fluorescence and autonomous characterization techniques with small-angle neutron scattering instrumentation, [175] Dicko et al., 2020, Rev. Sci. Instrum. 91, 075111 (2020) with the permission from AIP publishing.

exposure to oxidation of complex bacterial lipids found in marine aerosols [193].

Ellipsometry and NR are highly complementary techniques but rarely have they been performed simultaneously. Sample cells have been created where ellipsometry and NR can be performed on the same sample however the two techniques are measured separately [194]. Busch and colleagues [195] have created a mobile solid-liquid cell that can combine NR, ATR-FTIR spectroscopy, and spectroscopic ellipsometry (Fig. 14). As the equipment provides for an ATR-FTIR option, the same specially cut silicon wafers are used as mentioned above. The neutron and infrared beams are directed towards the solid-liquid interface through the silicon wafer perpendicular to each other but the polarised light beam for spectroscopic ellipsometry is directed to the interface through the bulk liquid. The authors demonstrated the usefulness of combining all three techniques for two examples of polyelectrolyte swelling as a function of pH and investigated the binding of gold nanoparticles to phospholipid bilayers.

Table 4 summarises many of the devices discussed in this section for the use of UV/visible/IR light in neutron scattering experiments.

4.7. Confinement

Confinement at an interface is where a material is geometrically constrained on the nanometre scale so that the materials brought close to one another experience different forces from that of the bulk. Conducting neutron scattering experiments, particularly reflectivity measurements, have been challenging due to achieving a strong enough scattering signal under confinement conditions [196]. Parallel plate hydraulic systems where a hydraulic press is used to bring two solid surfaces close to one another can be used to achieve confinement [197]. Most devices today that are used to study confinement consist of a flexible poly(ethylene terephthalate) (PET) membrane that is pushed towards the surface of interest using liquid to apply an even pressure behind the membrane; this approach can achieve confinement limits below 100 nm over large areas (>10 cm^2) [198]. This system has several advantages over parallel plate hydraulic systems such as the two surfaces can remain parallel, there is no long-range waviness of the surfaces, and any unwanted dust that may find itself on the surface will not prevent confinement. Recent investigations have assessed how confinement effects the thermal response of polymer brushes [199]. Thermo-responsive poly(N-isopropylacrylamide) (PNIPAM) brushes on silicon were found to have no critical temperature transition point under confinement with the brush always adopting a dehydrated block; the thermal response could be restored once confinement was removed. Many biomaterials function under confinement, however there is little structural information on how biomaterials perform under these conditions. One such material is mucin, a glycoprotein found in mucus which forms protective barriers around internal organs. Mucin films were chosen to study under confinement to investigate how the glycoprotein responds to the mechanical challenges that confinement presents. Using a cell of de Vos et al. [198], mucin films were deposited onto hydrophobized silicon surfaces and found to be a hydrated with a thickness of 440 Å [200]. Upon confinement at 0.1 MPa of pressure, the mucin films collapse with thickness of 20 Å and are highly dehydrated, with some loss of protein from the surface. Pressures above 0.1 MPa made no significant difference to the structure of the mucin films showing that pressures below 0.1 MPa are in the region where mucin films can provide mechanical protection.

A recent method to achieve confinement is to bring a solid-liquid and liquid-liquid interface close to one another. Micciulla et al. [201]

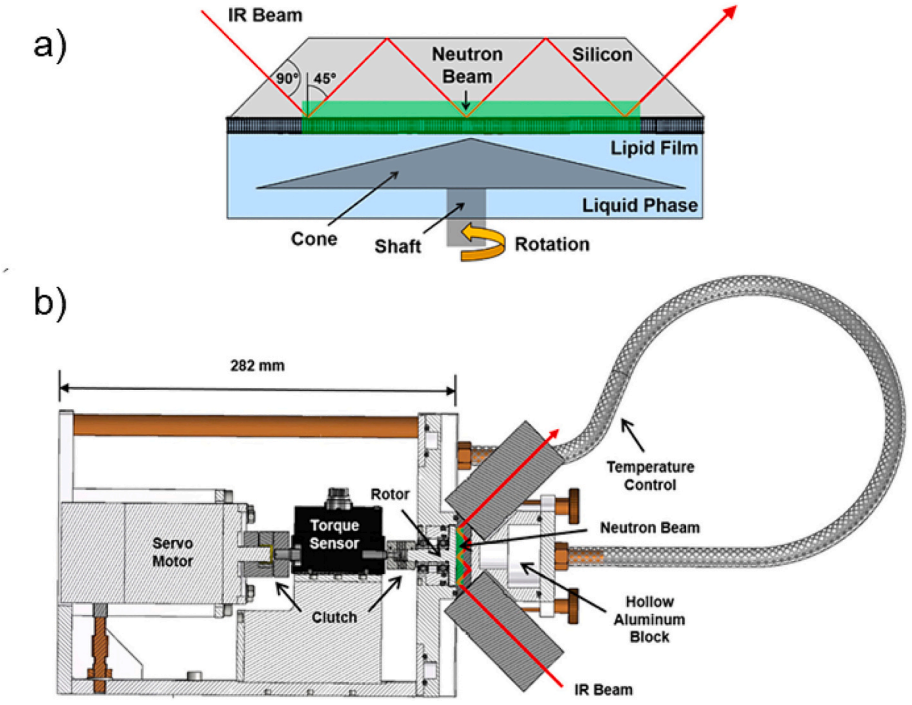

Fig. 13. (a) Schematic view of the combined NR/ATR-FTIR shear cell. The rotating cone exerts shear stress on the immobilized layer. IR analysis is performed in an ATR configuration with total reflection at the silicon–liquid interface. The neutron beam (green rectangle) is perpendicular to the IR beam and reflected at the same interface at a shallow angle. (b) Design drawing of the shear cell. Reproduced and adapted with permission from [140] Schwörer et al., Langmuir (2015) 31(42), 11,539–11,548. Copyright © 2015, American Chemical Society. (For interpretation of the references to colour in this figure legend, the reader is referred to the web version of this article.)

achieved this by placing functionalised silicon wafers in a sample cell designed for measuring liquid-liquid interfaces [37]. A silicon wafer with a grafted polyelectrolyte brush was placed in the cell and covered with aqueous solution. A mixed monolayer of phospholipid and polyethylene glycol (PEG) was then deposited onto the air-water interface above the wafer which was then subsequently covered with dodecane oil. The water was subsequently drained from the cell which brings the phospholipid/PEG monolayer geometrically close to the polyelectrolyte brush. This approach has several advantages, namely that the solid-liquid and air-liquid interfaces can be independently measured before confinement, there is always a homogenous interaction distance as the two layers are flexible, and the oil overlayer prevents evaporation so the system is always fully hydrated; the authors demonstrated different interaction cases depending on the makeup of the two interacting monolayers.

4.8. Humidity and vapour delivery

Humidity chambers based on the use of saturated salt solutions, saturated/dry gas flow or partial vapour pressure through controlling water reservoir temperature have been superseded by more sophisticated approaches. Gonthier et al. [202] report on the design of a precision humidity chamber for neutron diffraction but with a design that could be adapted for reflectometry, SANS, backscattering or time-of-flight instruments. The BerILL chamber is double walled but uses a reservoir of pure H_2O or D_2O that is temperature regulated by a water bath to generate the desired humidity through use of the Antoine equation. The relative humidity is controlled by independently controlling the temperatures of the sample and an attached water bath on the millidegree Celsius scale such that operation only requires entering two parameters, namely sample temperature and relative humidity. The chamber can control the relative humidity up to 99.9% with an accuracy of ±0.01%. The performance has been tested by monitoring the variation in d-spacing from lipid bilayers.

As well as humidity control and vapour delivery, gas is also relevant to the formation of foams. Kühnhammer et al. [203] have designed a dedicated device for the measurement of SANS on foams at different drainage states while providing control of the rate of foam formation, temperature and measurement position. The cell consists of a 250 mm long quartz glass cylinder with an inner diameter of 30 mm and a wall thickness of 2 mm. A porous quartz glass plate is fused to the bottom of the cylinder. When gas (e.g., air or nitrogen) is flowed via a gas-inlet socket, the continuous gas flow is disrupted into small bubbles. This results in the formation of foam when an appropriate foaming solution is poured into the cylinder. The gas exits the cylinder at the open top, which ensures pressure equilibrium. For temperature control, two thermostat-controlled jackets are fitted to each foam cylinder, while height variation enables different states of foam drainage to be investigated. When the gas flow is such that the foam retains a constant height in the cell, the position along the cell acts as a proxy for the age of the foam (i.e., the time passed after its formation at the bottom of the cylinder) and therefore its drainage state. A similar system is described in Mansour et al., [204] and Lamolinairie et al., [205] where the latter example also incorporates simultaneous electrical conductivity measurements. An alternative measurement is to stop the gas flow after a foam has been formed and monitor scattering changes during drainage to produce a ‘dry’ foam. Although published in the context of GI-SANS, a flexible sample environment capable of providing humidity control has been described by Widmann et al. [43,206]. This 3D printed spherical humidity chamber features a gas flow control assembly for atmospheric control and vapour mixing, adjustable temperature and an ability for in situ spectral reflectance (UV/Vis and near infrared) measurements, as well as a goniometer assembly for motion control and accurate sample alignment.

The use of humidity to investigate the structure of stacked lipid bilayer structures using neutron diffraction has been carried out for many years (for a review see for example, [207]). The stacked lipid bilayer structure is usually supported on a quartz or silicon slide and is

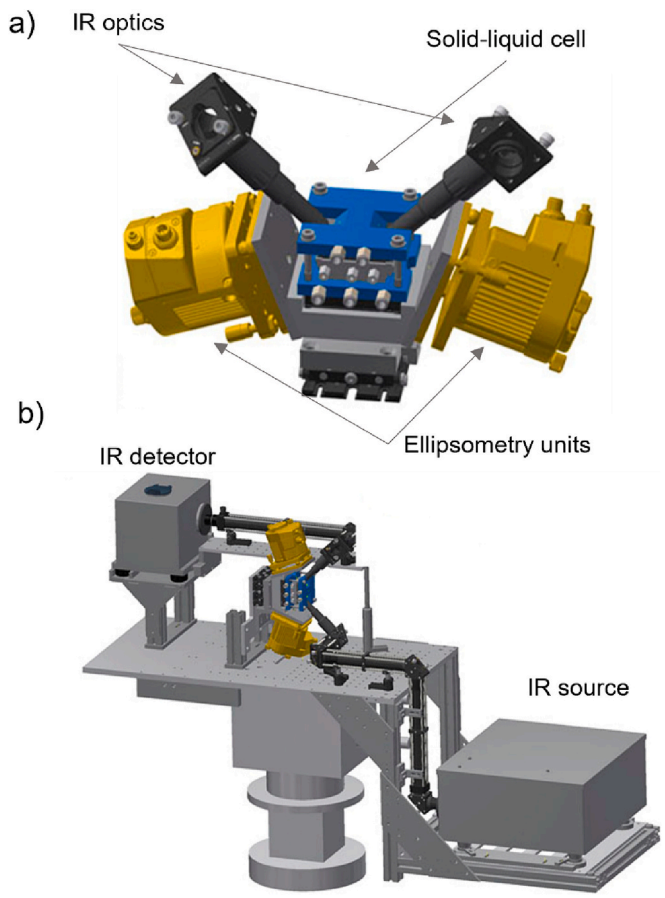

Fig. 14. Schematic of (a) the solid-liquid cell (in blue) for simultaneous neutron reflectometry, IR spectroscopy, and ellipsometry (modules in yellow), and (b) a schematic of the cell aligned for a neutron reflectometer using a vertical sample geometry. Figure reproduced and adapted from [195] under Creative Commons CC BY license. (For interpretation of the references to colour in this figure legend, the reader is referred to the web version of this article.)

hydrated using saturated salts. Different groups/facilities have designed sample containers for measuring stacked bilayers for neutron diffraction experiments but in essence the designs all have a method for generating humidity, a device to hold the sample, is sealed from the external environment, and has temperature regulation. Beyond the ILL/HZB BerILL humidity chamber [202] described above is the ORNL chamber for the WAND instrument at the HFIR reactor [208]. The latter uses the classical approach of where the sample is suspended above a reservoir of saturated salts that generate the humid environment. The canister is temperature controlled using a circulating water bath and is doubled lined and evacuated between the linings to keep the environment around the sample controlled. Such humidity chambers have recently been used to determine the structures of the skin lipid matrix [209,210], photosynthetic membranes [211], and yeast lipid membranes [212,213].

Other chamber systems have been used to investigate soft material responses to humidity. Melanin film swelling was investigated under different partial pressures of a D_2O vapour using a static vapour delivery system [214]. In this study a commercial static vapour delivery system was used which was connected to a custom-made sample chamber. Water (H_2O and D_2O) absorption was measured in situ at different partial pressures and the structural changes in the film monitored using NR. It was found that absorbed water is evenly distributed throughout the film and causing it to swell which has important implications for the bio-electronic properties of melanin. Using a system where the partial pressure of the water vapour could be controlled eliminated systematic errors that can occur with using saturated salt solutions to generate humidity. Studying the structure of Nafion films with NR under humidity has been of great interest due to its use as a soft electrolyte and as a material in fuel cells [215–217]. In a recent systematic approach, Cavaye et al. [218] used a custom-built static humidity delivery system to investigate the changes in Nafion films in situ in different relative humidities of D_2O, from which the water adsorption isotherm was obtained, and H_2O which showed gradual lamellar structures forming with increasing humidity. In the approach just described a static humidity delivery system was deployed, however dynamic vapour delivery systems have also been custom developed such as that of Arima-Osonoi et al. [219]; they used a dry line and wet line to carry the humidity through to a sample chamber (Fig. 15) with temperature and humidity sensors for monitoring. The equipment has been used to measure the swelling of polyvinyl alcohol (PVA) films; it was found at low humidities ($< 65\%$ RH) the water vapour fills voids in the film and at higher humidities the PVA films start to swell [219]. More recently this dynamic system was used to investigate water absorption in epoxy resins; it was found that at high curing temperatures (150 °C) any absorbed water from a humid atmosphere was located close to the silicon-epoxy resin interface whereas at lower curing temperatures absorbed water was distributed further through the epoxy resin film [220].

It is not just water vapour that can be delivered to samples of interest; organic vapours can also be studied. An example is the delivery of various polar organic vapours to graphene oxide (GO) films on silicon. It was found that the GO films swell in the presence of different organic vapours and, in some binary mixtures, one vapour may be selectively absorbed e.g., mixtures of methanol and ethanol where methanol is selectively absorbed [221]. Organic vapours have also been used to study the swelling of polymer films such as with polyvinyl acetate (PVAc) films on silicon in the presence of toluene vapour; here it was found that there is a thin layer of the PVAc film at the silicon interface that is impermeable to the toluene vapour [222]. For the previous two examples the organic vapours were delivered by placing a reservoir of the organic liquid in a sealed chamber with the sample of interest. Static or dynamic vapour delivery systems such as those mentioned above can also be used for organic vapour delivery as has been demonstrated by Geiger et al. [223] for investigating the solvency of *co*-polymer PMMA-b-PNIPAM thin films in water/methanol vapours.

Neutron radiography has been employed to explore various aspects of cultural heritage. An interesting recent development has been its potential to investigate canvas-supported paintings that comprise materials that are sensitive to moisture and susceptible to environmental fluctuations in temperature and relative humidity. Such environmental fluctuations can occur in uncontrolled environments found in historic houses and palaces; these induced stresses in paintings can lead to cracking and flaking of the paint layer and enhanced hydrolytic damage to the supporting canvases. Neutron radiography is ideally suited for the study of moisture transport due to the strong attenuation from hydrogen. As a proof of concept to validate the use of neutron radiography for dynamic measurements of sorption/desorption processes of moisture in painting canvases, and to evaluate the effect of novel canvas treatments on these processes. Bridarolli et al. [224] designed a custom-made closed-cell. This enabled canvases, that were untreated or treated with either a polar or non-polar nanocellulose-based consolidant, to be subjected to programmed cycles of relative humidity at fixed temperature to simulate enhanced effects of environmental fluctuations.

4.9. *Magnetic fields*

As a probe, neutrons provide unique information on magnetic materials due to their intrinsic interaction with unpaired electrons. Examples include magnetic nanoparticles for various technological, biomedical, or environmental applications [225]. Magnetic field application to colloidal samples or soft interfaces can enable structural orientation, re-assembly or, indeed, improved scattering contrasts

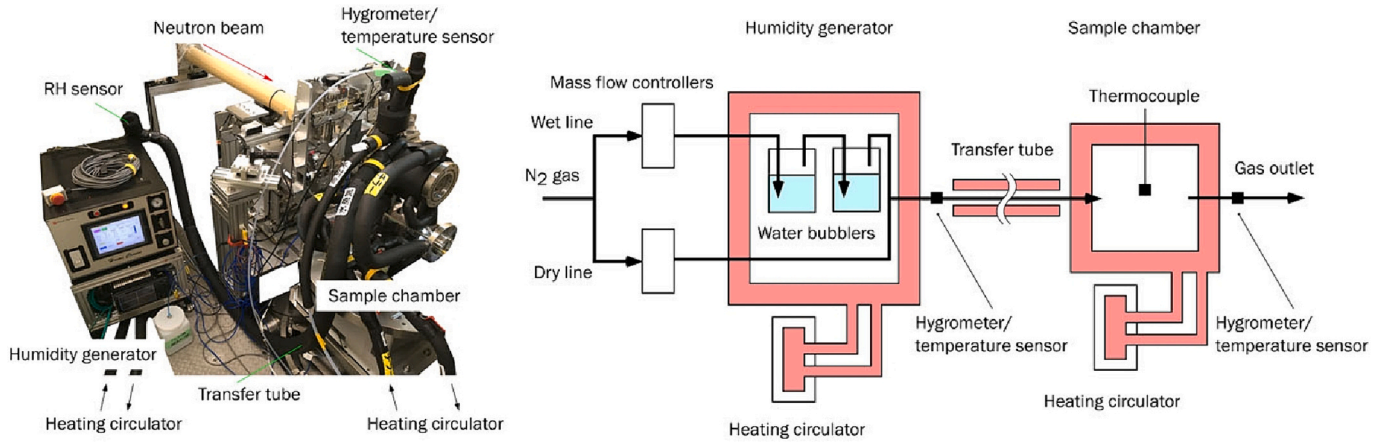

Fig. 15. Experimental setup at BL17 SHARAKU beamline at MLF, J-PARC, and a schematic diagram of the gas-flow humidity control system. Figure reproduced from [219] under Creative Commons CC BY license.

[226–228]. Further information can be achieved with the use of polarised neutrons and polarisation analysis. In concert, many facilities possess a range of magnets with varying geometry and field strength. By applying oscillating magnetic fields, the response and relaxation processes can be followed in real time down to microseconds through the use of the stroboscopic-like approach, referred to as TISANE [57]. This involves the synchronisation a periodic stimulus at the sample position, in this case an oscillating magnetic field, with an upstream chopper to pulse the neutron beam. This generates a condition in which the neutrons arriving at the detector have been scattered from the sample at the same time within the periodic sample stimulus but from different neutron pulses.

The dynamics and hence flow properties of magnetic fluids can be tuned via control of particle orientation and the potential creation of clusters. While rheology has been discussed above, the presence of a magnetic field in magnetic fluids offers opportunities for a range of applications based on changes in the magnetorheological behaviour including the magnetoviscous effect as well as shear-thinning and shear-thickening behaviours. Zakutna et al. [229] describe in situ "Magneto-RheoSANS" through the combination of a rheometer and a custom-made shielded Helmholtz coil set, which provides a static magnetic field of up to 20 mT perpendicular to the shear direction (vertical field direction); higher magnetic fields were observed to generate significant heat dissipation from the magnetic coils. Demonstration experiments were successfully performed on solutions of hematite nano-spindles.

Achieving the desired external magnetic field can be as simple placing permanent magnets close to the sample, or using electromagnets which can be used if changes in magnetic field strength are required. This approach has been applied to study the assembly of magnetite nanoparticles from ferrofluids at interfaces. The application of a magnetic field of approximately 11 mT was achieved by placing a permanent magnet against the solid-liquid cell [230]. When the magnetic field is applied, the nanoparticles assumed an ellipsoidal shape with the long axis along the magnetic field, creating a more compact layer. The work was furthered by applying higher magnetic fields of 100 mT using an electromagnet [231], where it was found that an ordered double layer of nanoparticles forms above a wetting layer. APRES-coated silicon ferromagnetic nanoparticles were found to self-assemble in magnetic fields of 100 mT and 250 mT generated using a neodymium permanent magnet with the nanoparticle layers becoming denser and structurally more well defined with the application of the field [232] (Fig. 16).

Magnetic fields can also be used to implement magnetic contrast NR to soft matter systems. When gold is deposited onto a silicon wafer for forming self-assembled structures through thiol chemistry, typically a metal binding layer is required between the gold and silicon. Usually, this metal binding layer is chromium or titanium; however, if a magnetic

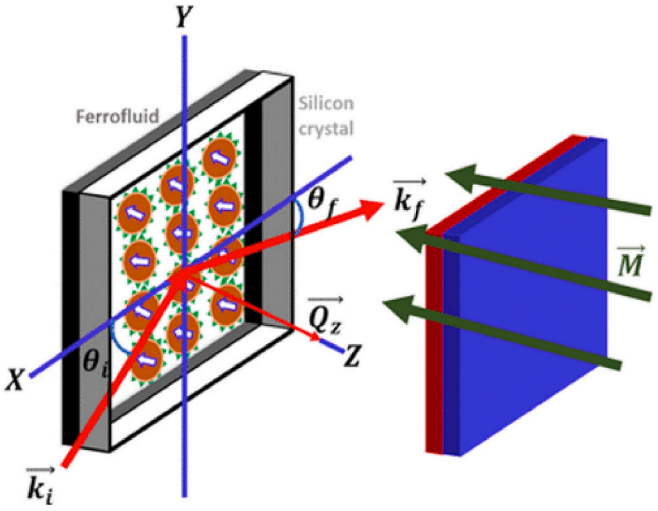

Fig. 16. Sketch of the experimental setup showing the incident and reflected neutron beams (k_i, k_f), the nanoparticle assembly, and the perpendicular magnetic field applied by using permanent magnets. Q_z is the vector of momentum transfer. Figure reproduced from [232] under Creative Commons CC-BY 4.0 license.

layer such as iron, Permalloy (80% nickel / 20% iron), or mu-metal (77% nickel, 16% iron, 5% copper, 2% molybdenum) is deposited, then polarised neutrons in combination with NR can be used to gain additional contrast. If the magnetic field of the deposited magnetic layer is in the same direction as an applied external magnetic field, then polarised neutrons will reflect differently from that magnetic layer as the neutron refractive index of the magnetic layer has a nuclear component plus or minus a magnetic component. This means that two SLD profiles can be obtained from the system without making any changes to any of the layers, providing an additional level of contrast [233]. The use of magnetic contrasts has been used to study complex systems such as biomembrane structures [234–237], biosensors [238–240], and more recently the assembly and structure of the β-barrel assembly machinery (BAM) complex [241], which is a bacterial outer membrane protein complex consisting of five proteins that fold and assemble bacterial membrane proteins into the outer membrane.

A somewhat less known technique that can be used to enhance contrast for SANS and that utilises magnetic fields (and low temperature) is dynamic nuclear polarisation where polarised neutrons (beam) are combined with polarised protons (sample). Since scattering length is

dependent on the relative orientation of proton and neutron spins, by manipulating the former within the nuclei of a target sample, scattering contrast can be changed. In a proton-containing material, at 1.2 K and 6.7 Tesla, the extent of proton polarisation is only 0.57% but the electron spins are almost fully polarised [242]. By combining with microwave irradiation, polarisation transfer can be achieved from the electrons to the protons to achieve high proton polarisation; the latter can be mediated with a stable free radical or electron dense complex. A recent example of how this approach has been used relates to the water distribution in human hair [242]. The broad range of application of this approach is described in Stuhrmann [243].

4.10. Electric fields and electrochemistry

The strength of an electric field is inversely proportional to the distance between the electrodes; as a consequence, higher voltages are required to produce the same field in a SANS experiment than in an analogous SAXS setup due to differences in beam size. While it is, of course, possible to place the electrodes directly in contact with the sample (e.g., by inserting two conducting wires into a quartz cuvette), this approach only works well for inert, insulating materials; however, in samples that contain ionic or conducting components, this approach may lead to unwanted electrochemical and resistive heating effects. An electric field sample environment designed to operate with standard SANS quartz cuvettes has been developed by Hayward et al. [244] (Fig. 17). The external field is produced using a function generator and a high-voltage amplifier. Applied fields of up to 8 kV/cm and where the applied field may be static or alternating (up to 10 kHz for 8 kV/cm and up to 60 kHz for 4 kV/cm) can be achieved. The ability to conduct such studies opens up opportunities for the investigation of field-directed self-assembly of colloidal materials and manipulation of electrorheological behaviour. Furthermore, such frequencies lend the device to the possibility of TISANE measurements, discussed above. The utility of this temperature-controlled device was demonstrated for a variety of liquid crystalline samples. The authors also investigated the influence of perfect insulator or perfect conductor bath fluids on the resultant electric field profiles. Improvements proposed include replacing the thermal fluid with a temperature-controlled air flow over the sample, which also has the advantage of facilitating rapid temperature jumps, and applying a symmetrical field with two live electrodes driven in anti-phase.

Various solid-liquid cells have been designed to apply an electrical potential to surfaces for NR studies. Cells used for electrochemistry can be assembled to use two electrodes with a working and counter electrode where a potential just needs to be applied to the surface of interest, or three electrodes where a reference electrode is used for full electrochemical analysis. Designs of electrochemical cells have been implemented on reflectometers with both horizontal (for example, [245]) or vertical geometry [246]. If the substrate of interest is coated with metal layers, then applying the electrodes is relatively straightforward, however if there are no metal layers then a material such as silicon with a low resistivity (< 1 Ω.cm) is required. Early work by Hillman and coworkers describes a neutron reflectometry cell with a three-electrode system [247,248]. The cell comprises a metal-coated quartz block, with the metal layer forming the working electrode, placed against a liquid filled PTFE chamber; the latter contains a platinum gauze counter electrode oriented parallel to the working electrode and a reference electrode. This type of cell has been used to measure in situ redox switching of polyvinylferrocene films to understand the dynamics of film swelling during potential cycling [249]. A similar electrochemical NR cell design has been used with event mode data collection to investigate the electrodeposition of metal films from deep eutectic solvents [250].

Recently investigating the adsorption of ionic liquids under different surface potentials has been of interest. Pilkington et al. [251] created a bespoke electrochemical cell for investigating the adsorption of a non-halogenated ionic liquid to gold surfaces under different potentials. The cell design only uses a two-electrode system (a reference electrode was not included to avoid instability and impurity issues) and utilises a glass counter electrode but a PTFE gasket. In this work the bulk SLD of the ionic liquid was matched to gold so that any interfacial structure arising from the application of a potential would be observed as a change in SLD against the gold and the bulk. In the work it was found that the ionic liquid boundary layer was formed between the gold and bulk solution and the composition of the boundary layer changed with applied potential. A similar approach has been used to investigate ionic liquid adsorption to niobium films [252]. A straightforward electrochemical cell with a three-electrode system was created where the working electrode was a niobium-coated silicon wafer which was separated from the counter electrode made of a Al_4Ti-coated roughened silicon wafer with a PTFE gasket. Embedded within one side of the gasket was a silver quasi-reference electrode. Using this cell, it was found that ionic liquids form an electrical double layer with anions enriched in the layer in contact with the niobium surface under a positive potential and vice versa under a negative potential.

The first attempt to structurally characterise electrochemical processes using neutron scattering across a liquid-liquid interface has recently been described [253]. A special liquid-liquid cell with working, counter, reference, and sensing electrodes, and incorporating quartz windows to allow passage of the neutron beam through the cell, was used. The two immiscible electrolyte solutions that were used were D_2O with 10 mM NaCl and a 60:40 (v/v) mixture of dodecane and 2-octanone with an organic electrolyte. It was found that the organic electrolyte forms a concentrated layer on the organic side of the interface regardless of the potential applied. To further the study, phospholipids with an overall negative charge were absorbed at the liquid-liquid interface and formed a layer that was much thicker than a single monolayer or bilayer. When a potential of $+0.45$ V was applied in the presence of the

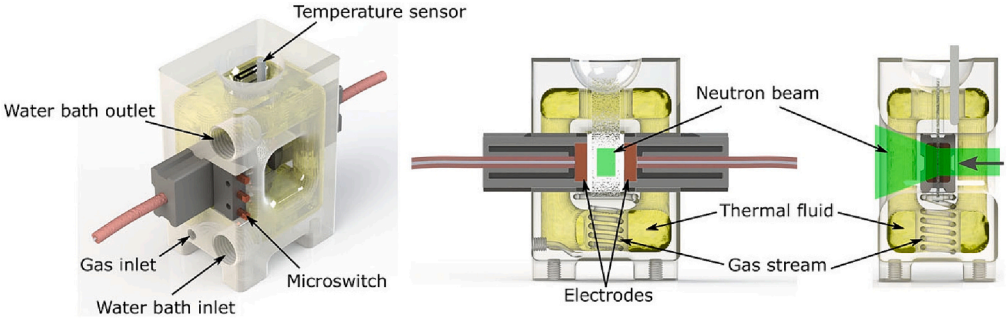

Fig. 17. Schematic and cross-sectional views of the electric-field sample environment with cell dimensions of 50 × 30 × 70 mm (width × depth × height); the body was constructed as a single piece by stereolithographic rapid prototyping. From left to right: perspective view, vertical cross section parallel to beam, and vertical cross section perpendicular to beam. Figure reproduced from [244] under Creative Commons Attribution 4.0 International License (http://creativecommons.org/licenses/by/4.0/).

phospholipid layer, an additional layer of hydrated sodium ions was formed adjacent to the bulk oil, which was not observed when the lipids were absent. The authors suggested that the phospholipids facilitated the exchange of cations across the interface. This work demonstrated that two immiscible electrolyte solutions can be structurally characterised simultaneously with electrochemical measurements, with the potential to further develop techniques to understand ion transfer in areas such as biological membranes.

4.11. Microwaves

Microwave treatment has not been extensively exploited in neutron scattering. Whittaker et al. combined microwaves with SANS to explore the hydrothermal preparation of iron oxide particles using a design that could be extended to wide-angle diffraction [254]. A number of unexplored opportunities exist for microwave radiation with neutrons including studies of how the connectivity of pores in shale oil, measured with SANS, can be enhanced in the context of gas recovery [255].

4.12. X-rays

Few would argue against the benefits of measuring the same sample with X-rays and neutrons. Contrast can be manipulated e.g., by means of hydrogen – deuterium substitution in the case of neutrons or by the addition of various contrasting agents such as sucrose, glycerol, or salts for SAXS. However, it is desirable to always ensure that the contrasting approach used does not alter the structure of the material being investigated. Metwalli et al. [256,257] recently reported on the development of a simultaneous SAXS/SANS platform on the D22 instrument at the ILL in which the sample is typically positioned at 45° relative to both of the orthogonal X-ray and neutron beams (Fig. 18). Background scattering, arising from neutrons scattered by the sample as well as from gamma rays produced by neutron absorption, result in a degradation in the signal-to-noise for SAXS measurements. Considerable effort was therefore expended to facilitate the SAXS measurements through the installation of optimized lead shielding and double energy threshold X-ray detector. The approach has been demonstrated for silica nanoparticle dispersions as well employed to study the time evolution of gold nanorods [258]. Interestingly magnetic shielding was also required as a magnetic field strength of approximately 0.2 to 0.5 mT was found to cause an X-ray beam drift. In addition, the N-REX reflectometer at FRM-2 can conduct simultaneous NR and X-ray reflectometry for samples at the air-solid interface [259]. This equipment has been used to investigate various properties of thin-metal films [260,261] and the formation of surface oxides [262].

4.13. Size exclusion chromatography

Size exclusion chromatography (SEC) has been used in combination with SAXS for almost 15 years as a means of enabling structural studies of aggregation-prone biomolecules that cannot be measured in their monomeric state in a standard experimental arrangement or, in the case of SAXS, where there exists the potential for radiation-damage mediated denaturation. More recently, Jordan et al. [263] implemented a SEC system within a SANS instrument. After calibrating with a series of standards varying in molecular weight from 1.35 to 670 kDa, the device was successfully used to study protonated and deuterated proteins Sir2a (34 kDa) and Alba3 (13 kDa). Johansen et al. [264] have subsequently used SEC-SANS to study the conformational distribution and associated dynamic behaviour of the pentameric Mg^{2+} ion channel, CorA with the addition of simultaneous UV absorption. Additional examples using membrane proteins and lipid nano discs have been reported by Johansen et al. [265] while more recent developments have been reported by Martel et al. [266]. An alternative separation technique is field flow fractionation. It relies on the laminar flow of a carrier liquid between two walls, separated by hundreds of microns, that forms a parabolic velocity profile. The sample to be separated is injected into the carrier stream at the inlet of the channel and exits through the outlet which is connected to a detector. Through application of an external field force, which can take several forms, e.g., sedimentation, electric, cross-flow, etc., molecules are pushed to the accumulation wall (e.g. an ultrafiltration membrane) where they obtain different average distances from the wall and are placed at different heights in the parabolic flow profile; the different sample molecules are consequently transported down the channel at different velocities. This approach has not yet been employed in-situ but has been used ex-situ to study e.g., the impact of hydrophobic polymer segments on the self-assembly behaviour of a supramolecular cyclic peptide [267], the location of a protein in the loading of a

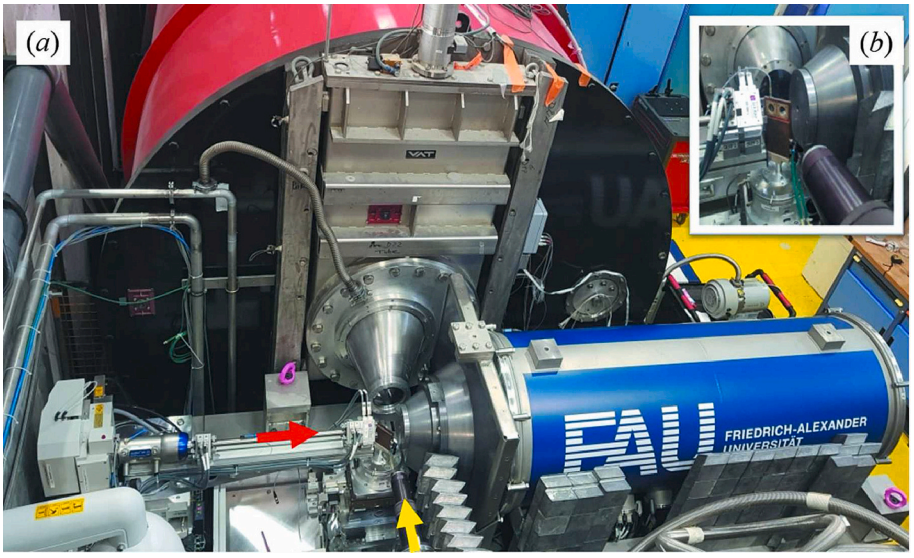

Fig. 18. (a) Photograph of the SAXS instrument installed at the D22 instrument (ILL) for simultaneous SAXS/SANS experiment. (b) A sample at an angle of 45° relative to both orthogonal neutron and X-ray beams. Lead shielding can be seen on the front of the detector vacuum chamber, along the neutron collimation and on the side of the vacuum chamber of the X-ray detector. The red and yellow arrows indicate the directions of the X-ray and neutron beams, respectively. Reproduced from [256] with permission from the International Union of Crystallography under creative commons CC BY 4.0 DEED. (For interpretation of the references to colour in this figure legend, the reader is referred to the web version of this article.)

polymersome [268], and the influence of glycerol on the chemical degradation of a protein [269].

5. Conclusions and outlook

This review has sought to highlight the role played by sample environments for neutron scattering measurements of relevance to researchers in the field of colloid and interface science. There are several areas where major developments are likely to occur in the foreseeable future. The availability of more powerful sources with enhanced time characteristics is likely to foster the development of new experiments that can benefit from greater flux, smaller beams and the opportunities for focussing (e.g., [270]); this will naturally give rise to new sample environments from which these capabilities can most effectively benefit. It is often the case that bespoke environments are needed to address specific scientific questions; the increased use of 3D printing approaches for both prototyping and full production will continue and is likely to benefit the colloid and interface community most. Finally, machine learning and artificial intelligence will inevitably revolutionize experimental design as well as the collection, analysis, and interpretation of data through the ability to automate highly controlled sample changes, perform faster experiments using straightforward instrument control software, and optimise the amount of information gained from a single experiment by carrying out in situ measurements using complementary techniques. What is currently generally lacking is the ability for software architecture to adequately correlate data with sample environment parameters, the simultaneous use of all data to generate structural models and, indeed, the development and use of multi-modal data formats. The ability to conduct more complicated experiments is also likely to see the greater uptake of neutron techniques to investigate real-world industrial processes e.g., extrusion, albeit where detailed structural analysis may not necessarily be required and correlations with processing parameters may be sufficient for meaningful insight to be gained.

CRediT authorship contribution statement

Anton P. Le Brun: Writing – review & editing, Writing – original draft. **Elliot Paul Gilbert:** Writing – review & editing, Writing – original draft.

Declaration of competing interest

None.

Data availability

No data was used for the research described in the article.

Acknowledgments

This review is inspired by the teams of sample environment technicians, designers and experts in the international neutron scattering community many of whom are affiliated with the International Society for Sample Environments (ISSE, https://sampleenvironment.org). Generations of users have benefited from essential sample environment equipment and will continue to do so. The authors particularly want to acknowledge the sample environment team at the Australian Centre for Neutron Scattering at ANSTO for their continued support and commitment to performing world-class science. The authors acknowledge funding support from the National Collaborative Research Infrastructure Strategy (NCRIS), an Australian Government initiative, for supporting sample environment operations at ANSTO. The authors would also like to thank Lilo Pozzo from the University of Washington and João T. Cabral from Imperial College London for providing figures.

References

[1] Lindner P, Schweins R, Campbell RA. Sample environment: Soft matter sample environment for small-angle neutron scattering and neutron reflectometry. In: Imae T, Kanaya T, Furusaka M, Torikai N, editors. Neutrons in Soft Matter. Hoboken, NJ: John Wiley & Sons, Inc.; 2011. https://doi.org/10.1002/9780470933886.ch14. Chapter 14. p. 383-414.
[2] van Eck NJ, Waltman L. Software survey: VOSviewer, a computer program for bibliometric mapping. Scientometrics 2010;84:523–38. https://doi.org/10.1007/s11192-009-0146-3.
[3] ACNS Sample Environment Group. Sample environment equipment handbook. https://www.ansto.gov.au/sites/default/files/2021-01/se_manual_06_01_21-compressed.pdf; 2021.
[4] Bailey IF. A review of sample environments in neutron scattering. Zeitschr Kristallogr - Crystall Mater 2003;218:84–95. https://doi.org/10.1524/zkri.218.2.84.20671.
[5] Urban VS, Heller WT, Katsaras J, Bras W. Soft matter sample environments for time-resolved small angle neutron scattering experiments: a review. Appl Sci 2021;11:5566. https://doi.org/10.3390/app11125566.
[6] Martel A, Gabel F. Chapter Nine - Time-resolved small-angle neutron scattering (TR-SANS) for structural biology of dynamic systems: Principles, recent developments, and practical guidelines. In: Tainer JA, editor. Methods in enzymology. vol. 677. Academic Press; 2022. p. 263–90. https://doi.org/10.1016/bs.mie.2022.08.010.
[7] Skoda MWA. Recent developments in the application of X-ray and neutron reflectivity to soft-matter systems. Curr Opin Colloid Interface Sci 2019;42:41–54. https://doi.org/10.1016/j.cocis.2019.03.003.
[8] Welbourn RJL, Clarke SM. New insights into the solid–liquid interface exploiting neutron reflectivity. Curr Opin Colloid Interface Sci 2019;42:87–98. https://doi.org/10.1016/j.cocis.2019.03.007.
[9] Bras W, Ryan AJ. Sample environments and techniques combined with small angle X-ray scattering. Adv Colloid Interf Sci 1998;75:1–43. https://doi.org/10.1016/S0001-8686(97)00032-8.
[10] Bras W, Koizumi S, Terrill NJ. Beyond simple small-angle X-ray scattering: developments in online complementary techniques and sample environments. IUCrJ 2014;1:478–91. https://doi.org/10.1107/S2052252514019198.
[11] Terrill NJ, Dent AJ, Dobson B, Beale AM, Allen L, Bras W. Past, present and future—sample environments for materials research studies in scattering and spectroscopy; a UK perspective. J Phys Condens Matter 2021;33:483002. https://doi.org/10.1088/1361-648X/ac2389.
[12] Pullen SA, Booth N, Olsen SR, Day B, Franceschini F, Mannicke D, et al. Design and implementation of a differential scanning calorimeter for the simultaneous measurement of small angle neutron scattering. Meas Sci Technol 2014;25:055606. https://doi.org/10.1088/0957-0233/25/5/055606.
[13] Barker J, Moyer J, Kline S, Jensen G, Cook J, Gagnon C, et al. The very small angle neutron scattering instrument at the National Institute of Standards and Technology. J Appl Crystallogr 2022;55:271–83. https://doi.org/10.1107/S1600576722000826.
[14] Bouwman WG. Spin-echo small-angle neutron scattering for multiscale structure analysis of food materials. Food Struct 2021;30:100235. https://doi.org/10.1016/j.foostr.2021.100235.
[15] Schmitt J, Zeeuw JJ, Plomp J, Bouwman WG, Washington AL, Dalgliesh RM, et al. Mesoporous silica formation mechanisms probed using combined spin–echo modulated Small-Angle Neutron Scattering (SEMSANS) and Small-Angle Neutron Scattering (SANS). ACS Appl Mater Interfaces 2020;12:28461–73. https://doi.org/10.1021/acsami.0c03287.
[16] Torikai N. Neutron Reflectometry. In: Imae T, Kanaya T, Furusaka M, Torikai N, editors. Neutrons in Soft Matter. Chapter 5. Hoboken, NJ: John Wiley & Sons, Inc; 2011. p. 115–45. https://doi.org/10.1002/9780470933886.ch5.
[17] Dalgliesh R. Application of off-specular scattering of X-rays and neutrons to the study of soft matter. Curr Opin Colloid Interface Sci 2002;7:244–8. https://doi.org/10.1016/S1359-0294(02)00054-7.
[18] Müller-Buschbaum P. Grazing incidence small-angle neutron scattering: challenges and possibilities. Polym J 2013;45:34–42. https://doi.org/10.1038/pj.2012.190.
[19] Ashkar R. Selective dynamics in polymeric materials: insights from quasi-elastic neutron scattering spectroscopy. J Appl Phys 2020:127. https://doi.org/10.1063/1.5144243.
[20] Krueger S. Small-angle neutron scattering contrast variation studies of biological complexes: challenges and triumphs. Curr Opin Struct Biol 2022;74:102375. https://doi.org/10.1016/j.sbi.2022.102375.
[21] Harris MJ, Dove MT, Parker JM. Floppy modes and the boson peak in crystalline and amorphous silicates: an inelastic neutron scattering study. Mineral Mag 2000;64:435–40.
[22] Cheung JY, Stewart RJ, May RP. Oxygen precipitation in Czochralski grown silicon heat treated at 525 °C. Semicond Sci Technol 2006;21:236. https://doi.org/10.1088/0268-1242/21/3/004.
[23] Gray EM, Bailey IF. Embrittlement of titanium–zirconium 'null-matrix' alloy by deuterium. J Neutron Res 2008;16:127–32. https://doi.org/10.1080/10238160903356504.
[24] Flacau R, Bolduc J, Bibienne T, Huot J, Fritzsche H. Performance of cu-coated vanadium cans for in situ neutron powder diffraction experiments on hydrogen storage materials. J Appl Crystallogr 2012;45:902–5. https://doi.org/10.1107/S002188981202938X.
[25] Kibble MG, Laliena V, Goodway CM, Lelièvre-Berna E, Kamenev KV, Klotz S, et al. Low-background materials for high pressure cells used in inelastic neutron

scattering experiments. J Neutron Res 2019;21:105–16. https://doi.org/10.3233/JNR-190115.
[26] Ericsson A, Pacheco V, Marattukalam JJ, Dalgliesh RM, Rennie AR, Fisk M, et al. Crystallization of a Zr-based metallic glass produced by laser powder bed fusion and suction casting. J Non-Cryst Solids 2021;571:120891. https://doi.org/10.1016/j.jnoncrysol.2021.120891.
[27] Sahlberg M, Rennie AR, Marattukalam JJ, Ericsson A, Pacheco V. A beam path component for use in neutron scattering equipment and method of producing such. Office SPaR, Sweden, patent number: SE 544 674 C2. 2022.
[28] Benmore CJ, Weber JKR. Aerodynamic levitation, supercooled liquids and glass formation. Adv Phys: X 2017;2:717–36. https://doi.org/10.1080/23746149.2017.1357498.
[29] Krauss SW, Schweins R, Magerl A, Zobel M. Free-film small-angle neutron scattering: a novel container-free in situ sample environment with minimized H/D exchange. J Appl Crystallogr 2019;52:284–8. https://doi.org/10.1107/S1600576719000906.
[30] Fragneto-Cusani G. Neutron reflectivity at the solid/liquid interface: examples of applications in biophysics. J Phys Condens Matter 2001;13:4973. https://doi.org/10.1088/0953-8984/13/21/322.
[31] Rennie AR, Hellsing MS, Lindholm E, Olsson A. Note: sample cells to investigate solid/liquid interfaces with neutrons. Rev Sci Instrum 2015:86. https://doi.org/10.1063/1.4906518.
[32] Hoogerheide DP, Heinrich F, Maranville BB, Majkrzak CF. Accurate background correction in neutron reflectometry studies of soft condensed matter films in contact with fluid reservoirs. J Appl Crystallogr 2020;53:15–26. https://doi.org/10.1107/S160057671901481X.
[33] Hoogerheide DP, Dura JA, Maranville BB, Majkrzak CF. Low-background neutron reflectometry from solid/liquid interfaces. J Appl Crystallogr 2022;55:58–66. https://doi.org/10.1107/S1600576721011924.
[34] Campbell RA, Wacklin HP, Sutton I, Cubitt R, Fragneto G. FIGARO: the new horizontal neutron reflectometer at the ILL. Eur Phys J Plus 2011;126:107. https://doi.org/10.1140/epjp/i2011-11107-8.
[35] Kyrey T, Ganeva M, Witte J, Feoktystov A, Wellert S, Holderer O. Grazing incidence small-angle neutron scattering: background determination and optimization for soft matter samples. Appl Sci 2021;11:3085. https://doi.org/10.3390/app11073085.
[36] Akutsu-Suyama K, Yamada NL, Ueda Y, Motokawa R, Narita H. New Design of a Sample Cell for neutron reflectometry in liquid–liquid systems and its application for studying structures at air–liquid and liquid–liquid interfaces. Appl Sci 2022;12:1215. https://doi.org/10.3390/app12031215.
[37] Scoppola E, Watkins E, Li Destri G, Porcar L, Campbell RA, Konovalov O, et al. Structure of a liquid/liquid interface during solvent extraction combining X-ray and neutron reflectivity measurements. Phys Chem Chem Phys 2015;17:15093–7. https://doi.org/10.1039/C5CP01809A.
[38] Olsson A, Rennie AR. Boron carbide composite apertures for small-angle neutron scattering made by three-dimensional printing. J Appl Crystallogr 2016;49:696–9. https://doi.org/10.1107/S1600576716000534.
[39] Haberl B, Molaison JJ, Frontzek M, Novak EC, Granroth GE, Goldsby D, et al. 3D-printed B4C collimation for neutron pressure cells. Rev Sci Instrum 2021:92. https://doi.org/10.1063/5.0055095.
[40] Knott JC, Khakbaz H, Allen J, Wu L, Mole RA, Baldwin C, et al. Few-layer hexagonal boron nitride / 3D printable polyurethane composite for neutron radiation shielding applications. Compos Sci Technol 2023;233:109876. https://doi.org/10.1016/j.compscitech.2022.109876.
[41] Doutch J, Bason M, Franceschini F, James K, Clowes D, Gilbert EP. Structural changes during starch pasting using simultaneous rapid Visco analysis and small-angle neutron scattering. Carbohydr Polym 2012;88:1061–71. https://doi.org/10.1016/j.carbpol.2012.01.066.
[42] Pajerowski DM, Ng R, Peterson N, Zhang Y, Stone MB, dos Santos AM, et al. 3D scanning and 3D printing AlSi10Mg single crystal mounts for neutron scattering. Rev Sci Instrum 2020:91. https://doi.org/10.1063/5.0008599.
[43] Widmann T, Kreuzer LP, Mangiapia G, Haese M, Frielinghaus H, Müller-Buschbaum P. 3D printed spherical environmental chamber for neutron reflectometry and grazing-incidence small-angle neutron scattering experiments. Rev Sci Instrum 2020:91. https://doi.org/10.1063/5.0012652.
[44] Campbell RA. Recent advances in resolving kinetic and dynamic processes at the air/water interface using specular neutron reflectometry. Curr Opin Colloid Interface Sci 2018;37:49–60. https://doi.org/10.1016/j.cocis.2018.06.002.
[45] Peterson PF, Campbell SI, Reuter MA, Taylor RJ, Zikovsky J. Event-based processing of neutron scattering data. Nucl Instrum Methods Phys Res, Sect A 2015;803:24–8. https://doi.org/10.1016/j.nima.2015.09.016.
[46] Peterson PF, Olds D, Savici AT, Zhou W. Advances in utilizing event based data structures for neutron scattering experiments. Rev Sci Instrum 2018:89. https://doi.org/10.1063/1.5034782.
[47] Granroth GE, An K, Smith HL, Whitfield P, Neuefeind JC, Lee J, et al. Event-based processing of neutron scattering data at the spallation neutron source. J Appl Crystallogr 2018;51:616–29. https://doi.org/10.1107/S1600576718004727.
[48] Adlmann FA, Gutfreund P, Ankner JF, Browning JF, Parizzi A, Vacaliuc B, et al. Towards neutron scattering experiments with sub-millisecond time resolution. J Appl Crystallogr 2015;48:220–6. https://doi.org/10.1107/S1600576714027848.
[49] Clulow AJ, Tao C, Lee KH, Velusamy M, McEwan JA, Shaw PE, et al. Time-resolved neutron reflectometry and photovoltaic device studies on sequentially deposited PCDTBT-fullerene layers. Langmuir 2014;30:11474–84. https://doi.org/10.1021/la5020779.
[50] Ballantyne AD, Barker R, Dalgliesh RM, Ferreira VC, Hillman AR, Palin EJR, et al. Electrochemical deposition of silver and copper from a deep eutectic solvent studied using time-resolved neutron reflectivity. J Electroanal Chem 2018;819:511–23. https://doi.org/10.1016/j.jelechem.2018.01.032.
[51] Calabrese MA, Wagner NJ, Rogers SA. An optimized protocol for the analysis of time-resolved elastic scattering experiments. Soft Matter 2016;12:2301–8. https://doi.org/10.1039/C5SM03039K.
[52] Adlmann FA, Busch S, Vacaliuc B, Nelson A, Ankner JF, Browning JF, et al. Normalization of stroboscopic neutron scattering experiments. Nucl Instrum Methods Phys Res, Sect B 2018;434:61–5. https://doi.org/10.1016/j.nimb.2018.08.030.
[53] Dalgliesh RM, Lau YGJ, Richardson RM, Riley DJ. Millisecond time resolution neutron reflection from a nematic liquid crystal. Rev Sci Instrum 2004;75:2955–9. https://doi.org/10.1063/1.1783596.
[54] López-Barrón CR, Porcar L, Eberle APR, Wagner NJ. Dynamics of melting and recrystallization in a polymeric micellar crystal subjected to large amplitude oscillatory shear flow. Phys Rev Lett 2012;108:258301. https://doi.org/10.1103/PhysRevLett.108.258301.
[55] Gurnon AK, Lopez-Barron CR, Eberle APR, Porcar L, Wagner NJ. Spatiotemporal stress and structure evolution in dynamically sheared polymer-like micellar solutions. Soft Matter 2014;10:2889–98. https://doi.org/10.1039/C3SM53113A.
[56] Wolff M, Saini A, Simonne D, Adlmann F, Nelson A. Time resolved polarised grazing incidence neutron scattering from composite materials. Polymers 2019;11:445. https://doi.org/10.3390/polym11030445.
[57] Mata JP, Hamilton WA, Gilbert EP. Application of time-resolved small angle neutron scattering to non-equilibrium kinetic studies. In: García Sakai V, Alba-Simionesco C, Chen S-H, editors. Dynamics of soft matter: Neutron applications. New York, NY: Springer US; 2012. p. 289–318. https://doi.org/10.1007/978-1-4614-0727-0_11.
[58] Bleuel M. Phase locked modulated (PLM) small angle neutron scattering (SANS). Nucl Instrum Methods Phys Res, Sect A 2019;927:184–6. https://doi.org/10.1016/j.nima.2019.01.099.
[59] Mukai AHC, Clarke MJ, Christensen MJ, Nilsson JMC, Shetty MG, Brambilla M, et al. Architecture of the data aggregation and streaming system for the European spallation source neutron instrument suite. J Instrum 2018;13:T10001. https://doi.org/10.1088/1748-0221/13/10/T10001.
[60] Hexemer A, Zwart P, Roth S, Sethian J, Setiadi A, Taylor A. Machine learning for X-ray and neutron scattering. https://sites.google.com/lbl.gov/machine-learning/home; 2023.
[61] Müller-Buschbaum P, Lohstroh W, Stieghorst C, Kreileder C. Machine learning conference for X-ray and neutron-based experiments. https://indico.frm2.tum.de/event/451/; 2024.
[62] Doucet M, Samarakoon AM, Do C, Heller WT, Archibald R, Alan Tennant D, et al. Machine learning for neutron scattering at ORNL. Mach Learn: Sci Technol 2021;2:023001. https://doi.org/10.1088/2632-2153/abcf88.
[63] Chen Z, Andrejevic N, Drucker NC, Nguyen T, Xian RP, Smidt T, et al. Machine learning on neutron and x-ray scattering and spectroscopies. Chemical. Phys Rev 2021:2. https://doi.org/10.1063/5.0049111.
[64] Drucker NC, Liu T, Chen Z, Okabe R, Chotrattanapituk A, Nguyen T, et al. Challenges and opportunities of machine learning on neutron and X-ray scattering. Synchrotr Radiat News 2022;35:16–20. https://doi.org/10.1080/08940886.2022.2112498.
[65] Hao Y, Feng E, Lu D, Zimmer L, Morgan Z, Chakoumakos BC, et al. Machine-learning-assisted automation of single-crystal neutron diffraction. J Appl Crystallogr 2023;56:519–25. https://doi.org/10.1107/S1600576723001516.
[66] Do C, Chen W-R, Lee S. Small angle scattering data analysis assisted by machine learning methods. MRS Adv 2020;5:1577–84. https://doi.org/10.1557/adv.2020.130.
[67] Archibald RK, Doucet M, Johnston T, Young SR, Yang E, Heller WT. Classifying and analyzing small-angle scattering data using weighted k nearest neighbors machine learning techniques. J Appl Crystallogr 2020;53:326–34. https://doi.org/10.1107/S1600576720000552.
[68] Chang M-C, Wei Y, Chen W-R, Do C. Deep learning-based super-resolution for small-angle neutron scattering data: attempt to accelerate experimental workflow. MRS Commun 2020;10:11–7. https://doi.org/10.1557/mrc.2019.166.
[69] Hinderhofer A, Greco A, Starostin V, Munteanu V, Pithan L, Gerlach A, et al. Machine learning for scattering data: strategies, perspectives and applications to surface scattering. J Appl Crystallogr 2023;56:3–11. https://doi.org/10.1107/S1600576722011566.
[70] Greco A, Starostin V, Hinderhofer A, Gerlach A, Skoda MWA, Kowarik S, et al. Neural network analysis of neutron and x-ray reflectivity data: pathological cases, performance and perspectives. Mach Learn: Sci Technol 2021;2:045003. https://doi.org/10.1088/2632-2153/abf9b1.
[71] Doucet M, Archibald RK, Heller WT. Machine learning for neutron reflectometry data analysis of two-layer thin films. Mach Learn: Sci Technol 2021;2:035001. https://doi.org/10.1088/2632-2153/abf257.
[72] Mironov D, Durant JH, Mackenzie R, Cooper JFK. Towards automated analysis for neutron reflectivity. Mach Learn: Sci Technol 2021;2:035006. https://doi.org/10.1088/2632-2153/abe7b5.
[73] Carmona Loaiza JM, Raza Z. Towards reflectivity profile inversion through artificial neural networks. Mach Learn: Sci Technol 2021;2:025034. https://doi.org/10.1088/2632-2153/abe564.
[74] Durant JH, Wilkins L, Cooper JFK. Optimizing experimental design in neutron reflectometry. J Appl Crystallogr 2022;55:769–81. https://doi.org/10.1107/S1600576722003831.

[75] Treece BW, Kienzle PA, Hoogerheide DP, Majkrzak CF, Löschea M, Heinricha F. Optimization of reflectometry experiments using information theory. J Appl Crystallogr 2019;52:47–59. https://doi.org/10.1107/S1600576718017016.
[76] Beaucage PA, Martin TB. The autonomous formulation laboratory: An open liquid handling platform for formulation discovery using X-ray and neutron scattering. Chem Mater 2023;35:846–52. https://doi.org/10.1021/acs.chemmater.2c03118.
[77] Fornalski D, García Sakai V, Postorino S, Silverwood I, Goodway C, Bones J, et al. Simultaneous thermodynamic and dynamical characterisation using in situ calorimetry with neutron spectroscopy. Low Temperat Phys 2019;45:289–93. https://doi.org/10.1063/1.5090042.
[78] Pullen SA, Gilbert EP, Olsen SR, Lang EA, Doolan KR. An in situ rapid heat–quench cell for small-angle neutron scattering. Meas Sci Technol 2008;19:065707. https://doi.org/10.1088/0957-0233/19/6/065707.
[79] Cabral JT, Gerard H, Clarke N, Higgins JS. Phase separation of polymer blend TMPC/PS: dependence on blending method. Phys B Condens Matter 2000;276-278:408–9. https://doi.org/10.1016/S0921-4526(99)01600-2.
[80] Zeng X, Ungar G, Spells SJ, King SM. Real-time neutron scattering study of transient phases in polymer crystallization. Macromolecules 2005;38:7201–4. https://doi.org/10.1021/ma0510486.
[81] Cabral JT, Higgins JS. Small angle neutron scattering from the highly interacting polymer mixture TMPC/PSd: no evidence of spatially dependent χ parameter. Macromolecules 2009;42:9528–36. https://doi.org/10.1021/ma901516v.
[82] Cheikh Sleiman H, Tengattini A, Briffaut M, Huet B, Dal Pont S. Simultaneous x-ray and neutron 4D tomographic study of drying-driven hydro-mechanical behavior of cement-based materials at moderate temperatures. Cem Concr Res 2021;147:106503. https://doi.org/10.1016/j.cemconres.2021.106503.
[83] Teixeira SCM, Leão JB, Gagnon C, McHugh MA. High pressure cell for bio-SANS studies under sub-zero temperatures or heat denaturing conditions. J Neutron Res 2018;20:13–23. https://doi.org/10.3233/JNR-180057.
[84] Berger JE, Teixeira SCM, Reed K, Razinkov VI, Sloey CJ, Qi W, et al. High-pressure, low-temperature induced unfolding and aggregation of monoclonal antibodies: role of the fc and fab fragments. J Phys Chem B 2022;126:4431–41. https://doi.org/10.1021/acs.jpcb.1c10528.
[85] Gomes DC, Teixeira SCM, Leão JB, Razinkov VI, Qi W, Rodrigues MA, et al. In situ monitoring of protein unfolding/structural states under cold high-pressure stress. Mol Pharm 2021;18:4415–27. https://doi.org/10.1021/acs.molpharmaceut.1c00604.
[86] Annighöfer B, Hélary A, Brûlet A, Colas de la Noue A, Loupiac C, Combet S. A high pressure cell using metallic windows to investigate the structure of molecular solutions up to 600 MPa by small-angle neutron scattering. Rev Sci Instrum 2019:90. https://doi.org/10.1063/1.5051765.
[87] Bannenberg Lars J, van Exter M, Verleg Malte N, Boshuizen B, Parnell Steven R, Thijs M, et al. Versatile pressure and temperature controlled cell for neutron reflectometry and small-angle neutron scattering. J Neutron Res 2023:1–13. https://doi.org/10.3233/JNR-230004.
[88] Dong X, Erkey C, Dai H-J, Li H-C, Cochran HD, Lin JS. Phase behavior and micelle size of an aqueous microdispersion in supercritical CO2 with a novel surfactant. Ind Eng Chem Res 2002;41:1038–42. https://doi.org/10.1021/ie010342t.
[89] Hill C, Umetsu Y, Fujita K, Endo T, Sato K, Yoshizawa A, et al. Design of Surfactant Tails for effective surface tension reduction and Micellization in water and/or supercritical CO2. Langmuir 2020;36:14829–40. https://doi.org/10.1021/acs.langmuir.0c02835.
[90] Sagisaka M, Iwama S, Ono S, Yoshizawa A, Mohamed A, Cummings S, et al. Nanostructures in water-in-CO2 microemulsions stabilized by double-chain fluorocarbon Solubilizers. Langmuir 2013;29:7618–28. https://doi.org/10.1021/la400376g.
[91] Müller A, Pütz Y, Oberhoffer R, Becker N, Strey R, Wiedenmann A, et al. Kinetics of pressure induced structural changes in super- or near-critical CO2-microemulsions. Phys Chem Chem Phys 2014;16:18092–7. https://doi.org/10.1039/C3CP53790K.
[92] Wrede O, Reimann Y, Lülsdorf S, Emmrich D, Schneider K, Schmid AJ, et al. Volume phase transition kinetics of smart N-n-propylacrylamide microgels studied by time-resolved pressure jump small angle neutron scattering. Sci Rep 2018;8:13781. https://doi.org/10.1038/s41598-018-31976-4.
[93] Hjelm RP, Taylor MA, Frash LP, Hawley ME, Ding M, Xu H, et al. Flow-through compression cell for small-angle and ultra-small-angle neutron scattering measurements. Rev Sci Instrum 2018:89. https://doi.org/10.1063/1.5022678.
[94] Etxegarai M, Tudisco E, Tengattini A, Viggiani G, Kardjilov N, Hall SA. Characterisation of single-phase fluid-flow heterogeneity due to localised deformation in a porous rock using rapid neutron tomography. J Imag 2021;7:275. https://doi.org/10.3390/jimaging7120275.
[95] Blach T, Radlinski AP, Vu P, Ji Y, de Campo L, Gilbert EP, et al. Deformation of pores in response to uniaxial and hydrostatic stress cycling in Marcellus shale: implications for gas recovery. Int J Coal Geol 2021;248:103867. https://doi.org/10.1016/j.coal.2021.103867.
[96] Sun M, Duan X, Liu Q, Blach TP, Ostadhassan M, Liu B, et al. The importance of pore-fracture connectivity in overmature marine shale for methane occurrence and transportation. Mar Pet Geol 2023;157:106495. https://doi.org/10.1016/j.marpetgeo.2023.106495.
[97] Radlinski AP, Blach T, Vu P, Ji Y, de Campo L, Gilbert EP, et al. Pore accessibility and trapping of methane in Marcellus shale. Int J Coal Geol 2021;248:103850. https://doi.org/10.1016/j.coal.2021.103850.
[98] Ruppert LF, Radlinski AP, In honor of Dr. Yuri B. Melnichenko: application of neutron scattering (SANS and USANS) to research on fossil fuel energy sources. Int J Coal Geol 2018;189:68–9. https://doi.org/10.1016/j.coal.2018.02.021.
[99] Melnickenko YB. Small-angle scattering from confined and interfacial fluids. 1 ed. Switzerland: Springer Cham; 2015. https://doi.org/10.1007/978-3-319-01104-2.
[100] Koga T, Seo YS, Shin K, Zhang Y, Rafailovich MH, Sokolov JC, et al. The role of elasticity in the anomalous swelling of polymer thin films in density fluctuating supercritical fluids. Macromolecules 2003;36:5236–43. https://doi.org/10.1021/ma021265w.
[101] Gupta RR, Lavery KA, Francis TJ, Webster JRP, Smith GS, Russell TP, et al. Self-diffusion of polystyrene in a CO2-swollen polystyrene matrix: a real time study using neutron reflectivity. Macromolecules 2003;36:346–52. https://doi.org/10.1021/ma021215r.
[102] Kreuzer M, Kaltofen T, Steitz R, Zehnder BH, Dahint R. Pressure cell for investigations of solid–liquid interfaces by neutron reflectivity. Rev Sci Instrum 2011:82. https://doi.org/10.1063/1.3505797.
[103] Winter R. Effects of hydrostatic pressure on lipid and surfactant phases. Curr Opin Colloid Interface Sci 2001;6:303–12. https://doi.org/10.1016/S1359-0294(01)00092-9.
[104] Smeller L. Pressure–temperature phase diagrams of biomolecules. Biochim Biophys Acta Protein Struct Mol Enzymol 2002;1595:11–29. https://doi.org/10.1016/S0167-4838(01)00332-6.
[105] Jeworrek C, Steitz R, Czeslik C, Winter R. High pressure cell for neutron reflectivity measurements up to 2500 bar. Rev Sci Instrum 2011:82. https://doi.org/10.1063/1.3553392.
[106] Wang P, Lerner AH, Taylor M, Baldwin JK, Grubbs RK, Majewski J, et al. High-pressure and high-temperature neutron reflectometry cell for solid-fluid interface studies. Eur Phys J Plus 2012;127:76. https://doi.org/10.1140/epjp/i2012-12076-0.
[107] Carmichael JR, Rother G, Browning JF, Ankner JF, Banuelos JL, Anovitz LM, et al. High-pressure cell for neutron reflectometry of supercritical and subcritical fluids at solid interfaces. Rev Sci Instrum 2012:83. https://doi.org/10.1063/1.3697999.
[108] Micciulla S, Gutfreund P, Kanduč M, Chiappisi L. Pressure-induced phase transitions of nonionic polymer brushes. Macromolecules 2023;56:1177–88. https://doi.org/10.1021/acs.macromol.2c01979.
[109] Levin A, Erlkamp M, Steitz R, Czeslik C. Volume profile of α-chymotrypsin during adsorption and enzymatic reaction on a poly(acrylic acid) brush. Phys Chem Chem Phys 2016;18:9070–8. https://doi.org/10.1039/C6CP00843G.
[110] Maestro A, Gutfreund P. In situ determination of the structure and composition of Langmuir monolayers at the air/water interface by neutron and X-ray reflectivity and ellipsometry. Adv Colloid Interf Sci 2021;293:102434. https://doi.org/10.1016/j.cis.2021.102434.
[111] Hossain KR, Turkewitz DR, Holt SA, Le Brun AP, Valenzuela SM. Sterol structural Features' impact on the spontaneous membrane insertion of CLIC1 into artificial lipid membranes. Langmuir 2023;39:3286–300. https://doi.org/10.1021/acs.langmuir.2c03129.
[112] Ciumac D, Gong H, Campbell RA, Campana M, Xu H, Lu JR. Structural elucidation upon binding of antimicrobial peptides into binary mixed lipid monolayers mimicking bacterial membranes. J Colloid Interface Sci 2021;598:193–205. https://doi.org/10.1016/j.jcis.2021.04.037.
[113] Vaillard A-S, El Haitami A, Dreier LB, Fontaine P, Cousin F, Gutfreund P, et al. Vertically heterogeneous 2D semi-interpenetrating networks based on cellulose acetate and cross-linked polybutadiene. Langmuir 2022;38:2538–49. https://doi.org/10.1021/acs.langmuir.1c03084.
[114] Bondaz L, Cousin F, Muller F, Pantoustier N, Perrin P, Luchini A, et al. pH-sensitive behavior of the PS-b-PDMAEMA copolymer at the air - water interface. Polymer 2021;221:123619. https://doi.org/10.1016/j.polymer.2021.123619.
[115] Eberle APR, Porcar L. Flow-SANS and Rheo-SANS applied to soft matter. Curr Opin Colloid Interface Sci 2012;17:33–43. https://doi.org/10.1016/j.cocis.2011.12.001.
[116] Gentile L, Behrens MA, Porcar L, Butler P, Wagner NJ, Olsson U. Multilamellar vesicle formation from a planar lamellar phase under shear flow. Langmuir 2014;30:8316–25. https://doi.org/10.1021/la501071s.
[117] Sharma J, King SM, Bohlin L, Clarke N. Apparatus for simultaneous rheology and small-angle neutron scattering from high-viscosity polymer melts and blends. Nucl Instrum Methods Phys Res, Sect A 2010;620:437–44. https://doi.org/10.1016/j.nima.2010.03.143.
[118] Velichko E, Tian B, Nikolaeva T, Koning J, van Duynhoven J, Bouwman WG. A versatile shear cell for investigation of structure of food materials under shear. Colloids Surf A Physicochem Eng Asp 2019;566:21–8. https://doi.org/10.1016/j.colsurfa.2018.12.046.
[119] Bent JF, Richards RW, Gough TD. Recirculation cell for the small-angle neutron scattering investigation of polymer melts in flow. Rev Sci Instrum 2003;74:4052–7. https://doi.org/10.1063/1.1602939.
[120] Bharati A, Hudson SD, Weigandt KM. Poiseuille and extensional flow small-angle scattering for developing structure–rheology relationships in soft matter systems. Curr Opin Colloid Interface Sci 2019;42:137–46. https://doi.org/10.1016/j.cocis.2019.07.001.
[121] Corona PT, Ruocco N, Weigandt KM, Leal LG, Helgeson ME. Probing flow-induced nanostructure of complex fluids in arbitrary 2D flows using a fluidic four-roll mill (FFoRM). Sci Rep 2018;8:15559. https://doi.org/10.1038/s41598-018-33514-8.
[122] Lopez CG, Watanabe T, Adamo M, Martel A, Porcar L, Cabral JT. Microfluidic devices for small-angle neutron scattering. J Appl Crystallogr 2018;51:570–83. https://doi.org/10.1107/S1600576718007264.
[123] Adamo M, Poulos AS, Lopez GC, Martel A, Porcar L, Cabral JT. Droplet microfluidic SANS. Soft Matter 2018;14:1759–70. https://doi.org/10.1039/C7SM02433A.

[124] Lopez CG, Watanabe T, Martel A, Porcar L, Cabral JT. Microfluidic-SANS: flow processing of complex fluids. Sci Rep 2015;5:7727. https://doi.org/10.1038/srep07727.
[125] Donina L, Rafique A, Khodaparast S, Porcar L, Cabral JT. Lamellar-to-MLV transformation in SDS/octanol/brine examined by microfluidic-SANS and polarised microscopy. Soft Matter 2021;17:10053–62. https://doi.org/10.1039/D1SM01215K.
[126] Fischer J, Porcar L, Cabral JT, Sottmann T. Shear-induced sponge-to-lamellar transition in bicontinuous microemulsions evidenced by microfluidic-SANS. J Colloid Interface Sci 2023;635:588–97. https://doi.org/10.1016/j.jcis.2022.12.125.
[127] Weston JS, Seeman DP, Blair DL, Salipante PF, Hudson SD, Weigandt KM. Simultaneous slit rheometry and in situ neutron scattering. Rheol Acta 2018;57:241–50. https://doi.org/10.1007/s00397-018-1073-0.
[128] Murphy RP, Riedel ZW, Nakatani MA, Salipante PF, Weston JS, Hudson SD, et al. Capillary RheoSANS: measuring the rheology and nanostructure of complex fluids at high shear rates. Soft Matter 2020;16:6285–93. https://doi.org/10.1039/D0SM00941E.
[129] Richards JJ, Riley JK. Dielectric RheoSANS: a mutual electrical and rheological characterization technique using small-angle neutron scattering. Curr Opin Colloid Interface Sci 2019;42:110–20. https://doi.org/10.1016/j.cocis.2019.05.002.
[130] Richards JJ, Wagner NJ, Butler PD. A strain-controlled RheoSANS instrument for the measurement of the microstructural, electrical, and mechanical properties of soft materials. Rev Sci Instrum 2017:88. https://doi.org/10.1063/1.4986770.
[131] Richards JJ, Gagnon CVL, Krzywon JR, Wagner NJ, Butler PD. Dielectric RheoSANS - simultaneous interrogation of impedance, rheology and small angle neutron scattering of complex fluids. J Vis Exp 2017;122:e55318. https://doi.org/10.3791/55318.
[132] Baker SM, Smith G, Pynn R, Butler P, Hayter J, Hamilton W, et al. Shear cell for the study of liquid-solid interfaces by neutron scattering. Rev Sci Instrum 1994;65:412–6. https://doi.org/10.1063/1.1145148.
[133] Hamilton WA, Butler PD, Baker SM, Smith GS, Hayter JB, Magid LJ, et al. Shear induced hexagonal ordering observed in an ionic viscoelastic fluid in flow past a surface. Phys Rev Lett 1994;72:2219–22. https://doi.org/10.1103/PhysRevLett.72.2219.
[134] Penfold J, Staples E, Tucker I, Fragnetto G. The effect of shear on the adsorption of non-ionic surfactants at the liquid—solid interface. Phys B Condens Matter 1996;221:325–30. https://doi.org/10.1016/0921-4526(95)00945-0.
[135] Wolff M, Kuhns P, Liesche G, Ankner JF, Browning JF, Gutfreund P. Combined neutron reflectometry and rheology. J Appl Crystallogr 2013;46:1729–33. https://doi.org/10.1107/S0021889813024059.
[136] Welbourn RJL, Bartholomew F, Gutfreund P, Clarke SM. Neutron reflectometry of an anionic surfactant at the solid–liquid interface under shear. Langmuir 2017;33:5982–90. https://doi.org/10.1021/acs.langmuir.7b00530.
[137] Korolkovas A, Rodriguez-Emmenegger C, de los Santos Pereira A, Chennevière A, Restagno F, Wolff M, et al. Polymer brush collapse under shear flow. Macromolecules 2017;50:1215–24. https://doi.org/10.1021/acs.macromol.6b02525.
[138] Maas M, Hess U, Rezwan K. The contribution of rheology for designing hydroxyapatite biomaterials. Curr Opin Colloid Interface Sci 2014;19:585–93. https://doi.org/10.1016/j.cocis.2014.09.002.
[139] Hamley IW, Burholt S, Hutchinson J, Castelletto V, da Silva ER, Alves W, et al. Shear alignment of bola-amphiphilic arginine-coated peptide nanotubes. Biomacromolecules 2017;18:141–9. https://doi.org/10.1021/acs.biomac.6b01425.
[140] Schwörer F, Trapp M, Ballauff M, Dahint R, Steitz R. Surface-active lipid linings under shear load—a combined in-situ neutron reflectivity and ATR-FTIR study. Langmuir 2015;31:11539–48. https://doi.org/10.1021/acs.langmuir.5b01678.
[141] Nemoto F, Yamada NL, Takabatake F, Seto H. Installation of a Rheometer on Neutron Reflectometer SOFIA at J-PARC toward Rheo-NR and Observation of the Crystallization Behavior of Cocoa Butter in Chocolate. In: Proceedings of the 3rd J-PARC Symposium (J-PARC2019). Vol. 33: Journal of the Physical Society of Japan; 2021. https://doi.org/10.7566/JPSCP.33.011077.
[142] Armstrong AJ, McCoy TM, Welbourn RJL, Barker R, Rawle JL, Cattoz B, et al. Towards a neutron and X-ray reflectometry environment for the study of solid–liquid interfaces under shear. Sci Rep 2021;11:9713. https://doi.org/10.1038/s41598-021-89189-1.
[143] Tein YS, Thompson BR, Majkrzak C, Maranville B, Renggli D, Vermant J, et al. Instrument for measurement of interfacial structure–property relationships with decoupled interfacial shear and dilatational flow: “Quadrotrough”. Rev Sci Instrum 2022:93. https://doi.org/10.1063/5.0090350.
[144] Pepicelli M, Verwijlen T, Tervoort TA, Vermant J. Characterization and modelling of Langmuir interfaces with finite elasticity. Soft Matter 2017;13:5977–90. https://doi.org/10.1039/C7SM01100H.
[145] López-Barrón CR, Zeng Y, Richards JJ. Chain stretching and recoiling during startup and cessation of extensional flow of bidisperse polystyrene blends. J Rheol 2017;61:697–710. https://doi.org/10.1122/1.4983828.
[146] Lam CN, Xu W-S, Chen W-R, Wang Z, Stanley CB, Carrillo J-MY, et al. Scaling behavior of anisotropy relaxation in deformed polymers. Phys Rev Lett 2018;121:117801. https://doi.org/10.1103/PhysRevLett.121.117801.
[147] López-Barrón CR, Zeng Y, Schaefer JJ, Eberle APR, Lodge TP, Bates FS. Molecular alignment in polyethylene during cold drawing using in-situ SANS and Raman spectroscopy. Macromolecules 2017;50:3627–36. https://doi.org/10.1021/acs.macromol.7b00504.
[148] Galuska LA, Muckley ES, Cao Z, Ehlenberg DF, Qian Z, Zhang S, et al. SMART transfer method to directly compare the mechanical response of water-supported and free-standing ultrathin polymeric films. Nat Commun 2021;12:2347. https://doi.org/10.1038/s41467-021-22473-w.
[149] Li DS, Lee Y-T, Xi Y, Pelivanov I, O’Donnell M, Pozzo LD. A small-angle scattering environment for in situ ultrasound studies. Soft Matter 2018;14:5283–93. https://doi.org/10.1039/C8SM01000E.
[150] Gupta S, Bleuel M, Schneider GJ. A new ultrasonic transducer sample cell for in situ small-angle scattering experiments. Rev Sci Instrum 2018:89. https://doi.org/10.1063/1.5021370.
[151] Torres JR, Fanelli VR, Shinohara Y, May AF, Ruiz-Rodriguez M, Everett MS, et al. Resonant ultrasound spectroscopy probe for in-situ neutron scattering measurements. Proceed Meet Acoust 2021;43. https://doi.org/10.1121/2.0001430.
[152] Hayward DW, Chiappisi L, Prévost S, Schweins R, Gradzielski M. A small-angle neutron scattering environment for in-situ observation of chemical processes. Sci Rep 2018;8:7299. https://doi.org/10.1038/s41598-018-24718-z.
[153] Jellicoe M, Igder A, Chuah C, Jones DB, Luo X, Stubbs KA, et al. Vortex fluidic induced mass transfer across immiscible phases. Chem Sci 2022;13:3375–85. https://doi.org/10.1039/D1SC05829K.
[154] Solheim TE, Salvemini F, Dalziel SB, Raston CL. Neutron imaging and modelling inclined vortex driven thin films. Sci Rep 2019;9:2817. https://doi.org/10.1038/s41598-019-39307-x.
[155] He S, Joseph N, Mirzamani M, Pye SJ, Al-anataki AHM, Whitten AE, et al. Vortex fluidic mediated encapsulation of functional fish oil featuring in situ probed small angle neutron scattering. npj Sci Food 2020;4:12. https://doi.org/10.1038/s41538-020-00072-1.
[156] Adamo M, Poulos AS, Miller RM, Lopez CG, Martel A, Porcar L, et al. Rapid contrast matching by microfluidic SANS. Lab Chip 2017;17:1559–69. https://doi.org/10.1039/C7LC00179G.
[157] Tabor RF, Eastoe J, Grillo I. Time-resolved small-angle neutron scattering as a lamellar phase evolves into a microemulsion. Soft Matter 2009;5:2125–9. https://doi.org/10.1039/B819196D.
[158] Virtanen OLJ, Kather M, Meyer-Kirschner J, Melle A, Radulescu A, Viell J, et al. Direct monitoring of microgel formation during precipitation polymerization of N-Isopropylacrylamide using in situ SANS. ACS Omega 2019;4:3690–9. https://doi.org/10.1021/acsomega.8b03461.
[159] Kelley EG, Nguyen MHL, Marquardt D, Maranville BB, Murphy RP. Measuring the time-evolution of nanoscale materials with stopped-flow and small-angle neutron scattering. JoVE 2021:e62873. https://doi.org/10.3791/62873.
[160] Hughes T-L, Falkowska M, Leutzsch M, Sederman AJ, Mantle MD, Headen TF, et al. Bulk and confined benzene-cyclohexane mixtures studied by an integrated Total neutron scattering and NMR method. Top Catal 2021;64:722–34. https://doi.org/10.1007/s11244-021-01437-w.
[161] Leutzsch M, Falkowska M, Hughes T-L, Sederman AJ, Gladden LF, Mantle MD, et al. An integrated total neutron scattering – NMR approach for the study of heterogeneous catalysis. Chem Commun 2018;54:10191–4. https://doi.org/10.1039/C8CC04740E.
[162] Kohlbrecher J, Bollhalder A, Vavrin R, Meier G. A high pressure cell for small angle neutron scattering up to 500MPa in combination with light scattering to investigate liquid samples. Rev Sci Instrum 2007:78. https://doi.org/10.1063/1.2817632.
[163] Heigl RJ, Longo M, Stellbrink J, Radulescu A, Schweins R, Schrader TE. Crossover from a linear to a branched growth regime in the crystallization of lysozyme. Cryst Growth Des 2018;18:1483–94. https://doi.org/10.1021/acs.cgd.7b01433.
[164] Nawroth T, Buch P, Buch K, Langguth P, Schweins R. Liposome formation from Bile Salt–Lipid Micelles in the digestion and drug delivery model FaSSIFmod estimated by combined time-resolved neutron and dynamic light scattering. Mol Pharm 2011;8:2162–72. https://doi.org/10.1021/mp100296w.
[165] Nigro V, Angelini R, King S, Franco S, Buratti E, Bomboi F, et al. Apparatus for simultaneous dynamic light scattering–small angle neutron scattering investigations of dynamics and structure in soft matter. Rev Sci Instrum 2021:92. https://doi.org/10.1063/5.0035529.
[166] Schmid AJ, Wiehemeier L, Jaksch S, Schneider H, Hiess A, Bögershausen T, et al. Flexible sample environments for the investigation of soft matter at the European spallation source: part I—the in situ SANS/DLS setup. Appl Sci 2021;11:4089. https://doi.org/10.3390/app11094089.
[167] Balacescu L, Brandl G, Kaneko F, Schrader TE, Radulescu A. Light scattering and absorption complementarities to neutron scattering: in situ FTIR and DLS techniques at the high-intensity and extended Q-range SANS diffractometer KWS-2. Appl Sci 2021;11:5135. https://doi.org/10.3390/app11115135.
[168] Vögl F, Balacescu L, Holderer O, Pasini S, Staringer S, Brandl G, et al. Multi-angle in situ dynamic light scattering at a neutron spin echo spectrometer. Rev Sci Instrum 2023:94. https://doi.org/10.1063/5.0136367.
[169] Iwase H, Akamatsu M, Inamura Y, Sakaguchi Y, Morikawa T, Kasai S, et al. New measurement system based on small-angle neutron scattering for structural analysis of light-responsive materials. J Appl Crystallogr 2023;56:110–5. https://doi.org/10.1107/S1600576722011104.
[170] Kelly EA, Houston JE, Evans RC. Probing the dynamic self-assembly behaviour of photoswitchable wormlike micelles in real-time. Soft Matter 2019;15:1253–9. https://doi.org/10.1039/C8SM01948G.
[171] Sakaguchi Y, Asaoka H, Uozumi Y, Kawakita Y, Ito T, Kubota M, et al. Measurement of transient photo-induced changes in thin films at J-PARC - time-resolved neutron reflectivity measurements of silver photo-diffusion into ge-chalcogenide films. In: Proceedings of the 2nd International Symposium on Science at J-PARC - Unlocking the Mysteries of Life, Matter and the Universe Vol.

8: Journal of the Physical Society of Japan; 2015. https://doi.org/10.7566/JPSCP.8.031023.
[172] Sakaguchi Y, Kasai S, Oh-Uchi K, Morikawa T, Iwase H, Akamatsu M, et al. Recent development of the sample environment for light irradiation experiments at the materials and life science experimental facility. In: Proceedings of the 3rd J-PARC Symposium (J-PARC2019). Vol. 33: Journal of the Physical Society of Japan; 2021. https://doi.org/10.7566/JPSCP.33.011100.
[173] Sakaguchi Y, Hanashima T, Ahmed Simon A-A, Mitkova M. Excitation light energy dependence of silver photodiffusion into amorphous germanium sulfide: neutron and X-ray reflectivity and X-ray diffraction. Phys Status Solidi B 2020; 257:2000178. https://doi.org/10.1002/pssb.202000178.
[174] Sakaguchi Y, Asaoka H, Mitkova M. Kinetics of silver photodiffusion into amorphous S-rich germanium sulphide – neutron and optical reflectivity. Pure Appl Chem 2019;91:1821–35. https://doi.org/10.1515/pac-2019-0217.
[175] Dicko C, Engberg A, Houston JE, Jackson AJ, Pettersson A, Dalgliesh RM, et al. NUrF—optimization of in situ UV–vis and fluorescence and autonomous characterization techniques with small-angle neutron scattering instrumentation. Rev Sci Instrum 2020:91. https://doi.org/10.1063/5.0011325.
[176] Cavaye H, Smith ARG, James M, Nelson A, Burn PL, Gentle IR, et al. Solid-state dendrimer sensors: probing the diffusion of an explosive analogue using neutron reflectometry. Langmuir 2009;25:12800–5. https://doi.org/10.1021/la9017689.
[177] Cavaye H, Shaw PE, Smith ARG, Burn PL, Gentle IR, James M, et al. Solid state dendrimer sensors: effect of dendrimer dimensionality on detection and sequestration of 2,4-Dinitrotoluene. J Phys Chem C 2011;115:18366–71. https://doi.org/10.1021/jp205586s.
[178] Smith ARG, Ruggles JL, Cavaye H, Shaw PE, Darwish TA, James M, et al. Investigating morphology and stability of Fac-tris (2-phenylpyridyl)iridium(III) films for OLEDs. Adv Funct Mater 2011;21:2225–31. https://doi.org/10.1002/adfm.201002365.
[179] Smith ARG, Lee KH, Nelson A, James M, Burn PL, Gentle IR. Diffusion – the hidden menace in organic optoelectronic devices. Adv Mater 2012;24:822–6. https://doi.org/10.1002/adma.201104029.
[180] McEwan JA, Clulow AJ, Shaw PE, Nelson A, Darwish TA, Burn PL, et al. Diffusion at interfaces in OLEDs containing a doped phosphorescent emissive layer. Adv Mater Interfaces 2016;3:1600184. https://doi.org/10.1002/admi.201600184.
[181] McEwan JA, Clulow AJ, Nelson A, Yepuri NR, Burn PL, Gentle IR. Dependence of organic interlayer diffusion on glass-transition temperature in OLEDs. ACS Appl Mater Interfaces 2017;9:14153–61. https://doi.org/10.1021/acsami.7b01450.
[182] McEwan JA, Clulow AJ, Nelson A, Krause-Heuer AM, Jansen-van Vuuren RD, Burn PL, et al. Diffusion in organic film stacks containing solution-processed phosphorescent poly(dendrimer) dopants. ACS Appl Mater Interfaces 2021;13: 30910–20. https://doi.org/10.1021/acsami.1c05940.
[183] Cavaye H, Schastny M. In situ illumination with inelastic neutron scattering: a study of the photochromic material cis-1,2-dicyano-1,2-bis(2,4,5-trimethyl-3-thienyl)ethene (CMTE). Phys Chem Chem Phys 2021;23:22324–9. https://doi.org/10.1039/D1CP03716A.
[184] Kaneko F, Seto N, Sato S, Radulescu A, Schiavone MM, Allgaier J, et al. Development of a simultaneous SANS/FTIR measuring system. Chem Lett 2015; 44:497–9. https://doi.org/10.1246/cl.141179.
[185] Kaneko F, Kawaguchi T, Radulescu A, Iwase H, Morikawa T, Takata S-i, et al. A new simultaneous measurement system of wide Q-range small angle neutron scattering combined with polarized Fourier transform infrared spectroscopy. Rev Sci Instrum 2019:90. https://doi.org/10.1063/1.5112054.
[186] Strobl M, Steitz R, Kreuzer M, Rose M, Herrlich H, Mezei F, et al. BioRef: A versatile time-of-flight reflectometer for soft matter applications at Helmholtz–Zentrum Berlin. Rev Sci Instrum 2011;82:055101. https://doi.org/10.1063/1.3581210.
[187] Trapp M, Steitz R, Kreuzer M, Strobl M, Rose M, Dahint R. BioRef II—neutron reflectometry with relaxed resolution for fast, kinetic measurements at HZB. Rev Sci Instrum 2016;87:105112. https://doi.org/10.1063/1.4964294.
[188] Le Brun AP, Huang TY, Pullen S, Nelson ARJ, Spedding J, Holt SA, et al. Spatz: the time-of-flight neutron reflectometer with vertical sample geometry at the OPAL research reactor. J Appl Crystallogr 2023;56:18–25. https://doi.org/10.1107/S160057672201086X.
[189] Wojciechowski K, Orczyk M, Gutberlet T, Trapp M, Marcinkowski K, Kobiela T, et al. Unusual penetration of phospholipid mono- and bilayers by Quillaja bark saponin biosurfactant. Biochim Biophys Acta (BBA) - Biomembr 2014;1838: 1931–40. https://doi.org/10.1016/j.bbamem.2014.04.008.
[190] Garvey CJ, Bryant SJ, Elbourne A, Hunt T, Kent B, Kreuzer M, et al. Phase separation in a ternary DPPC/DOPC/POPC system with reducing hydration. J Colloid Interface Sci 2023;638:719–32. https://doi.org/10.1016/j.jcis.2023.01.145.
[191] Schwörer F, Trapp M, Xu X, Soltwedel O, Dzubiella J, Steitz R, et al. Drastic swelling of lipid Oligobilayers by polyelectrolytes: a potential molecular model for the internal structure of lubricating films in mammalian joints. Langmuir 2018;34:1287–99. https://doi.org/10.1021/acs.langmuir.7b03229.
[192] Skoda MWA, Thomas B, Hagreen M, Sebastiani F, Pfrang C. Simultaneous neutron reflectometry and infrared reflection absorption spectroscopy (IRRAS) study of mixed monolayer reactions at the air–water interface. RSC Adv 2017;7:34208–14. https://doi.org/10.1039/C7RA04900E.
[193] Woden B, Skoda MWA, Hagreen M, Pfrang C. Night-time oxidation of a monolayer model for the air–water interface of marine aerosols—a study by simultaneous neutron reflectometry and in situ Infra-Red Reflection Absorption Spectroscopy (IRRAS). Atmosphere 2018;9:471. https://doi.org/10.3390/atmos9120471.
[194] Sebastiani F, Campbell RA, Pfrang C. Complementarity of neutron reflectometry and ellipsometry for the study of atmospheric reactions at the air–water interface. RSC Adv 2015;5:107105–11. https://doi.org/10.1039/C5RA22725A.
[195] Busch C, Nagy B, Stöcklin A, Gutfreund P, Dahint R, Ederth T. A mobile setup for simultaneous and in situ neutron reflectivity, infrared spectroscopy, and ellipsometry studies. Rev Sci Instrum 2022:93. https://doi.org/10.1063/5.0118329.
[196] Wei Z, Prescott SW. Scattering approaches to probing surface layers under confinement. Curr Opin Colloid Interface Sci 2015;20:253–60. https://doi.org/10.1016/j.cocis.2015.09.001.
[197] Hamilton WA, Smith GS, Alcantar NA, Majewski J, Toomey RG, Kuhl TL. Determining the density profile of confined polymer brushes with neutron reflectivity. J Polym Sci B Polym Phys 2004;42:3290–301. https://doi.org/10.1002/polb.20170.
[198] de Vos WM, Mears LLE, Richardson RM, Cosgrove T, Dalgliesh RM, Prescott SW. Measuring the structure of thin soft matter films under confinement: a surface-force type apparatus for neutron reflection, based on a flexible membrane approach. Rev Sci Instrum 2012:83. https://doi.org/10.1063/1.4767238.
[199] Gresham IJ, Humphreys BA, Willott JD, Johnson EC, Murdoch TJ, Webber GB, et al. Geometrical confinement modulates the Thermoresponse of a poly(N-isopropylacrylamide) brush. Macromolecules 2021;54:2541–50. https://doi.org/10.1021/acs.macromol.0c02775.
[200] Gonzalez-Martinez JF, Boyd H, Gutfreund P, Welbourn RJL, Robertsson C, Wickström C, et al. MUC5B mucin films under mechanical confinement: a combined neutron reflectometry and atomic force microscopy study. J Colloid Interface Sci 2022;614:120–9. https://doi.org/10.1016/j.jcis.2022.01.096.
[201] Micciulla S, Gerelli Y, Campbell RA, Schneck E. A versatile method for the distance-dependent structural characterization of interacting soft interfaces by neutron reflectometry. Langmuir 2018;34:789–800. https://doi.org/10.1021/acs.langmuir.7b02971.
[202] Gonthier J, Barrett MA, Aguettaz O, Baudoin S, Bourgeat-Lami E, Demé B, et al. BerILL: the ultimate humidity chamber for neutron scattering. J Neutron Res 2019;21:65–76. https://doi.org/10.3233/JNR-190109.
[203] Kühnhammer M, Widmann T, Kreuzer LP, Schmid AJ, Wiehemeier L, Frielinghaus H, et al. Flexible sample environments for the investigation of soft matter at the European spallation source: part III—the macroscopic foam cell. Appl Sci 2021;11:5116. https://doi.org/10.3390/app11115116.
[204] Mansour OT, Cattoz B, Beaube M, Montagnon M, Heenan RK, Schweins R, et al. Assembly of small molecule surfactants at highly dynamic air–water interfaces. Soft Matter 2017;13:8807–15. https://doi.org/10.1039/C7SM01914A.
[205] Lamolinairie J, Dollet B, Bridot J-L, Bauduin P, Diat O, Chiappisi L. Probing foams from the nanometer to the millimeter scale by coupling small-angle neutron scattering, imaging, and electrical conductivity measurements. Soft Matter 2022; 18:8733–47. https://doi.org/10.1039/D2SM01252A.
[206] Widmann T, Kreuzer LP, Kühnhammer M, Schmid AJ, Wiehemeier L, Jaksch S, et al. Flexible sample environment for the investigation of soft matter at the European spallation source: part II—the GISANS setup. Appl Sci 2021;11:4036. https://doi.org/10.3390/app11094036.
[207] Foglia F, Lawrence MJ, Barlow DJ. Studies of model biological and bio-mimetic membrane structure: reflectivity vs diffraction, a critical comparison. Curr Opin Colloid Interface Sci 2015;20:235–43. https://doi.org/10.1016/j.cocis.2015.08.001.
[208] Marquardt D, Frontzek MD, Zhao Y, Chakoumakos BC, Katsaras J. Neutron diffraction from aligned stacks of lipid bilayers using the WAND instrument. J Appl Crystallogr 2018;51:235–41. https://doi.org/10.1107/S1600576718001243.
[209] Beddoes CM, Gooris GS, Foglia F, Ahmadi D, Barlow DJ, Lawrence MJ, et al. Arrangement of ceramides in the skin: sphingosine chains localize at a single position in stratum Corneum lipid matrix models. Langmuir 2020;36:10270–8. https://doi.org/10.1021/acs.langmuir.0c01992.
[210] Beddoes CM, Gooris GS, Barlow DJ, Lawrence MJ, Dalgliesh RM, Malfois M, et al. The importance of ceramide headgroup for lipid localisation in skin lipid models. Biochim Biophys Acta Biomembr 2022;1864:183886. https://doi.org/10.1016/j.bbamem.2022.183886.
[211] Bolik S, Albrieux C, Schneck E, Demé B, Jouhet J. Sulfoquinovosyldiacylglycerol and phosphatidylglycerol bilayers share biophysical properties and are good mutual substitutes in photosynthetic membranes. Biochim Biophys Acta Biomembr 2022;1864:184037. https://doi.org/10.1016/j.bbamem.2022.184037.
[212] Luchini A, Delhom R, Cristiglio V, Knecht W, Wacklin-Knecht H, Fragneto G. Effect of ergosterol on the interlamellar spacing of deuterated yeast phospholipid multilayers. Chem Phys Lipids 2020;227:104873. https://doi.org/10.1016/j.chemphyslip.2020.104873.
[213] Luchini A, Corucci G, Chaithanya Batchu K, Laux V, Haertlein M, Cristiglio V, et al. Structural characterization of natural yeast phosphatidylcholine and bacterial phosphatidylglycerol lipid multilayers by neutron diffraction. Front Chem 2021:9. https://doi.org/10.3389/fchem.2021.628186.
[214] Clulow AJ, Mostert AB, Sheliakina M, Nelson A, Booth N, Burn PL, et al. The structural impact of water sorption on device-quality melanin thin films. Soft Matter 2017;13:3954–65. https://doi.org/10.1039/C6SM02420C.
[215] Dura JA, Murthi VS, Hartman M, Satija SK, Majkrzak CF. Multilamellar Interface structures in Nafion. Macromolecules 2009;42:4769–74. https://doi.org/10.1021/ma802823j.
[216] DeCaluwe SC, Kienzle PA, Bhargava P, Baker AM, Dura JA. Phase segregation of sulfonate groups in Nafion interface lamellae, quantified via neutron reflectometry fitting techniques for multi-layered structures. Soft Matter 2014;10: 5763–76. https://doi.org/10.1039/C4SM00850B.

[217] DeCaluwe SC, Baker AM, Bhargava P, Fischer JE, Dura JA. Structure-property relationships at Nafion thin-film interfaces: thickness effects on hydration and anisotropic ion transport. Nano Energy 2018;46:91–100. https://doi.org/10.1016/j.nanoen.2018.01.008.
[218] Cavaye H, Welbourn RJL, Gluschke JG, Hughes P, Nguyen KV, Micolich AP, et al. Systematic in situ hydration neutron reflectometry study on Nafion thin films. Phys Chem Chem Phys 2022;24:28554–63. https://doi.org/10.1039/D2CP03067E.
[219] Arima-Osonoi H, Miyata N, Yoshida T, Kasai S, Ohuchi K, Zhang S, et al. Gas-flow humidity control system for neutron reflectivity measurements. Rev Sci Instrum 2020:91. https://doi.org/10.1063/5.0021128.
[220] Liu Y, Miyata N, Miyazaki T, Shundo A, Kawaguchi D, Tanaka K, et al. Neutron reflectometry analysis of condensed water layer formation at a solid Interface of epoxy resins under high humidity. Langmuir 2023;39:10154–62. https://doi.org/10.1021/acs.langmuir.3c01091.
[221] Klechikov A, Sun J, Vorobiev A, Talyzin AV. Swelling of thin graphene oxide films studied by in situ neutron reflectivity. J Phys Chem C 2018;122:13106–16. https://doi.org/10.1021/acs.jpcc.8b01616.
[222] Miyazaki T, Shimokita K, Yamamoto K, Aoki H, Yamada NL, Miyata N. Neutron reflectivity on the Mobile surface and immobile interfacial layers in the poly(vinyl acetate) adsorption layer on a Si substrate with deuterated toluene vapor-induced swelling. Langmuir 2020;36:15181–8. https://doi.org/10.1021/acs.langmuir.0c03025.
[223] Geiger C, Reitenbach J, Kreuzer LP, Widmann T, Wang P, Cubitt R, et al. PMMA-b-PNIPAM thin films display cononsolvency-driven response in mixed water/methanol vapors. Macromolecules 2021;54:3517–30. https://doi.org/10.1021/acs.macromol.1c00021.
[224] Bridarolli A, Odlyha M, Burca G, Duncan JC, Akeroyd FA, Church A, et al. Controlled environment neutron radiography of moisture sorption/desorption in nanocellulose-treated cotton painting canvases. ACS Appl Poly Mater 2021;3:777–88. https://doi.org/10.1021/acsapm.0c01073.
[225] Honecker D, Bersweiler M, Erokhin S, Berkov D, Chesnel K, Venero DA, et al. Using small-angle scattering to guide functional magnetic nanoparticle design. Nanoscale Adv 2022;4:1026–59. https://doi.org/10.1039/D1NA00482D.
[226] Kirby BJ, Kienzle PA, Maranville BB, Berk NF, Krycka J, Heinrich F, et al. Phase-sensitive specular neutron reflectometry for imaging the nanometer scale composition depth profile of thin-film materials. Curr Opin Colloid Interface Sci 2012;17:44–53. https://doi.org/10.1016/j.cocis.2011.11.001.
[227] Mühlbauer S, Honecker D, Périgo ÉA, Bergner F, Disch S, Heinemann A, et al. Magnetic small-angle neutron scattering. Rev Mod Phys 2019;91:015004. https://doi.org/10.1103/RevModPhys.91.015004.
[228] Theis-Bröhl K, Saini A, Wolff M, Dura JA, Maranville BB, Borchers JA. Self-assembly of magnetic nanoparticles in Ferrofluids on different templates investigated by neutron reflectometry. Nanomaterials 2020;10:1231. https://doi.org/10.3390/nano10061231.
[229] Zákutná D, Graef K, Dresen D, Porcar L, Honecker D, Disch S. In situ magnetorheological SANS setup at Institut Laue-Langevin. Colloid Polym Sci 2021;299:281–8. https://doi.org/10.1007/s00396-020-04713-5.
[230] Theis-Bröhl K, Gutfreund P, Vorobiev A, Wolff M, Toperverg BP, Dura JA, et al. Self assembly of magnetic nanoparticles at silicon surfaces. Soft Matter 2015;11:4695–704. https://doi.org/10.1039/C5SM00484E.
[231] Theis-Bröhl K, Vreeland EC, Gomez A, Huber DL, Saini A, Wolff M, et al. Self-assembled layering of magnetic nanoparticles in a Ferrofluid on silicon surfaces. ACS Appl Mater Interfaces 2018;10:5050–60. https://doi.org/10.1021/acsami.7b14849.
[232] Saini A, Theis-Bröhl K, Koutsioubas A, Krycka KL, Borchers JA, Wolff M. Magnetic particle self-assembly at functionalized interfaces. Langmuir 2021;37:4064–71. https://doi.org/10.1021/acs.langmuir.0c03235.
[233] Majkrzak CF, Berk NF. Inverting neutron reflectivity from layered film structures using polarized beams. Phys B Condens Matter 1999;267-268:168–74. https://doi.org/10.1016/S0921-4526(99)00055-1.
[234] Holt SA, Le Brun AP, Majkrzak CF, McGillivray DJ, Heinrich F, Lösche M, et al. An ion-channel-containing model membrane: structural determination by magnetic contrast neutron reflectometry. Soft Matter 2009;5:2576–86. https://doi.org/10.1039/B822411K.
[235] Hughes AV, Holt SA, Daulton E, Soliakov A, Charlton TR, Roser SJ, et al. High coverage fluid-phase floating lipid bilayers supported by ω-thiolipid self-assembled monolayers. J R Soc Interface 2014;11:20140447. https://doi.org/10.1098/rsif.2014.0447.
[236] Hughes AV, Patel DS, Widmalm G, Klauda JB, Clifton LA, Im W. Physical properties of bacterial outer membrane models: neutron reflectometry & molecular simulation. Biophys J 2019;116:1095–104. https://doi.org/10.1016/j.bpj.2019.02.001.
[237] Clifton LA, Holt SA, Hughes AV, Daulton EL, Arunmanee W, Heinrich F, et al. An accurate in vitro model of the E. Coli envelope. Angew Chem Int Ed 2015;54:11952–5. https://doi.org/10.1002/anie.201504287.
[238] Le Brun AP, Holt SA, Shah DS, Majkrzak CF, Lakey JH. Monitoring the assembly of antibody-binding membrane protein arrays using polarised neutron reflection. Eur Biophys J 2008;37:639–45. https://doi.org/10.1007/s00249-008-0291-2.
[239] Le Brun AP, Holt SA, Shah DSH, Majkrzak CF, Lakey JH. The structural orientation of antibody layers bound to engineered biosensor surfaces. Biomaterials 2011;32:3303–11. https://doi.org/10.1016/j.biomaterials.2011.01.026.
[240] Le Brun A, Soliakov A, Shah DH, Holt S, McGill A, Lakey J. Engineered self-assembling monolayers for label free detection of influenza nucleoprotein. Biomed Microdevices 2015;17:1–10. https://doi.org/10.1007/s10544-015-9951-z.
[241] Hall SCL, Clifton LA, Sridhar P, Hardy DJ, Wotherspoon P, Wright J, et al. Surface-tethered planar membranes containing the β-barrel assembly machinery: a platform for investigating bacterial outer membrane protein folding. Biophys J 2021;120:5295–308. https://doi.org/10.1016/j.bpj.2021.10.033.
[242] Noda Y, Koizumi S, Maeda T, Inada T, Ishihara A. Water distribution in human hair microstructure elucidated by spin contrast variation small-angle neutron scattering. J Appl Crystallogr 2023;56:1015–31. https://doi.org/10.1107/S160057672300465X.
[243] Stuhrmann HB. Polarised neutron scattering from dynamic polarised nuclei 1972–2022. Eur Phys J E 2023;46:41. https://doi.org/10.1140/epje/s10189-023-00295-6.
[244] Hayward DW, Magro G, Hörmann A, Prévost S, Schweins R, Richardson RM, et al. A temperature-controlled electric field sample environment for small-angle neutron scattering experiments. Rev Sci Instrum 2021:92. https://doi.org/10.1063/5.0040675.
[245] Lauw Y, Rodopoulos T, Gross M, Nelson A, Gardner R, Horne MD. Electrochemical cell for neutron reflectometry studies of the structure of ionic liquids at electrified interface. Rev Sci Instrum 2010:81. https://doi.org/10.1063/1.3455178.
[246] Mizusawa M, Sakurai K, Yamazaki D, Takeda M. An electrochemical cell with vertical geometry for neutron reflectivity measurements. Phys B Condens Matter 2018;551:270–3. https://doi.org/10.1016/j.physb.2018.01.050.
[247] Roser SJ, Richardson RM, Swann MJ, Hillman AR. In situ neutron reflectivity studies of polybithiophene. J Chem Soc Faraday Trans 1991;87:2863–4. https://doi.org/10.1039/FT9918702863.
[248] Richardson RM, Swann MJ, Hillman AR, Roser SJ. In situ neutron reflectivity studies of electroactive films. Faraday Discuss 1992;94:295–306. https://doi.org/10.1039/FD9929400295.
[249] Cooper JM, Cubitt R, Dalgliesh RM, Gadegaard N, Glidle A, Hillman AR, et al. Dynamic in situ electrochemical neutron reflectivity measurements. J Am Chem Soc 2004;126:15362–3. https://doi.org/10.1021/ja044682s.
[250] Hillman AR, Barker R, Dalgliesh RM, Ferreira VC, Palin EJR, Sapstead RM, et al. Real-time in situ dynamic sub-surface imaging of multi-component electrodeposited films using event mode neutron reflectivity. Faraday Discuss 2018;210:429–49. https://doi.org/10.1039/C8FD00084K.
[251] Pilkington GA, Harris K, Bergendal E, Reddy AB, Palsson GK, Vorobiev A, et al. Electro-responsivity of ionic liquid boundary layers in a polar solvent revealed by neutron reflectance. J Chem Phys 2018:148. https://doi.org/10.1063/1.5001551.
[252] Nishi N, Uchiyashiki J, Ikeda Y, Katakura S, Oda T, Hino M, et al. Potential-dependent structure of the ionic layer at the electrode Interface of an ionic liquid probed using neutron reflectometry. J Phys Chem C 2019;123:9223–30. https://doi.org/10.1021/acs.jpcc.9b01151.
[253] Tummino A, Scoppola E, Fragneto G, Gutfreund P, Maestro A, Dryfe RAW. Neutron reflectometry study of the interface between two immiscible electrolyte solutions: effects of electrolyte concentration, applied electric field, and lipid adsorption. Electrochim Acta 2021;384:138336. https://doi.org/10.1016/j.electacta.2021.138336.
[254] Whittaker AG, Harrison A, Oakley GS, Youngson ID, Heenan RK, King SM. Preliminary experiments on apparatus for in situ studies of microwave-driven reactions by small angle neutron scattering. Rev Sci Instrum 2001;72:173–6. https://doi.org/10.1063/1.1332112.
[255] Sun M, Zhao X, Liu Q, Ukaomah CF, Jiang S, Hu Q, et al. Investigation of microwave irradiation stimulation to enhance the pore connectivity of shale. Energy Fuel 2021;35:3240–51. https://doi.org/10.1021/acs.energyfuels.1c00108.
[256] Metwalli E, Gotz K, Lages S, Bar C, Zech T, Noll DM, et al. A novel experimental approach for nanostructure analysis: simultaneous small-angle X-ray and neutron scattering. J Appl Crystallogr 2020;53:722–33. https://doi.org/10.1107/S1600576720005208.
[257] Metwalli E, Götz K, Zech T, Bär C, Schuldes I, Martel A, et al. Simultaneous SAXS/SANS method at D22 of ILL: instrument upgrade. Appl Sci 2021;11:5925. https://doi.org/10.3390/app11135925.
[258] Zech T, Metwalli E, Götz K, Schuldes I, Porcar L, Unruh T. Investigating growth of gold nanorods by simultaneous small-angle X-ray and neutron scattering. Part Part Syst Charact 2022;39:2100172. https://doi.org/10.1002/ppsc.202100172.
[259] Khaydukov Y, Soltwedel O, Keller T. NREX: neutron reflectometer with X-ray option. J Large-Scale Res Facil 2015;1:A38. https://doi.org/10.17815/jlsrf-1-30.
[260] Khaydukov Y, Morari R, Soltwedel O, Keller T, Christiani G, Logvenov G, et al. Interfacial roughness and proximity effects in superconductor/ferromagnet CuNi/Nb heterostructures. J Appl Phys 2015:118. https://doi.org/10.1063/1.4936789.
[261] Khaydukov Y, Morari R, Mustafa L, Kim JH, Keller T, Belevski S, et al. Structural, magnetic, and superconducting characterization of the CuNi/Nb bilayers of the S/F type using polarized neutron reflectometry and complementary techniques. J Supercond Nov Magn 2015;28:1143–7. https://doi.org/10.1007/s10948-014-2850-3.
[262] Khaydukov YN, Soltwedel O, Marchenko YA, Khaidukova DY, Csik A, Acartürk T, et al. Formation of thin oxide layer on surface of copper caused by implantation of high-energy oxygen ions. J Surf Investig: X-ray, Synchrot Neutr Techn 2017;11:206–10. https://doi.org/10.1134/S1027451017010293.
[263] Jordan A, Jacques M, Merrick C, Devos J, Forsyth VT, Porcar L, et al. SEC-SANS: size exclusion chromatography combined in situ with small-angle neutron scattering. J Appl Crystallogr 2016;49:2015–20. https://doi.org/10.1107/S1600576716016514.

[264] Johansen NT, Bonaccorsi M, Bengtsen T, Larsen AH, Tidemand FG, Pedersen MC, et al. Mg2+−dependent conformational equilibria in CorA and an integrated view on transport regulation. eLife 2022;11:e71887. https://doi.org/10.7554/eLife.71887.

[265] Johansen NT, Pedersen MC, Porcar L, Martel A, Arleth L. Introducing SEC-SANS for studies of complex self-organized biological systems. Acta Crystallogr Sect D 2018;74:1178–91. https://doi.org/10.1107/S2059798318007180.

[266] Martel A, Cocho C, Caporaletti F, Jacques M, El Aazzouzi A, Lapeyre F, et al. Upgraded D22 SEC-SANS setup dedicated to the biology community. J Appl Crystallogr 2023;56:994–1001. https://doi.org/10.1107/S1600576723004119.

[267] Kariuki M, Rho JY, Hall SCL, Perrier S. Investigating the impact of hydrophobic polymer segments on the self-assembly behavior of supramolecular cyclic peptide systems via asymmetric-flow field flow fractionation. Macromolecules 2023;56:6618–32. https://doi.org/10.1021/acs.macromol.3c00442.

[268] Palinske M, Muza UL, Moreno S, Appelhans D, Boye S, Schweins R, et al. Potential of small-angle neutron scattering for evaluating protein locus within a polymersome. Macromol Chem Phys 2023;224:2200300. https://doi.org/10.1002/macp.202200300.

[269] Ramm I, Sanchez-Fernandez A, Choi J, Lang C, Fransson J, Schagerlöf H, et al. The impact of glycerol on an Affibody conformation and its correlation to chemical degradation. Pharmaceutics 2021;13:1853. https://doi.org/10.3390/pharmaceutics13111853.

[270] Hansen UB, Bertelsen M, Stahn J, Lefmann K. An optional focusing SELENE extension to conventional neutron guides: a case study for the ESS instrument BIFROST. Nucl Instrum Methods Phys Res, Sect A 2017;852:46–56. https://doi.org/10.1016/j.nima.2017.01.075.